UNIVERSITY OF CALIFORNIA, SAN DIEGO

Statistical Mechanics of the Cytoskeleton

A dissertation submitted in partial satisfaction of the
requirements for the degree
Doctor of Philosophy

in

Physics

by

Shenshen Wang

Committee in charge:

Professor Herbert Levine, Chair
Professor Peter G. Wolynes, Co-Chair
Professor Olga K. Dudko
Professor J. Andrew McCammon
Professor José N. Onuchic

2012

The dissertation of Shenshen Wang is approved, and it is acceptable in quality and form for publication on microfilm and electronically:

_____

_____

_____

_____
Co-Chair

_____
Chair

University of California, San Diego

2012

DEDICATION

To my parents, and Ching-Kit.

TABLE OF CONTENTS

LIST OF FIGURES

ACKNOWLEDGEMENTS

Upon the completion of my dissertation, I recollect with great gratitude the twinkling moments in my memory. I realize these are all about the people who went through some part of the journey with me and warmed up the way. They grant me the belief that all my struggle is worthwhile.

I am deeply grateful to my supervisor, Dr. Peter Wolynes, who gave me the freedom to discover myself and grow the confidence, from the very beginning. He led me to value the quality of being honest yet never say impossible. He taught me how to benefit from failure; his inspiring guidance and unfailing support not only resolved my frustration, but excited me out of the trap to come up with something even more interesting. His unique way of supervision has made my graduate experience unexpectedly challenging and rewarding. Over the years I have learned to be a more independent and confident person, a better self. I cherish this progress as an invaluable gift from Peter that I will benefit from continuously no matter what my future pursuit will be.

I am grateful to my committee members Dr. Olga Dudko, Dr. Herbert Levine, Dr. Andrew McCammon and Dr. José Onuchic for their constructive advice on my work and constant concern and encouragement along the way.

I want to thank Dr. Terry Hwa for all his concern and advice at different stages of my PhD pursuit. I appreciate the opportunity he gave me to perform basic experiments on bacterial growth in his lab. I have learned various ideas and techniques in statistical mechanics from the excellent courses he delivered. I am also grateful to his sincere advice on how to get the best from my postdoctoral experience. I also want to thank Dr. Bo Li for his interest in my work and sustained encouragement. It was my great pleasure and honor to present at the Biophysics seminar and communicate with an applied math audience.

Interactions with experts in variety of fields have broadened my scope and led me to appreciate diverse styles and cultures of scientific research. I enjoyed the enlightening discussions with Dr. Gijsje Koenderink on active contractility of actomyosin networks. I appreciate the helpful communications with Dr. Leticia Cugliandolo on effective temperature in active matter and thank her for drawing

our attention to the numerical studies of her group. Many thanks to Dr. Jianshu Cao for his constructive comments on my work and drew the connection to mechanics of red blood cells. I also want to acknowledge Dr. Andrea Liu for hosting my visit to Penn and sharing her insight in jamming. I thank Dr. Tom Lubensky for scrutinizing my model and raising insightful questions that lent novel perspectives on my work. I thank Dr. Randy Kamien for showing me the fascinating aspects of liquid crystals. Many thanks to Dr. Jin Wang for his critical reading of my manuscript and useful discussions on the spontaneous collective motion project. I also want to thank Dr. Randy Hall for kindly giving me the glassy configurations as input to the magnetic analogy project.

I have benefited a lot from the intellectual and spiritual resources in our group. I thank Dr. Tongye Shen, who initiated the project on the cytoskeleton before I joined the group, for lending me technical and mental support at the early stage of my research and giving me cogent suggestions over the years. I feel lucky to have overlapped with Dr. Jacob Stevenson during his last year before graduation. He explained to me the intriguing ideas of glass transition theories and showed me how to be a charming scientist. I thank Apiwat Wisitsorasak, a sharp and kind young man from Thailand, for his considerate company when I visited Peter at Rice University. I am also thankful to Tracy Hogan, for being such a caring and capable assistant. Without her efficient work, I can easily imagine much delay of my progress in many things. I would like to thank all our former and current group members who had shared a memorable time with me, Arash Ashourvan, Leonardo Boechi, Anat Burger, Patricio Craig, Robert East, Joe Hegler, Ryan Hoffman, Vanessa Oklejas, Michael Prentiss, Nick Schafer, Rachel Small, Jacob Stevenson, Patrick Weinkam, Apiwat Wisitsorasak and Weihua Zheng.

Many friends have helped me keep up my spirit and enthusiasm to confront challenges and embrace possibilities. Most importantly, their passion and wisdom have injected bracing fluctuations into the self-similar days in graduate school.

Special thanks go to my husband, Ching-Kit Chan, who has been proud and supportive of my work and has shared the many uncertainties and challenges in life. As a colleague, he stimulated my thoughts with refreshing viewpoints; as

a companion, he listens to me with great patience and love. He cares more about whether I am living in the way I like than how far I have achieved work-wise. He is my source of happiness, imagination and strength.

My deepest gratitude goes to my parents, with whom I wish to spend more time. Among many other things, what I appreciate the most is that they always respect my choice and support my decision, ever since my young age. I have never felt the press of expectation, instead, I have been supported to be true to myself and be brave to try out new possibilities in pursuit of my real passion. I am so lucky to have their deep love and profound understanding.

Finally, I appreciate the financial support from the Center for Theoretical Biological Physics (CTBP) at UCSD that funded this research and provided the great weekly seminars. I have learned a lot by talking to the speakers about science and the life as a scientist. I also enjoy presenting regularly at the Journal Club, exchanging scientific ideas in "human languages".

Chapter 2, in full, is a reprint of the material as it appears in the Journal of Chemical Physics **134** 014510 (2011), S. Wang, T. Shen, and P. G. Wolynes. The dissertation/thesis author was the primary investigator and author of this paper.

Chapter 3, in full, is a reprint of the material as it appears in the Journal of Chemical Physics **135** 051101 (2011), S. Wang and P. G. Wolynes. The dissertation/thesis author was the primary investigator and author of this paper.

Chapter 4, in full, is a reprint of the material as it appears in the Proceedings of the National Academy of Sciences **108** 15184-15189 (2011), S. Wang and P. G. Wolynes. The dissertation/thesis author was the primary investigator and author of this paper.

Chapter 5, in full, is a reprint of the material as it appears in the Proceedings of the National Academy of Sciences **109** 6446-6451 (2012), S. Wang and P. G. Wolynes. The dissertation/thesis author was the primary investigator and author of this paper.

Chapter 6, in full, is a reprint of the material as it appears in the Journal of Chemical Physics **136** 145102 (2012), S. Wang and P. G. Wolynes. The dissertation/thesis author was the primary investigator and author of this paper.

VITA

2005	Bachelor of Science in Physics *cum laude*, Nanjing University, China
2007	Master of Philosophy in Physics, Hong Kong University of Science and Technology, Hong Kong
2007-2009	Graduate Teaching Assistant, University of California, San Diego, USA
2009-2012	Graduate Researcher, University of California, San Diego, USA
2012	Doctor of Philosophy in Physics, University of California, San Diego, USA

PUBLICATIONS

S. Wang and P. G. Wolynes, "Tensegrity and motor-driven effective interactions in a model cytoskeleton", *J. Chem. Phys.* **136**, 145102 (2012).

S. Wang and P. G. Wolynes, "Active contractility in actomyosin networks", *Proc. Nat. Acad. Sci. USA* **109**, 6446-6451 (2012).

S. Wang and P. G. Wolynes, "On the spontaneous collective motion of active matter", *Proc. Nat. Acad. Sci. USA* **108**, 15184-15189 (2011).

S. Wang and P. G. Wolynes, "Effective temperature and glassy dynamics of active matter", *J. Chem. Phys.* **135**, 051101 (2011).

S. Wang, T. Shen and P. G. Wolynes, "The interplay of nonlinearity and architecture in equilibrium cytoskeletal mechanics", *J. Chem. Phys.* **134**, 014510 (2011).

ABSTRACT OF THE DISSERTATION

Statistical Mechanics of the Cytoskeleton

by

Shenshen Wang

Doctor of Philosophy in Physics

University of California, San Diego, 2012

Professor Herbert Levine, Chair
Professor Peter G. Wolynes, Co-Chair

The mechanical integrity of eukaryotic cells along with their capability of dynamic remodeling depends on their cytoskeleton, a structural scaffold made up of a complex and dense network of filamentous proteins spanning the cytoplasm. Active force generation within the cytoskeletal networks by molecular motors is ultimately powered by the consumption of chemical energy and conversion of that energy into mechanical work. The resulting functional movements range from the collective cell migration in epithelial tissues responsible for wound healing to the changes of cell shape that occur during muscle contraction, as well as all the internal structural rearrangements essential for cell division. The role of the cytoskeleton as a dynamic versatile mesoscale "muscle", whose passive and ac-

tive performance is both highly heterogeneous in space and time and intimately linked to diverse biological functions, allows it to serve as a sensitive indicator for the health and developmental state of the cell. By approaching this natural nonequilibrium many-body system from a variety of perspectives, researchers have made major progress toward understanding the cytoskeleton's unusual mechanical, dynamical and structural properties. Yet a unifying framework capable of capturing both the dynamics of active pattern formation and the emergence of spontaneous collective motion, that allows one to predict the dependence of the model's control parameters on motor properties, is still needed. In the following we construct a microscopic model and provide a theoretical framework to investigate the intricate interplay between local force generation, network architecture and collective motor action. This framework is able to accommodate both regular and heterogeneous pattern formation, as well as arrested coarsening and macroscopic contraction in a unified manner, through the notion of motor-driven effective interactions. Moreover a systematic expansion scheme combined with a variational stability analysis yields a threshold strength of motor kicking noise, below which the motorized system behaves as if it were at an effective equilibrium, but with a nontrivial effective temperature. Above the threshold, however, collective directed motion emerges spontaneously. Computer simulations support the theoretical predictions and highlight the essential role played in large-scale contraction by spatial correlation in motor kicking events.

Chapter 1

Introduction

Biological versatility is most vividly illustrated by a crawling cell pushing its way through a pore or around an obstacle. This occurs while the cell constantly changes its shape and elasticity to adapt to a complex and fluctuating environment. Underlying this remarkable active mechanical performance is the ability of an eukaryotic cell to maintain its mechanical integrity and to reorganize rapidly the local structure and mechanical properties of its cytoskeleton [1]. The cytoskeleton is a dense and complex meshwork of biopolymers spanning the cytoplasm. It mainly consists of three classes of filamentous proteins having distinct stiffness: F-actin, microtubules and intermediate filaments. These proteins are further organized into higher-order assemblies by a myriad of auxiliary proteins such as crosslinkers, bundlers, capping and severing proteins, which bind to the scaffolding elements. The regulation of the kinetics of these binding proteins, the polymerization and depolymerization processes of the filaments and the action of molecular motors turn the cytoskeleton from a static carcass into a dynamic protean muscle.

A substantial specialization of the various constituents of the cytoskeleton seems to be instrumental for the cytoskeleton to fulfill its diverse tasks. In cell motility, there is the most complex orchestrated interplay of many different constituents of the actin cytoskeleton which works independently of the nucleus and most organelles of the cell. This is dramatically illustrated by the way chopped-off lamellipodia (sheet-like extensions at the cell periphery) retain their motility [2], and by the way invasive bacteria and viruses exploit parts of this cellular machin-

ery for their own propulsion [3]. *In vitro* reconstitution of "functional modules" [4] (assemblies of purified subunits) of increasing complexity seems a natural intermediate step in a bottom-up reassembly of living matter [5]. This approach is a promising way to resolve the mutually conflicting demands for simplicity, required for systematic and quantitative studies, and the need for a sufficient degree of complexity that allows a faithful representation of biological functions. The study of such simplified model systems should lead to a better understanding of the formation and stability of more complex structures of biological relevance.

Physical studies concentrating on the mechanical properties of cells have been useful in elucidating the synergies of generic physical mechanisms and specific biological regulation in establishing the overall mechanical behavior of biological cells. A remarkable universality has been revealed in the viscoelastic responses of reconstituted networks and of whole cells of different types over a wide range of timescales, reminiscent of soft glassy materials [6, 7, 8]. Meanwhile, the overall cell stiffness has been shown to be highly sensitive to cytoskeletal dysfunction, a connection which validates the use of cell shape and stiffness as efficient and reliable detectors of some diseases such as cancer [9]. On the other hand, functionally relevant heterogeneities exemplify the specificity of biochemical signaling events. One remarkable demonstration is provided by the formation of filopodia (finger-like extensions of cytoplasm sent out by the cell in motion at its leading edge), in which the local activation of various actin-binding proteins enables the dynamic generation of highly localized meso-structures [10, 11].

Cytoskeletal networks play a major role in many developmental processes, ranging from cytokinesis and cell motility to wound healing and tissue morphogenesis. Unlike macroscopic machines, within the active cellular materials there is no clear distinction between the force generators and the structural elements. Rather, the force-generating motor proteins are mixed with the elementary building blocks of cell structure on a molecular scale. An important motor-filament assembly—the microtubule-kinesin system—forms well-focused mitotic spindle poles. These are driven by a polarity sorting mechanism [12, 13] to accomplish high-accuracy segregation of replicated chromosomes into daughter cells. Networks of filamentous

actin (F-actin) and the type-II myosin motors have been identified as the major components of the cellular contractile machinery. Walking on the structural scaffold provided by an actin network, myosin-II motors themselves self-assemble into bipolar minifilaments that generate sustained sliding of neighboring actin filaments relative to each other. By carrying out such correlated motions the minifilaments reorganize the actin networks and generate tension ultimately powered by ATP hydrolysis. The formation and coalescence of actomyosin condensates to exert contractile forces have been seen in contractile rings driving cytokinesis [14, 15] and wound healing [16], and in contractile networks that deform epithelial cell layers in developing embryos [17, 18] and drive polarizing cortical flows [19, 20].

Cytoskeletal networks self-organize into highly dynamic and heterogeneous functional patterns from the interplay between active force generation by molecular motors and passive dissipation of energy in the crowded cellular interior. The formation and dynamics of contractile structures are manifested in pulsed contractions of an actomyosin network that drive epithelial sheet deformation during morphogenesis [21]. Such actomyosin aggregates also are responsible for a multistage coarsening process that occurs in a bottom-up model system for contractility [22]. In reconstituted filament-motor assemblies there arise some comparatively regular patterns such as asters, in which stiff filaments or filament bundles radiate from a common center, that resemble the mitotic spindles formed in dividing cells. On the other hand, irregular heterogeneous cluster structures have also been seen both in the actomyosin networks of *C. elegans* embryos [23] and in the minimal in vitro network model [24]. Understanding the dynamics of these pattern formation processes remains a challenge to statistical mechanical theory.

In addition to the formation of quasi-steady functional patterns, spontaneous directed motion driven by active processes is also just as crucial to biology, if not more so. Such motion is only possible because the cell is a far-from-equilibrium many-body system. Oscillations of the mitotic spindle during cell division [25] and cytoplasmic streaming [26] dramatically illustrate the nonequilibrium nature of cellular dynamics and the collective motion of a myriad of constituents. Sustained spontaneous collective motion is quite remarkable in many-body physics. Super-

fluidity and superconductivity are examples of metastable states of motion made possible by quantum statistics. The biological example provided by the cytoskeleton is seemingly quite different, leading not to infinitely long-lived states but to ones that go away when the cell is depleted of fuel. Nevertheless, like the quantum examples, the motion of the cytoskeleton is an emergent many-body phenomenon reflecting broken symmetries. Design principles for controlling artificial active materials can be learned by exploring the origin of collective directed motion for systems of many interacting biomacromolecules with motor-driven processes.

On the basis of recent experiments with simplified/reconstituted cytoskeletal networks, a number of theoretical models have emerged. These models consider, on the one hand, treating the system simply as one-component entangled solutions [27, 28] that have a surprisingly rich viscoelastic response. On the other hand, systems can be modeled as permanently crosslinked filamentous networks [29, 30, 31, 32, 33] which exhibit a universal nonlinear stiffening [34] at low to intermediate strains, as well as negative normal stresses [35] under shear being attributable to the asymmetric load responses of individual filaments. Ideas of nematic liquid crystal physics have been introduced to explain bundle formation as a structural phase transition due to liquid crystal ordering [36]. By counting the number of effective degrees of freedom, researchers have also shown that additional bending constraints yield a lower rigidity percolation threshold by eliminating some of the otherwise allowed rotational (soft) modes [37, 38]. Unlike the cytoskeleton, however, all these model systems are equilibrium materials.

Various models have been developed for active systems kept far from equilibrium by a permanent supply of mechanical energy. Many theoretical works on the cytoskeleton start from microscopic considerations at the molecular level and show how the interactions between the filaments and molecular motors can lead to the active behavior observed on macroscopic scales. This, of course, requires a good knowledge at the molecular level of the filament-motor coupling. Kruse and Jülicher [39, 40, 41] have proposed a model for the dynamics of actin bundles which leads to an expression for the tension inside the bundle and also predicts bundle instabilities. Marchetti and Liverpool [42, 43] as well as others have ex-

tended this approach to higher dimensions and studied in particular instabilities of the isotropic homogeneous filament distribution. To this end effective descriptions on macroscopic scales were derived from the microscopic equations.

Rather than beginning from a microscopic model, the hydrodynamic theory starts on macroscopic scales. Thinking of the cytoskeleton as an active polar gel allows the construction of hydrodynamic-like continuum theories. This approach circumvents the difficulties due to the nonequilibrium nature of the dynamics by modeling the gels at a coarse-grained level, subsuming all the intricate details into a set of phenomenological parameters. The equations of motion for the internal stresses as well as for local order-parameter-like quantities are constructed using generic symmetry arguments. The nonequilibrium nature of the problem is reflected in the fact that such equations of motion do not derive from an underlying free energy. This macroscopic approach has been successfully applied to systems as diverse as biological membranes [44], self-propelled colloidal objects [45, 46], bacterial colonies [47] and bird flocks [48]. In the context of the cytoskeleton, these theories have revealed the possibility of the spontaneous generation of flow in an active polar film [49] and the formation of defect structures such as vortices and asters [50]. The main limitation of the hydrodynamic theory is that this theory ineluctably considers only large length scales and long time scales. Moreover, the rate and strength of motor-induced force exchange among the filaments is controlled by phenomenological parameters whose dependence on biochemical motor activity is not known. Relating model parameters to microstructures remains a challenging theoretical task. In this dissertation I attempt to construct a microscopic model and provide a unifying theoretical framework capable of capturing both the active pattern formation and the emergence of spontaneous collective motion, with an explicit dependence of the control parameters on the motor properties.

The "cat's cradle" model [51] was introduced by Shen and Wolynes to study the statistical mechanics of a collection of buckling bonds connecting point nodes sitting on a regular lattice. Here I extend the model to treat the cytoskeleton as a crosslinked amorphous network of nonlinear elastic filaments with excluded volume. The nonlinear elasticity of individual filaments allows them to stiffen under

strain thereby preventing large deformations that could threaten tissue integrity. On the other hand, the buckling instability under compressive load is essential for large-scale contraction that makes possible wound healing and morphogenesis. Rather than keep track of the filament degrees of freedom based on the contour of the filaments using a continuum description, we follow the motion of the crosslinks or the nodes of the network. This model encodes the effect of the filaments (i.e. their asymmetric load response) via the pairwise interaction between the bonded nodes. A hard-sphere repulsion between all the node pairs accounts for the excluded volume of the filaments and binding protein aggregates. The caging effect due to repulsive neighbors comes into play at high concentrations of the nodes and is essential for the glassy dynamics observed experimentally [7, 8].

Motors do not explicitly enter our model; instead, they are exemplified as generating kicks on the motorized crosslinks or nodes. Spatially *uncorrelated* kicks on individual nodes imitate the effects of unidirectional stepping of processive motors (e.g. kinesin) along the filament tracks (e.g. microtubules). Spatially *anti-correlated* kicks on motor-bonded node pairs, in contrast, mimic the myosin-driven relative sliding of neighboring actin filaments, in which the nodes on either filament are pulled toward each other. It will be shown that uncorrelated isotropic kicks are responsible for a transition that leads to streaming flows as seen in *Drosophila* oocyte where the cytoskeleton is driven by kinesin motors [52]. On the other hand, spatial anti-correlation in motor kicks is shown to be crucial for there to be active contractility as is observed in actomyosin networks in vitro [53] and in vivo [21].

Our coarse-grained models are completely microscopic but they bear some resemblance to the macroscopic approach adopted by Levine and MacKintosh [54, 55] that introduces force dipoles into an elastic continuum where motor unbinding kinetics leads to enhanced low-frequency stress fluctuations. In the microscopic model the network connectivity and motor distribution over the bonds of the network are quenched once initially assigned, so that the nonequilibrium dynamics and structures predicted by our model arise solely from the intrinsic activity of motors firmly built into the network driving correlated motions stochastically. This assumption is in line with the fact that the in vitro structures are irreversibly

assembled because many protein factors found in vivo that allow fast pattern renewals are left out of the reconstitution. Thus disassembly of contractile structures and the transient action of actin crosslinking proteins, while important in vivo, are absent in the simplified in vitro systems. Our model highlights the key role played by the motor susceptibility, a parameter that characterizes how sensitively the motors respond to imposed forces. The coupling between motor kinetics and the structure leads to a double-way feedback: Motor action induces structural changes of the network; these changes in turn modify the local mechanical environment of the motors, again, changing the load-dependent motor response. Despite being constructed in the context of the cytoskeleton, this model may have wide implications for variety of systems having nonlinear interactions and mechanochemical coupling, since motors and nodes can represent different objects in different circumstances.

Chapter 2 explores the interplay between nonlinear elasticity of individual filaments and the tunable network architecture and how this interplay establishes equilibrium cytoskeletal mechanics. Mean field theories are used to determine the Debye-Waller factor of localized particles. Combining these results with a density functional formulation for the free energy allows us to identify diverse thermodynamically stable mechanical phases the model cytoskeleton can take on and the possible transitions between them. These transitions are controlled by biophysical parameters in the microscopic model. The equivalence of our approach and the replica method in spin glass theory makes possible an estimation of the glass transition densities using the concept of configurational entropy, whose smallness in value indicates the paucity of possible configurational states and thus monitors a deep descent into the glassy regime. A martensite-like structural phase also arises from instability of homogeneous states in a floppy network. This heterogeneous pattern is characterized by adjacent spatial domains with uncorrelated orientations of net motion, as confirmed by molecular dynamics simulations.

Having achieved some understanding of the equilibrium phase behavior of the model cytoskeleton, we enquire as to how the nonequilibrium fluctuations and responses due to active processes can be captured by generalized thermodynamic

concepts. In chapter 3 we pursue this possibility by using a master equation description for active matter in which motors power configurational changes as in the cytoskeleton. A systematic expansion of the many-body master equation yields a description of the steady state and low-frequency responses in terms of an effective temperature. The effective temperature not only allows a simple rescaling of the equilibrium phase diagrams to be used for nonequilibrium motorized systems, it also suggests a description of aging in active matter which has become kinetically jammed.

Partially inspired by cytoplasmic streaming, in which a collective particle flow circulating matter and information all over the cell arises driven by motor-generated active stresses, we consider the question in general: How does the collective motor action which is stochastic in nature give rise to spontaneous directed motion reflecting broken symmetries? We attempt to address this question in chapter 4 by pursuing the systematic expansion of the many-body master equation to higher order in step size of motor kicks. Mean field theories and variational stability analysis reveal a threshold motor kick size for such collective flow: Systems driven by small-step motors can be described by an effective temperature and are thus quiescent, above the threshold, however, streaming flow emerges spontaneously. Depending on network architecture and motor susceptibility, inhomogeneous and oscillating patterns may also arise. Motors that respond with a negative susceptibility lead to an apparent negative temperature system in which beautiful structures form resembling the asters seen in cell division. The proposed mechanism for collective directed motion is robust to various forms of interactions, as long as three generic conditions are fulfilled: (1) broken translational symmetry and the corresponding elastic restoring force providing the rigidity of the macroscopic state; (2) sufficiently strong agitation triggering dynamic instability about the quiescent state; (3) coupling between chemical kinetics of the active elements and the forces exerted on them that promotes cooperativity and thus coherence in motion. This mechanism might be responsible for cortical flow on subcellular scale and relevant for collective cell migration in multicellular tissues.

Active contractility in actomyosin networks observed both in vitro and in

vivo drew our attention to the possibility that spatial correlation in motor kicking events would dramatically modify the structural development and dynamics of the cytoskeleton. Chapter 5 presents a microscopic model that incorporates two essential aspects of actomyosin self-organization: the asymmetric load responses of individual actin filaments and the anti-correlated motor-driven events mimicking myosin-induced filament sliding. This model is shown to capture the formation and dynamics of contractile structures and is shown to agree with the observed dependence of active contractility on microscopic parameters, in particular, that contractility occurs only above a threshold motor concentration and within a window of network connectivity. *In silico* realization of this model vividly demonstrates how cooperative action of load-resisting motors in a force-percolating structure integrates local buckling events into a global contractile state via an active coarsening process, in contrast to the flow transition driven by uncorrelated kicks of susceptible motors.

Chapter 6 provides a theoretical framework to investigate the intricate interplay between local force generation, network connectivity, and collective action of molecular motors. This framework is capable of accommodating both regular and heterogeneous pattern formation, arrested coarsening and macroscopic contraction in a unified manner. Simulation studies confirm the theoretical picture that a nonequilibrium many-body system driven by correlated motor kicks can behave as if it were at an effective equilibrium, but with modified interactions that account for the correlation of the motor-driven motions of the actively bonded nodes. The notion of effective interaction provides a natural explanation for the diverse forms of active patterning: An effective short-range attraction drives the aggregation and coalescence of actomyosin condensates, whereas an effective repulsion allows the formation of sustained aster patterns.

Our theory is not yet a final theory of everything "cytoskeletal". So I close by discussing some immediate extensions and pointing out future opportunities in chapter 7.

Even though we have not provided all the answers, we hope these studies help sharpen the questions and nucleate starting points for further investigations.

Bibliography

[1] Howard, J. *Mechanics of Motor Proteins and the Cytoskeleton*, (Sinauer Assoc., Sunderland, MA, 2001).

[2] Verkhovsky, A. B., Svitkina, T. M. & Borisy, G. G. Self-polarization and directional motility of cytoplasm. *Curr. Biol.* **9,** 11–20 (1999).

[3] Theriot, J. A., Mitchison, T. J., Tilney, L. G. & Portnoy, D. A. The rate of actin-based motility of intracellular Listeria monocytogenes equals the rate of actin polymerization. *Nature* **357,** 257–260 (1992).

[4] Hartwell, L. H., Hopfield, J. J., Leibler, S. & Murray, A. W. From molecular to modular cell biology. *Nature* **402,** 47–52 (1999).

[5] Bausch, A. R. & Kroy, K. A bottom-up approach to cell mechanics. *Nat. Phys.* **2,** 231–238 (2006).

[6] Fabry, B., Maksym, G. N., Butler, J. P., Glogauer, M., Navajas, D. & Fredberg, J. J. Scaling the microrheology of living cells. *Phys. Rev. Lett.* **87,** 148102 (2001).

[7] Bursac, P., Lenormand, G., Fabry, B., Oliver, M., Weitz, D. A., Viasnoff, V., Butler, J. P., & Fredberg, J. J. Cytoskeletal remodelling and slow dynamics in the living cell. *Nature Mater.* **4,** 557–561 (2005).

[8] Zhou, E. H. *et al.* Universal behavior of the osmotically compressed cell and its analogy to the colloidal glass transition. *Proc. Natl. Acad. Sci. USA* **106,** 10632–10637 (2009).

[9] Guck, J. *et al.* Optical deformability as an inherent cell marker for testing malignant transformation and metastatic competence. *Biophys. J.* **88,** 3689–3698 (2005).

[10] Svitkina, T. M. *et al.* Mechanism of filopodia initiation by reorganization of a dendritic network. *J. Cell Biol.* **160,** 409–421 (2003).

[11] Small, J. V., Stradal, T., Vignal, E. & Rottner, K. The lamellipodium: where motilitiy begins. *Trends Cell Biol.* **12,** 112–120 (2002).

[12] Heald, R., Tournebize, R., Blank, T., Sandaltzopoulos, R., Becker, P., Hyman, A. & Karsenti, E. Self-organization of microtubules into bipolar spindles around artificial chromosomes in Xenopus egg extracts. *Nature* **382,** 420–425 (1996).

[13] Surrey, T., Nédélec, F., Leibler, S. & Karsenti, E. Physical properties determining self-organization of motors and microtubules. *Science* **292,** 1167–1171 (2001).

[14] Vavylonis, D., Wu, J., Hao, S., OShaughnessy, B. & Pollard, T. Assembly mechanism of the contractile ring for cytokinesis by fission yeast. *Science* **319,** 97–100 (2008).

[15] Moores, S., Sabry, J. & Spudich, J. Myosin dynamics in live Dictyostelium cells. *Proc. Natl. Acad. Sci. USA* **93,** 443–446 (1996).

[16] Mandato, C. & Bement, W. Contraction and polymerization cooperate to assemble and close actomyosin rings around Xenopus oocyte wounds. *J. Cell Biol.* **154,** 785–797 (2001).

[17] Blanchard, G. B., Murugesu, S., Adams, R. J., Martinez-Arias, A. & Gorfinkiel, N. Cytoskeletal dynamics and supracellular organisation of cell shape fluctuations during dorsal closure. *Development* **137,** 2743–2752 (2010).

[18] Franke, J., Montague, R. & Kiehart, D. Nonmuscle myosin II generates forces that transmit tension and drive contraction in multiple tissues during dorsal closure. *Curr. Biol.* **15,** 2208–2221 (2005).

[19] Hird, S. & White, J. Cortical and cytoplasmic flow polarity in early embryonic cells of Caenorhabditis elegans. *J. Cell Biol.* **121,** 1343–1355 (1993).

[20] Mayer, M., Depken, M., Bois, J. S., Jülicher, F. & Grill, S. W. Anisotropies in cortical tension reveal the physical basis of polarizing cortical flows. *Nature* **467,** 617–621 (2010).

[21] Martin, A. C., Kaschube, M. & Wieschaus, E. F. Pulsed contractions of an actin-myosin network drive apical constriction. *Nature* **457,** 495–499 (2009).

[22] Silva, M. S., Depken, M., Stuhrmann, B., Korsten, M., MacKintosh, F. C. & Koenderink, G. H. Active multistage coarsening of actin networks driven by myosin motors. *Proc. Natl. Acad. Sci. USA* **108,** 9408–9413 (2011).

[23] Munro, E., Nance, J. & Priess, J. R. Cortical flows powered by asymmetrical contraction transport PAR proteins to establish and maintain anterior-posterior polarity in the early *C. elegans* embryo. *Dev. Cell* **7,** 413–424 (2004).

[24] Köhler, S., Schaller, V. & Bausch, A. R. Structure formation in active networks. *Nat. Mater.* **10,** 462–468 (2011).

[25] Pecreaux, J. *et al.* Spindle oscillations during asymmetric cell division require a threshold number of active cortical force generators. *Curr. Biol.* **16,** 2111–2122 (2006).

[26] Bray, D. *Cell Movements*, (Garland, New York, 2001).

[27] Morse, D. C. Viscoelasticity of tightly entangled solutions of semiflexible polymers. *Phys. Rev. E* **58,** 1237–1240 (1998).

[28] Isambert, H. & Maggs, A. C. Dynamics and rheology of actin solutions. *Macromolecules* **29,** 1036–1040 (1996).

[29] MacKintosh, F. C., Käs, J. & Janmey, P. A. Elasticity of semiflexible biopolymer networks. *Phys. Rev. Lett.* **75,** 4425–4428 (1995).

[30] Satcher, R. L. & Dewey, C. F. Theoretical estimates of mechanical properties of the endothelial cell cytoskeleton. *Biophys. J.* **71,** 109–118 (1996).

[31] Kroy, K. & Frey, E. Force-extension relation and plateau modulus for wormlike chains. *Phys. Rev. Lett.* **77,** 306–309 (1996).

[32] Wilhelm, J. & Frey, E. Elasticity of stiff polymer networks. *Phys. Rev. Lett.* **91,** 108103 (2003).

[33] Onck, P. R., Koeman, T., van Dillen, T. & van der Giessen, E. Alternative explanation of stiffening in cross-linked semiflexible networks. *Phys. Rev. Lett.* **95,** 178102 (2005).

[34] Storm, C., Pastore, J. J., MacKintosh, F. C., Lubensky, T. C. & Janmey, P. A. Nonlinear elasticity in biological gels. *Nature* **435,** 191–194 (2005).

[35] Janmey, P. A., McCormick, M. E., Rammensee, S., Leight, J. L., Georges, P. C. & MacKintosh, F. C. Negative normal stress in semiflexible biopolymer gels. *Nat. Mater.* **6,** 48–51 (2007).

[36] Borukhov, I., Bruinsma, R. F., Gelbart, W. M. & Liu, A. J. Structural polymorphism of the cytoskeleton: A model of linker-assisted filament aggregation. *Proc. Natl. Acad. Sci. USA* **102,** 3673–3678 (2005).

[37] Wyart, M., Liang, H., Kabla, A. & Mahadevan, L. Elasticity of floppy and stiff random networks. *Phys. Rev. Lett.* **101,** 215501 (2008).

[38] Broedersz, C. P., Mao, X., Lubensky, T. C. & MacKintosh, F. C. Criticality and isostaticity in fibre networks. *Nat. Phys.* **7,** 983–988 (2011).

[39] Kruse, K. & Jülicher, F. Actively contracting bundles of polar filaments. *Phys. Rev. Lett.* **85,** 1778 (2000).

[40] Kruse, K., Camalet, S. & Jülicher, F. Self-propagating patterns in active filament bundles. *Phys. Rev. Lett.* **87,** 138101 (2001).

[41] Kruse, K. & Jülicher, F. Self-organization and mechanical properties of active filament bundles. *Phys. Rev. E* **67,** 051913 (2003).

[42] Liverpool, T. B. & Marchetti, M. C. Instabilities of isotropic solutions of active polar filaments. *Phys. Rev. Lett.* **90,** 138102 (2003).

[43] Ahmadi, A., Liverpool, T. B. & Marchetti, M. C. Nematic and polar order in active filament solutions. *Phys. Rev. E* **72,** 060901(R) (2005).

[44] Manneville, J.-B., Bassereau, P., Ramaswamy, S. & Prost, J. Active membrane fluctuations studied by micropipet aspiration. *Phys. Rev. E* **64,** 021908 (2001).

[45] Simha, R. A. & Ramaswamy, S. Hydrodynamic fluctuations and instabilities in ordered suspensions of self-propelled particles. *Phys. Rev. Lett.* **89,** 058101 (2002).

[46] Hatwalne, Y., Ramaswamy, S., Rao, M. & Simha, R. A. Rheology of active-particle suspensions. *Phys. Rev. Lett.* **92,** 118101 (2004).

[47] Dombrowski, C., Cisneros, L., Chatkaew, S., Goldstein, R. E. & Kessler, J. O. Self-concentration and large-scale coherence in bacterial dynamics. *Phys. Rev. Lett.* **93,** 098103 (2004).

[48] Long-range order in a two-dimensional dynamical XY model: How birds fly together. *Phys. Rev. Lett.* **75,** 4326–4329 (1995).

[49] Giomi, L., Marchetti, M. C. & Liverpool, T. B. Complex spontaneous flows and concentration banding in active polar films. *Phys. Rev. Lett.* **101,** 198101 (2008).

[50] Kruse, K., Joanny, J. F., Jülicher, F., Prost, J. & Sekimoto, K. Asters, vortices, and rotating spirals in active gels of polar filaments. *Phys. Rev. Lett.* **92,** 078101 (2004).

[51] Shen, T. & Wolynes, P. G. Statistical mechanics of a cat's cradle. *New J. Phys.* **8,** 273 (2006).

[52] Serbus, L. R., Cha, B. J., Theurkauf, W. E. & Saxton, W. M. Dynein and the actin cytoskeleton control kinesin-driven cytoplasmic streaming in Drosophila oocytes. *Development* **132,** 3743–3752 (2005).

[53] Bendix, P. M., Koenderink, G. H., Cuvelier, D., Dogic, Z., Koeleman, B. N., Briehera, W. M., Fielda, C. M., Mahadevan, L. & Weitz, D. A. A quantitative analysis of contractility in active cytoskeletal protein networks. *Biophys. J.* **94,** 3126–3136 (2008).

[54] MacKintosh, F. C. & Levine, A. J. Nonequilibrium mechanics and dynamics of motor-activated gels. *Phys. Rev. Lett.* **100,** 018104 (2008).

[55] Levine, A. J. & MacKintosh, F. C. The mechanics and fluctuation spectrum of active gels. *J. Phys. Chem. B* **113,** 3820–3830 (2009).

Chapter 2

The interplay of nonlinearity and architecture in equilibrium cytoskeletal mechanics

2.1 Introduction

The cytoskeleton is a crowded network of dynamic filamentous protein polymers that collaborate with diverse binding proteins and molecular motors to form nature's most marvellous active material [1]. All eukaryotic cells are known to contain a well-developed cytoskeleton, and even bacteria have been found to contain a diverse set of proteins capable of forming structural filaments [2]. Actin is a major constituent of the cytoskeletal network that participates in such widely differing processes as blood clotting, egg fertilization, intestinal absorption and tumor invasion. A common theme of many substantial experimental efforts [3, 4, 5, 6, 7] is the role of actin filaments in maintaining cell architecture and generating movement.

In vitro, actin can polymerize to form long rigid filaments (F-actin), with a diameter around 7 nm and contour length up to 20 μm. The *in vivo* cytoskeletal network, however, is regulated and controlled not only by the concentration of F-actin, but also by accessory proteins that bind to F-actin. Nature provides a host of actin-binding proteins (ABPs) with versatile functions that offer the necessary

variations for the part actin has to play [8]: Cross-linking proteins form filament bundles or isotropic gels, whereas capping proteins and/or filament-severing proteins regulate actin polymerization under specific salt conditions and thus control the average length of F-actin. Experiments show, for example, that actin-binding protein functions to stabilize cortical actin *in vivo* and is required for efficient cell locomotion [9]. Rheological experiments on simplified networks and living cells demonstrate that even the most basic mechanical properties of cytoskeletal materials are sensitive to specific architectural details, including filament and cross-link density, connectivity, and orientation [10].

Unlike flexible polymers, where changes in cross-link density typically do not markedly affect the elasticity, small changes in the concentration of cross-linking actin-binding proteins do dramatically alter the elasticity of F-actin networks [11]. As materials, *in vitro* networks of cytoskeletal filaments exhibit several unusual mechanical properties, including a highly nonlinear elastic response [7, 12] and negative normal stresses [13]. Another noteworthy observation is the buckling of actin stress fibers that occurs upon rapid shortening [14], which demonstrates the instability of a prestressed actin network under compression.

A refined experimental route to understanding cytoskeletal structures in terms of their molecular components is to reconstitute these structures from purified proteins. *In vitro* reconstitution provides the capability to study the emergence of micrometer-scale function from numerous molecular-scale interactions. A recent reconstitution of contractility in a simplified model system, composed of purified F-actin, muscle myosin II motors and α-actinin cross-linkers, has shown that contractility occurs above a threshold motor concentration (one myosin filament for every 30 actin filaments) and within a window of cross-link concentrations ($90-270$ α-actinin dimers per actin filament) [15]. It is somewhat unexpected that at high cross-link densities the bundled networks do not contract on the experimental timescale of an hour. This seems to imply a dramatic slow-down of cytoskeletal kinetics due to the steric constraints associated with increasing crowding.

The cytoskeleton in different organisms or even during different stages of the cell cycle exhibits a rich variety of viscoelastic properties [16, 17]. To ac-

commodate both the adaptive behavior of dynamic remodeling, and the ability to stabilize and be resistant to deformation, the cytoskeleton should exhibit at least two mechanical phases: a plastic/fluid phase for internal reorganization of the cell, and an elastic/solid phase for mechanical support and tension transmission.

In contrast to the strain-stiffening behavior [18] in response to a *sustained* stretching of cells or reconstituted cross-linked actin gels, measurements on the responses to a *transient* stretching in the living cells [19] demonstrate that the cell will fluidize in response to the stretch, but will resolidify subsequent to this fluidization. This ability seems to be insensitive to molecular details, and instead only depends on the proximity of the thermodynamic conditions of the cell to a solid-like state before the stretch. This observation implied that in addition to specific signalling pathways, some response mechanisms are most likely controlled by non-specific actions of a slowly evolving network of physical forces. On the other hand, the universal behavior observed in the osmotically compressed cell [20] highlighted the crowding-induced stiffening of the cytoplasm as the solid volume fraction is sufficiently high, and suggested an analogy to the colloidal glass transition.

In an attempt to understand the interplay between the individual filament properties and network architecture, we study in this paper the equilibrium properties of a model cytoskeleton as an amorphous network of rigidly cross-linked nonlinear strings which also contains nodes with excluded volume. We incorporate the nonlinearity of interaction due to bucklable filaments into the force law, and characterize the cytoskeletal architecture by cross-link density and network connectivity. A mean-field level investigation, within the framework of the self-consistent phonon method and a density functional formulation, reveals a diversity of mechanical phases and a number of possible transitions in between which can be controlled by biophysical parameters. This phase diagram may shed light on our understanding of cytoskeletal remodeling in response to mechanical or chemical stimuli. We also show the possibility of a glass transition in this model system and how the network connectivity modulates the transition densities.

2.2 Model and method

2.2.1 Model

We model the F-actin bundles as individual nonlinear elastic strings; they are capable of resisting tensile forces by stretching (beyond the relaxed length L_e), but are unstable under compression so that these forces may cause the strings to buckle. The actin-binding proteins bundle and crosslink F-actin to form an amorphous network. To account for the excluded volume of F-actin and the ABP aggregates, to the lowest order, we model the network as being crosslinked by hard "beads"; each bead serves as a compact rigid subunit that concentrates the volume of the F-actin and ABP aggregates centered on that bead. The network elasticity then comes from the remaining inter-bead F-actin molecules which are now taken to be volumeless. To higher order, the elasticity within the beads can also be included by introducing softness in the repulsion. In this way we effectively decompose the inter-bead interaction into purely excluded volume and nonlinear elastic contributions, and the model potential energy $V(r)$ between a nearest-neighbor pair of beads is given by

$$\beta V(r) = A\,\Theta(d-r) + \frac{\beta\gamma}{2}(r-L_e)^2\,\Theta(r-L_e)\,, \tag{2.1}$$

where $\Theta(x)$ is the Heaviside step function. The limit $A \to \infty$ indicates the hard-sphere (HS) repulsion, while γ measures the rigidity of the inter-bead F-actin. Temperature dependence enters this model only via the combination $\beta\gamma$ where $\beta = 1/k_BT$. Here d denotes the HS diameter of the beads and L_e marks the onset of elasticity. Thus $L_e > d$ define a buckling regime ($d < r < L_e$) where no load is imposed. We show a sketch of the model system (Fig. 2.1a) and a schematic of the nonlinear interaction (Fig. 2.1b).

We incorporate the filament nonlinearity to the extent that it effectively encodes the asymmetric response of the filaments to stretch and to compression; in this sense, our model is more "coarse-grained" than the well-studied "semi-flexible fiber" model [21]; the latter treats the bending degrees of freedom of F-actin based on the contour of the filaments using a continuum description. This bending

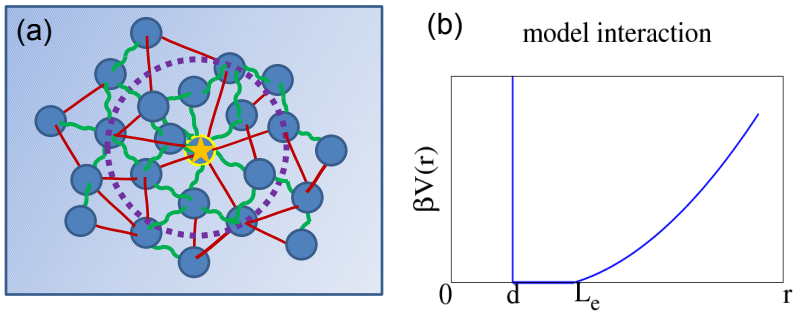

Figure 2.1: Illustrations of the model system and the nonlinear interaction. (a) The beads (blue spheres) interconnect the F-actin (red straight or green squiggly lines) into an amorphous network. Red straight lines stand for tense/stretched bonds and green squiggly lines for loose/buckled bonds. The arbitrarily chosen central particle (yellow-stared) is connected with its nearest neighbors within the first shell of the radial distribution function (the dotted purple circle). (b) Nearest-neighbor interaction versus radial separation.

effect, stated in our language of inter-bead interaction, essentially introduces a finite resistance/restoring force to compression in our originally buckling regime. It can be easily incorporated, yet we do not expect any qualitative modification on the mean-field level predictions made by our current model.

Similar buckling bonds were used to study the statistical mechanics of a "cat's cradle" built on a regular lattice by two of us several years ago [22]. Here we also include a HS repulsion to account for the excluded volume of the F-actin and ABP aggregates, and also assume the cytoskeleton adopts an aperiodic amorphous structure characteristic of the disorder of biological cytoskeletal networks. Thus in our model system, localization is achieved not only at a high concentration of beads via hard-core repulsions (topological caging), but also will occur upon network expansion due to bond stretching. The interplay between the nonlinearity of interaction due to bucklable bonds and the network architecture renders the thermodynamic state diagram nontrivial in terms of diverse mechanical phases. These equilibrium phases include persistent uniform liquid-like states, regions with a coexistence of frozen and liquid phases, and the possibility of a martensitic-like phase transition that signals a spontaneous symmetry breaking.

The average length of F-actin in an *in vitro* network can be adjusted by controlling the concentration of capping proteins (for example the concentration of gelsolin); a higher molar ratio of capping protein to actin results in shorter F-actin on average. Increasing the crosslink concentration promotes the formation of F-actin and ABP aggregates [23], and in turn increases the bead density. The bead density determines the average spacing between the beads, or equivalently, the average end-to-end distance of F-actin (r). When $r < L_e$ the elasticity of the fiber is entropic in origin, whereas the intrinsic elastic modulus of the fiber dominates when $r > L_e$. The effective stiffness of the interbead F-actin ($\beta\gamma$) is also variable; it is enhanced when filaments are bundled together to form structures with larger diameters [24]. Thermal fluctuations play a smaller role as filaments become stiffer.

To get a feeling about how the relevant biophysical parameters work out in our model system, we can first estimate the bead density ρ from experimental actin concentration. The typical actin concentration used for *in vitro* networks is 23.8μM which, if we assume the actin monomers to be spheres of diameter 5nm, corresponds to a volume fraction of 0.9×10^{-3}. The ABPs take up negligibly small volume compared to that taken up by actin. We further take the bead size to be 1μm and the F-actin as slender rods of cross section 5nm $\times$ 5nm, then if each bead concentrates five F-actin of length 6μm, $\rho = 1.2$ is needed to reach the given volume fraction; if five F-actin of length 10μm per bead then $\rho = 0.9$ (taking the bead diameter d to be the length unit). Thus ρ is adjustable, ranging from 0.1 to 1.4, by varying actin concentration and/or crosslinking properties. Since the filament aggregates are not perfectly dense-packed within the bead, they only take up a portion of the assumed bead volume; the modeled hard-sphere repulsion between the beads may overestimate the excluded volume effect. Yet the qualitative phase behavior of this model system should not be altered. In a first approximation, the cytoskeleton determines the mechanical properties of a cell; since the elastic modulus of a cell is in the range of 10^3 Pa, the corresponding effective stiffness $\beta\gamma$ is then estimated to be between 1 and 10 as converted into our model parameters. (The characteristic bead size is $d = 1\mu$m.)

2.2.2 Mean field approximations and the self consistent phonon (SCP) method

Instead of treating the bending degrees of freedom of F-actin directly, we focus on the motion of individual beads, located on the vertices of the network, in order to find the nonlinear elasticity as the bead density is varied. In the mean-field spirit, we tag a given bead as the central particle, and study its stability/response to the local mechanical environment.

We build the model system on top of an amorphous structure. In contrast to a regular lattice that usually has a unique equilibrium configuration as well as a definite coordination number for a specific lattice structure, amorphous systems must be appropriately averaged over non-vibrational disorder in the lattice which we take as quenched. A further mean-field approximation will be made in the present analysis to avoid detailing the configurational complexity of a random network. We will summarize the underlying topology of the amorphous solid in an assumed isotropic pair distribution function $g(r)$ for the fiducial configurations of the system. Such a treatment has also been used for molecular structural glasses. We then define nearest neighbors as those beads that sit within the "first shell", i.e., up to the first minimum of the equilibrium radial distribution function $g(r)$, and assume that interaction only exists between nearest-neighbor pairs.

For liquids above the melting point, g_{HS} is well described by the Percus-Yevick approximation; the Verlet-Weis correction improves the behavior of $g(r)$ near the core and dampens its oscillations at large r, giving accurate modifications especially at high densities [25]. We follow the procedures of Verlet and Weis, and note that coordination number in an amorphous structure depends on particle concentration, because the amplitude and phase of the oscillations in radial distribution vary with number density/packing fraction of the particles (See Fig. 2.2(a)). As shown in Fig. 2.2(b), an increasing number of nearest neighbors are accommodated within the first shell when particles are packed denser. This increase is almost linear when ρ is low, and slows down as ρ approaches 0.6; the modest increase above densities of 0.8 is bounded by the random close packing value of the coordination number which is around 14.

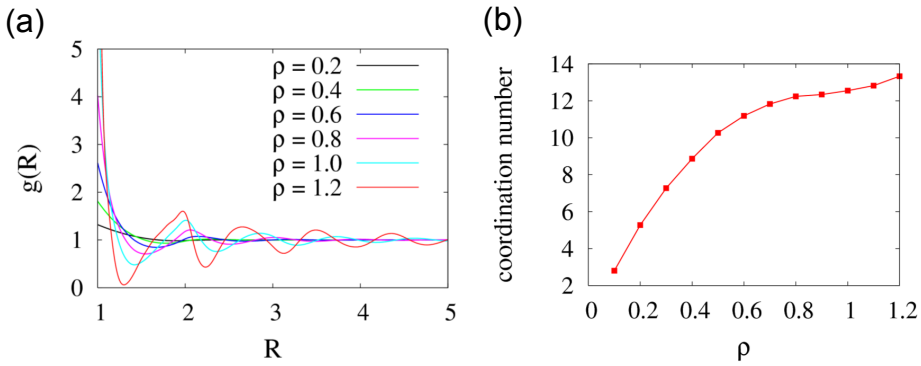

Figure 2.2: (a) Radial distribution function $g(R)$ vs the radial separation R for a series of particle density ρ. As density increases, oscillatory amplitude gets larger along with a phase shift toward the core. (b) Coordination number vs particle density.

In the context of our model network, the amorphous topology effectively contains the physical aspects of bond breaking and/or ABP detachment upon network expansion. These aspects were absent in the lattice setting which was studied earlier: as the density of beads decreases (or equivalently as the network expands), coordination number drops off resulting in a smaller number of interacting neighbors or an effectively weaker network connectivity, even though the bond connections between each nearest-neighbor pair are assumed to be permanent at each given bead density.

As an approach of thermal stability analysis in an equilibrium system, the SCP theory was first developed to treat the anharmonic effects of hard-sphere crystals. The basic idea is to introduce a reference harmonic system, and then obtain the effective potential felt by each tagged particle, by averaging the pair interaction over the assumed Gaussian fluctuations from all its neighbors. This procedure should give back the assumed harmonic potential of the typical particle. The resulting coupled set of self-consistent equations allows an iterative scheme to determine the generally site-dependent force constants. Among several schemes, Fixman's SCP method based on a systematic expansion in Hermite functions has proven an efficient and especially robust procedure [26]. Recently, this technique

has been applied to network glasses [27], and also by two of us to study motorized particle assembly [28] to analyze the far-from-equilibrium dynamics like that of the living protoplasm using a local feedback scheme.

We apply the SCP method to quantify the responses of various mechanical phases under varying physical conditions. At low concentration of beads, the effective attraction due to stretched springs dominates, thus the tagged particles are localized by "bond trapping"; whereas in the high concentration limit, HS repulsion dominates and results in a glassy/jammed state owing to "topological caging". To investigate both localized phases and the intermediate states that bridge the transition, we make a Gaussian local density profile ansatz with a single parameter, i.e. we describe the time-averaged density configuration as a sum of Gaussians representing thermal vibrations of particles about the fiducial sites

$$\rho(\vec{r}) = \sum_i \left(\frac{\alpha_i}{\pi}\right)^{3/2} e^{-\alpha_i\left(\vec{r}-\vec{R}\right)^2}. \tag{2.2}$$

In the present work, the force constants (inverse mean squared displacements or localization strengths) $\{\alpha_i\}$ will all be taken to be equal, but it is not difficult to allow spatial variation [29], i.e., dependence on the index i.

In the independent-oscillator version of the SCP theory, the effective potential between two interacting particles is given by

$$e^{-\beta V^{eff}(|\vec{r}-\vec{R}'|;\alpha)} = \left(\frac{\alpha}{\pi}\right)^{3/2} \int d\vec{r}' e^{-\beta\frac{1}{2}V(\vec{r}-\vec{r}')} e^{-\alpha(\vec{r}'-\vec{R}')^2}, \tag{2.3}$$

which may be explicitly written as

$$\begin{aligned} e^{-\beta V^{eff}(R;\alpha)} &= \sqrt{\frac{\alpha}{\pi}}\frac{1}{R}\int_0^\infty dw w e^{-\frac{1}{2}\beta V(w)} \\ &\times \left[e^{-\alpha(w-R)^2} - e^{-\alpha(w+R)^2}\right]. \end{aligned} \tag{2.4}$$

Here, R denotes the averaged equilibrium separation between interacting particles, and α represents the homogeneous localization strength.

Taylor expansion of the effective interaction up to the second order gives a self-consistent relation for α:

$$\alpha = \frac{\rho}{6}\int_{\text{"1st shell"}} d^3\vec{R}\, g(\rho,R)\, Tr\left[\nabla\nabla\beta V^{eff}(R,\alpha)\right], \tag{2.5}$$

or

$$\alpha = \frac{2\pi}{3}\rho \int_1^{R^*} dR\, R^2 g(\rho, R) \nabla^2 \beta V^{eff}(R, \alpha)\,. \tag{2.6}$$

Here R^* marks the position of the first minimum of the radial distribution function $g(R)$. The HS diameter d, as the lower limit, is taken to be the unit of length.

2.2.3 Thermodynamic ramifications of our model system

We shall show in a moment that in our model system—a rigidly cross-linked nonlinear-elastic network—there exist at least two different localized phases: one modestly localized phase describes the weakly trapped motion due to bond stretching. We refer to this state as the "liquid-like state", in view of its considerable mobility and small localization strength (α_{liq}). The other more strongly localized state corresponds to the jammed motion within topological cages of neighbors. This solution depicts a "glassy state" exhibiting highly restricted vibrations (α_{gl}).

Traditionally, microscopic treatments of liquids take the view that since the liquid structure is dominated by repulsive forces, it is desirable to develop perturbation theories based on a HS reference system and then find the optimal parameters for it. In this spirit, the Helmholtz free energy can be obtained by adding a first-order perturbation to the free energy of the corresponding HS system. On the other hand, the Carnahan-Starling equation of state gives accurate values of the reference free energy at moderately high densities. In sum, the free energy for the liquid-like state is given by

$$\begin{aligned} f_{liq} \;&\equiv\; \frac{\beta A_{liq}}{N} = \left(\ln \rho\Lambda^3 - 1\right) + \int_0^{\eta} \left(Z_{CS}(\eta') - 1\right) \frac{d\eta'}{\eta'} \\ &+\; \rho \int_{1st\ shell} d\vec{R}\, g(\eta, R) \\ &\times\; \left[\beta V^{eff}_{model}(R, \alpha_{liq}; \beta\gamma, L_e) - \beta V^{eff}_{HS}(R, \alpha_{liq})\right]. \end{aligned} \tag{2.7}$$

Here the first term gives the entropic cost when all the nearest-neighbor pairs are bonded, with Λ denoting the thermal wavelength. The second term is the excess free energy of the HS reference system where the compressibility factor Z is given by Carnahan-Starling(CS) equation of state. The last term involves the energetic

contributions from the attraction due to bond stretching; note the HS part is carefully deducted.

We use SCP theory to describe the free energy of glassy configurations [30, 31]. The expression we use for an individual glassy configuration is

$$\begin{aligned} f_{gl} &\equiv \frac{\beta A_{gl}}{N} = \rho \int_{1st\ shell} d\vec{R}\, g(\rho, R) \beta V^{eff}_{model}(R, \alpha_{gl}; \beta\gamma, L_e) \\ &+ \{\frac{3}{2} \ln\left(\frac{\alpha_{gl}\Lambda^2}{\pi}\right) - 3 \ln\left[erf(\sqrt{\alpha_{gl}} D)\right]\} - \delta f. \end{aligned} \tag{2.8}$$

Here the first integral gives the "on-site" free energy after double averaging over thermal fluctuations and over topological disorder. The second term (inside the curly bracket) comes from $-(1/N) \ln\left[Z_p \cdot \left(\int_{|w_i| \le D} d\vec{w} e^{-\alpha w^2}\right)^N\right]$ which accounts for the effect of cell constraint; Z_p represents the momentum part of the partition function, and we choose a cubic cell with side length $D \equiv \rho^{-1/3}/2$ for convenience. Finally, δf (taken to be 0.224) is a numerical correction to the entropy of HS crystal system near face-centered-cubic (fcc) close packing obtained via SCP approximation, which then gives extremely accurate free energies near melting.

The pressure can be evaluated by numerically differentiating the liquid free energy:

$$p = \rho^2 \left(\frac{\partial}{\partial \rho} f_{liq}\right)_{T,N} k_B T. \tag{2.9}$$

Random first order transition theory identifies the configurational entropy with the difference between the free energy of the highly localized glass solution and the liquid, i.e.

$$\frac{S_c(\rho, \beta)}{N k_B} = \Delta f = f_{gl} - f_{liq} \tag{2.10}$$

Another interesting quantity that can be evaluated within the SCP theory is the number of force-bearing bonds, i.e., those that have a length exceeding the elasticity onset L_e. In three dimensions, the structure-dependent probability for a single bond to be elastically stretched (or equivalently, the fraction of stretched bonds, in the mean field context) is given by

$$q_3(\alpha, R) = \int_{|\vec{r}| > L_e} d\vec{r} \left(\frac{\alpha}{\pi}\right)^{3/2} e^{-\alpha(\vec{r} - \vec{R})^2}, \tag{2.11}$$

or

$$q_3(\alpha, R) = \sqrt{\frac{\alpha}{\pi}} \frac{1}{R} \int_{L_e}^{\infty} dr\, r \left[e^{-\alpha(r-R)^2} - e^{-\alpha(r+R)^2} \right]. \tag{2.12}$$

The number of stretched bonds can then be obtained by averaging over non-vibrational disorders, i.e. configurational degrees of freedom:

$$q_3(\alpha, \rho) = \rho \int_{1st\ shell} d\vec{R}\, g(\rho, R) q_3(\alpha, R). \tag{2.13}$$

This double integral accounts both for the contributions from the fluctuation of individual bonds (small α indicates strong fluctuation) and from fluctuations in the underlying topological structure (short L_e enlarges the radial range that contains stretched "fiducial bonds").

2.3 Numerical investigations

2.3.1 Localization strength

The fundamental quantity that characterizes the diverse mechanical phases in our model is the localization strength, or the force constant of the emergent Einstein oscillator, α. We may plot α against bead density ρ and/or effective stiffness $\beta\gamma$ of the F-actin. We measure lengths and energies in units of d and β, then the corresponding dimensionless quantities are taken to be $\rho^* \equiv \rho d^3 = \rho$ and $\gamma^* \equiv \beta\gamma d^2 = \beta\gamma$. We start with several representative one dimensional plots that come from vertical slices of the two dimensional α-surface, and we first focus on the liquid-like solution which is absent in the pure HS system.

Referring to Fig. 2.2(a), we observe that the first shell (R^*) of the radial distribution shrinks from 1.95 to 1.3 as the bead density increases from 0.2 to 1.2. When $L_e < R^*$, the separation $(R^* - L_e)$ determines how many nearest-neighbor fiducial sites are found beyond L_e and on-average have tense bonds; in this case, both the underlying topology and thermal fluctuations contribute to the localization. On the other hand, however, if $L_e > R^*$, all fiducial sites of nearest neighbors fall inside the sphere of radius L_e and on-average result in buckled strings; in this case fluctuations are the only source of stretching and thus of localization. This

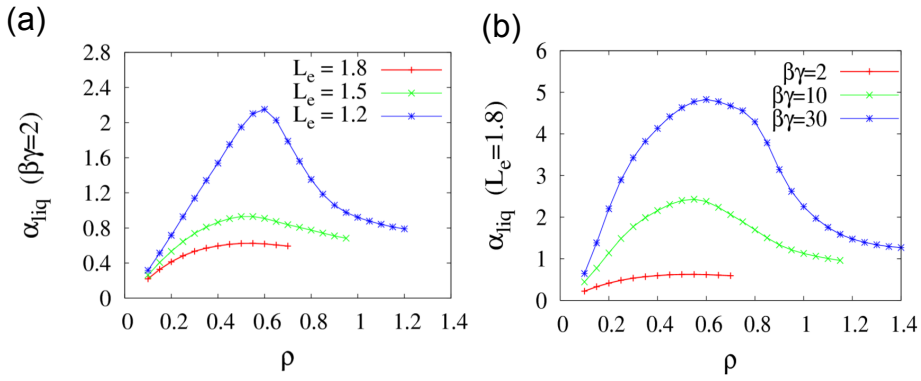

Figure 2.3: Liquidlike localization strength α_{liq} versus bead density ρ. (a) For $\gamma^* = 2$ with $L_e = 1.2$ $(blue), 1.5$ $(green), 1.8$ (red); (b) for $L_e = 1.8$ with $\gamma^* = 2$ $(red), 10$ $(green), 30$ $(blue)$.

information is also encoded in the *threshold density* ρ_{th} beyond which a stable α_{liq} solution no longer exists. In sum, longer onset length leads to weaker overall localization as well as lower threshold density, as shown in Fig. 2.3(a). A similar effect is produced by low rigidity γ as can be seen in Fig. 2.3(b); since smaller γ indicates a broader and shallower confining well in which particles are more loosely tethered thus being less localized, and the corresponding liquid-like solution becomes unstable at lower ρ_{th}.

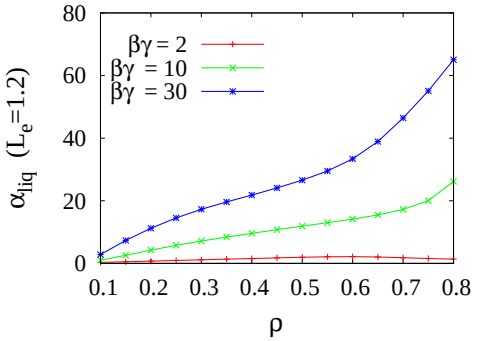

Figure 2.4: Liquidlike localization strength versus bead density for $L_e = 1.2$ with $\beta\gamma = 2, 10, 30$. Liquid-like solution is still distinct at $\beta\gamma = 2$, whereas a rapid crossover to glassy behavior occurs for $\beta\gamma = 10, 30$.

The compromise between the number of contributing neighbors and the degree of stretching produces a non-monotonic density dependence of α_{liq} at a

given L_e, and the most efficient localization is achieved at an intermediate density around 0.6. At $\rho < 0.6$, the individual bonds become less likely to be stretched as the beads pack more densely, whereas the total number of bonded neighbors increases much faster with increasing density, the combined effect thus leads to a stronger localization as density grows. On the other side when $\rho \geq 0.6$, the number of bonded neighbors almost saturates, while the thinner first shell of g(r) indicates less tightly stretching or deeper buckling as density increases, whereby the localization strength decays accordingly.

Note that this non-monotonic density dependence only occurs for a sufficiently long L_e or in the low-$\beta\gamma$ regime for a short L_e. For sufficiently high $\beta\gamma$ liquid-like solutions are no longer distinct, instead a rapid crossover to high-α solutions is observed, as is exhibited in Fig. 2.4.

2.3.2 Thermodynamics

q_3—role of localization

Recall that q_3 explicitly counts the average number of tensely bonded neighbors. Its dependence on elasticity comes from the self-consistently determined localization strength α and the intrinsic cutoff L_e for a bond to be stretched. For a given ρ, more elastically-bonded neighbors become available as L_e drops (Fig. 2.5(a), bottom to top) and/or γ^* decreases (Fig. 2.5(b), bottom to top). For a moderate γ^*, the number of stretched bonds increases with bead density for various L_e as long as stable liquid-like solution exists (Fig. 2.5(a)); at high γ^*, however, close to the most localized regime for individual beads, even though the coordination number still gently increases, the weak fluctuation (high α) strongly suppresses bond stretching, thus leading to an intermediate decline of q_3 in its ρ-dependence, as seen in $\gamma^* = 10, 30$ cases (Fig. 2.5(b)).

Free energy profile—consistency with SCP theory

As can be seen when we compare Fig. 2.6 with the corresponding curves in Fig. 2.3(b), the minima on the free energy profile $F(\alpha)$ for the liquid-like state

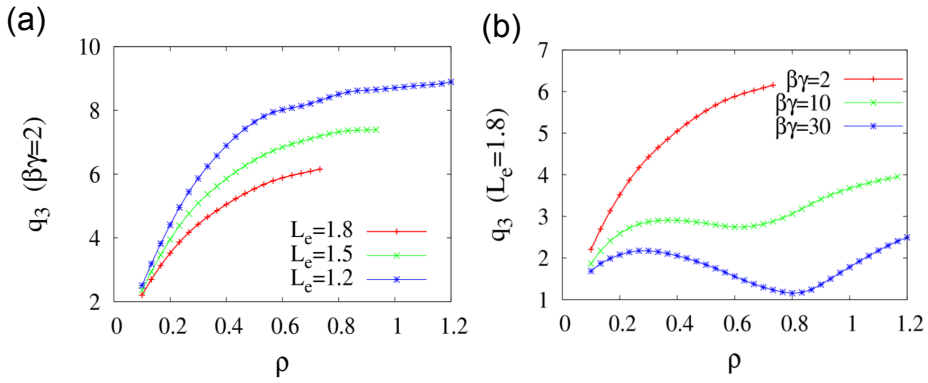

Figure 2.5: Average number of stretched bonds q_3 vs bead density ρ. (a) $\gamma^* = 2$ for $L_e = 1.2, 1.5, 1.8$ (top to bottom); (b) $L_e = 1.8$ for $\gamma^* = 2, 10, 30$ (top to bottom).

coincide with the corresponding α_{liq} solutions obtained via the SCP method. As the bead density increases, the overall profile shifts upward. At a given density ($\rho = 0.6$ here), raising L_e (Fig. 2.7(a)) or lowering γ^* (Fig. 2.7(b)) causes the liquid-like state to be increasingly favorable (deeper and sharper valley) with lower localization strength (bottom of valley being shifted leftward). As expected, γ^* only markedly affects the low-α regime ($\alpha \leq 10$), since when particles are sufficiently localized (due to short L_e or high ρ), bond stiffness only plays a minor role in altering the interaction strength. In contrast, varying L_e not only modulates the low-α regime, but causes a nearly uniform upshift of the high-α portion of $F(\alpha)$; this observation is consistent with our previous statement that when thermal fluctuations are weak (high α) topology dominates; shorter elasticity onset L_e indicates more stretched bonds at a given density and thus enhanced interaction.

Pressure

We plot pressure versus bead density with $\gamma^* = 2$ for a series of onset lengths in Fig. 2.8. At the low-density end, most of the bonds are stretched and the system tends to shrink, resulting in a very low pressure. At the opposite end, in a densely packed system HS repulsion takes over the major role; the steeply increasing pressure reflects the rising difficulty in rearrangement and the consequent

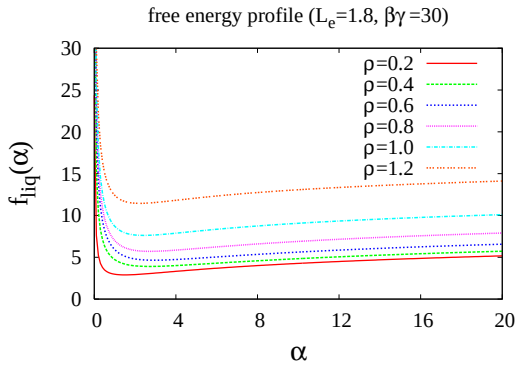

Figure 2.6: Free energy f_{liq} versus the order parameter—localization strength α with $L_e = 1.8, \beta\gamma = 30$ for $\rho = 0.2$–1.2 (bottom to top). As the bead density ρ increases, the overall profile shifts upward with the valley indicating the equilibrium solution α_{liq}.

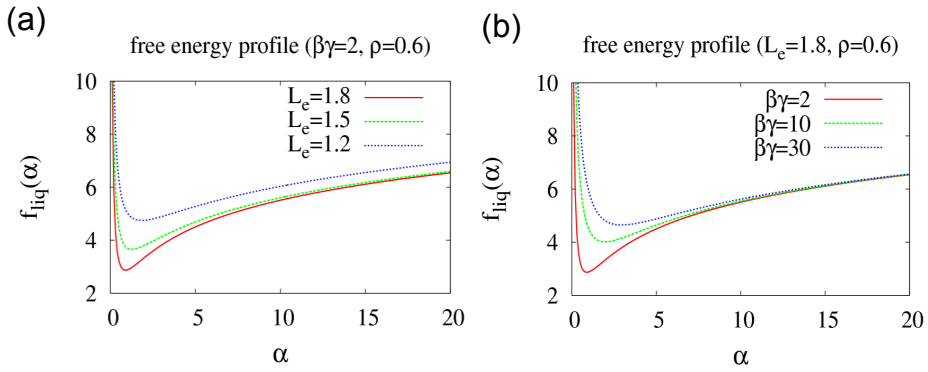

Figure 2.7: Free energy versus localization strength. (a) $\gamma^* = 2$ for $L_e = 1.2, 1.5, 1.8$ (top to bottom); (b) $L_e = 1.8$ for $\gamma^* = 2, 10, 30$ (bottom to top).

soaring resistance to compression. In contrast with the nearly universal behavior at both extremal-ends, parameter-sensitive features emerge in the intermediate density regime, where shorter L_e enhances the effective attraction and thus lowers the pressure of the system. In particular, a non-monotonic behavior is observed to occur for pliable springs (low γ^*) with early onset (short L_e), as is exhibited for the case of $L_e = 1.2$.

It is natural to expect the possibility of a negative pressure at a modest bead concentration in view of the tendency of the network to shrink due to attraction. We plot in the inset of Fig. 2.8 the contribution of attraction (p_{attr}) to the total

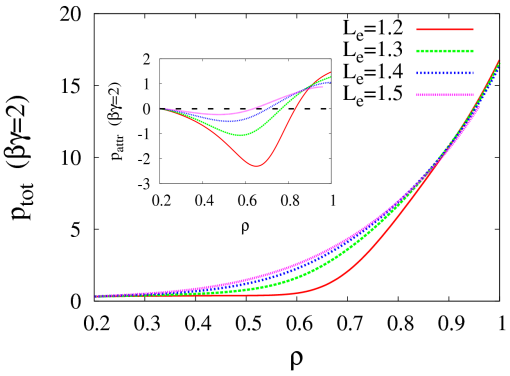

Figure 2.8: Pressure versus bead concentration for soft strings ($\beta\gamma = 2$) with various onset lengths $L_e = 1.2, 1.3, 1.4, 1.5$ (bottom to top). Main plot: total pressure; inset: pressure due to attraction.

pressure (p_{tot}) for several onset lengths, and p_{attr} does indeed exhibit a negative valley at intermediate concentrations. It is clearly seen that a short onset length is necessary for a notable contribution from attraction and thus for the emergence of this non-monotonic behavior of the total pressure.

On the other hand, the negative contribution owing to attraction is eventually overwhelmed by the positive part due to a more rapid increase in repulsion as ρ increases, and the total pressure (p_{tot}) remains positive over the whole density range. This behavior is originated from the specific form of the free energy functional that we have used for the model system, where the correction due to attraction enters as a perturbation to the dominating repulsive part. This result might require modification to better accommodate the low-concentration regime where attraction becomes important. Another reason for this behavior may be related to the $g(r)$ we have used for the radial distribution which drops sharply when move away from the core; bonding effects might lead to a fatter tail of $g(r)$ and an enhanced contribution from attraction. Nevertheless, we feel these insufficiencies of the approximations should not modify the mechanical and thermodynamic properties qualitatively.

The thermodynamic considerations discussed above help with understanding of the physics underlying the predicted phase behavior in terms of the order parameter α. We will discuss these in detail next.

2.3.3 State diagram

Overview

In our model network, we assume permanent bond connections between the nearest-neighbor pairs. The interplay between these intrinsic constraints and the thermal fluctuations gives rise to an inhomogeneous distribution of tensile forces throughout the network. Such force heterogeneity exhibits as a (uniform) non-vanishing tethering strength in our mean field context. This explains the prediction that a completely ergodic fluid phase, which is allowed for the pure hard-sphere system with short-range attraction and that has strictly diffusive behavior for long times i.e. $\alpha \to 0$ as $t \to \infty$, never occurs for the equilibrium network structure; the lack of utter freedom in locomotion leads to a *finite* α over the whole span of bead concentrations.

There exist two characteristic densities in our model system: the threshold density ρ_{th} above which the homogeneous liquid-like solution is no longer stable, and the critical density ρ_{cr} which signals the emergence of a glassy state. These densities help define the boundaries between diverse mechanical phases:

- $\rho < \rho_{th}, \rho_{cr}$: only α_{liq} exists, which describes the liquid-like loosely tethered phase;
- $\rho_{th} < \rho < \rho_{cr}$: the mean-field α_{liq} is no longer stable, and the glassy state has not yet occurred; bifurcation to a low-α solution may occur, exhibiting a symmetry broken phase which we shall call the "martensitic-like" (ML) phase;
- $\rho_{cr} < \rho < \rho_{th}$: both α_{liq} and α_{gl} exist, depicting the transition state with presumably coexisting phases that implies a macroscopic number of configurational degrees of freedom for structural rearrangements.
- $\rho > \rho_{th}, \rho_{cr}$: the repulsive-glass phase dominates.

Features of the various phases

Our SCP calculation has found five distinct phases in our model system: the liquid-like (LL) phase, the crossover (CO) phase, the repulsive-glass (RG) phase, the multiple-solution (MS) phase, and a martensitic-like (ML) phase.

◊ the liquid-like (LL) phase and crossover (CO) phase

We choose two particular onset lengths based on their position with respect to the boundary of the nearest-neighbor shell.

For $L_e = 1.8$, this cutoff stands outside the nearest-neighbor shell for $\rho : 0.2$–1.2, which means that almost all the "fiducial bonds", i.e. bonds that connect fiducial sites of nearest neighbors, are buckled, and become more floppy as bead density grows; in this situation once the coordination number saturates at $\rho \simeq 0.6$, increasingly deeper buckling results in a decrease in α_{liq} as ρ increases. Owing to the overall buckling of the bonds, higher bond stiffness and thus smaller fluctuations lead to a smaller probability for the bonds to tense up, and an even steeper drop in α_{liq} occurs as density increases (Fig. 2.3(b)). Therefore, the distinct liquid-like solutions persist over the whole γ^*-range of interest (as long as $\rho \leq \rho_{th}$) for the case of a long onset length.

For the case of $L_e = 1.2$, however, since this cutoff remains inside the nearest-neighbor shell all the way through $\rho : 0.2$–1.2, there always exists a fraction of fiducial bonds being stretched beyond their relaxed length. In this situation the descending branch of α_{liq} at intermediate densities only occurs for very soft springs, i.e. in the low-γ^* regime. Furthermore, taking advantage of the persistent fraction of stretched (fiducial) bonds, sufficient stiffness beyond a threshold value (marked by the phase boundary ρ_{CO}) would help enhance localization, and facilitates a smooth crossover from elasticity-dependent liquid-like behavior to geometry-dominant glassy behavior (as seen in Fig. 2.4); we shall refer to the states showing such behavior as being in a "crossover" (CO) phase.

◊ the repulsive-glass (RG) phase

Current simulations performed on increasingly longer timescales make it possible to compare the equilibrium properties based on the present theoretical predictions with simulation outcomes in the long-time limit. To investigate the long-term fate of attractive glasses, simulations of glassy arrest in hard-core particles with short-range attraction [32] were performed over a waiting-time-independent window of up to 10^6 MD units, which is a few orders of magnitude longer than those reached by previous experiments or simulations ($\sim 10^3$ MD units). They

found that even if the short-range attraction generates a transient plateau in the time-evolution of the calculated mean-squared displacement (i.e. inverse α) owing to breaking and reforming of nearest-neighbor "bonds", the long-time behavior of "bonded" and "nonbonded" repulsive glasses converges, suggesting that in the long run particles are ultimately confined by their topological cage of neighbors.

Our equilibrium calculation on a long-range-attractive HS system consistently shows that as long as the (nearly-universal) critical density is reached, there would emerge the repulsive-glass behavior being almost independent of the attractive strength γ^*. Such independence is found for various onset lengths.

$\Diamond$ the multiple-solution (MS) phase

The simultaneous presence of distinct α_{liq} and α_{gl} solutions, according to the SCP analysis, implies a non-vanishing configurational entropy in this phase region. This further signifies the availability of configurational degrees of freedom for structural rearrangement. As shown in previous examples, a longer onset length ($L_e = 1.8$) allows for distinct α_{liq} solutions over a larger $\beta\gamma$ range and thus allows the system to explore more energetically favorable configurations; on the other hand, the emergence of crossover behavior at moderate $\beta\gamma$ and the consequent shrinkage of the MS regime induced by early onset of elasticity ($L_e = 1.2$) suggests a rapid loss of configurational entropy as bonds become stiffer.

$\Diamond$ the martensitic-like (ML) phase

As verified by our SCP calculation, a completely ergodic fluid phase, presented by a sticky HS system with weak attraction at a low density, does not occur for an elastically bonded HS system, so that α is always finite. Yet finite localization strength does not ensure a homogeneous structure. In our model system, with a large elasticity onset L_e (compared to the lattice spacing) and a low bond stiffness γ^*, bifurcation in α_{liq} takes place before the emergence of glassy behavior (i.e. below ρ_{cr}) and may allow the existence of a spatial-symmetry-broken phase characterized by a stable pair of liquid-like solutions. The occurrence of bifurcation was also found in an earlier study by Shen and Wolynes with a pure "cat's cradle" built on a regular lattice. The possibility of self-generated spatial heterogeneity associated with such a mechanical instability makes it interesting to study what

kind of structural phase such a destabilized system would actually develop into, and to quantify the associated conformational changes. The resultant mechanical/structural phase might be related to the orientational order often observed in F-actin networks of the cytoskeleton.

We performed explicit molecular dynamics (MD) simulations on a body-centered-cubic (BCC) network of n^3 unit cells with pure nonlinear elasticity, as described by the Hamiltonian $H = \frac{1}{2}\sum_i \sum_{<j>} \frac{1}{2}\gamma \left(|\overrightarrow{r_i} - \overrightarrow{r_j}| - L_e\right)^2 \Theta\left(|\overrightarrow{r_i} - \overrightarrow{r_j}| - L_e\right)$. Here i,j label the nodes and $\langle \cdots \rangle$ represents sum over nearest neighbors; γ denotes bond stiffness and L_e elasticity onset as before. The bipartite nature of the BCC structure allows us to divide the original BCC network into two interpenetrating simple-cubic (SC) subnetworks (see an illustration of the subnetwork division in Fig. 2.9(a)) , so that each node on one subnetwork interacts with its 8 neighbors on the other subnetwork, and the neighbor list never changes.

The quality of the motion—whether it is oscillatory or monotonic—depends on the relative contribution of the inertial forces (that tend to produce oscillations) and the viscous forces (that tend to damp the oscillations out). It turns out that inertial forces are usually very small at the microscopic and molecular levels, so that the overdamped limit usually applies [1]. We thus carried out the simulations with stochastic dynamics in the overdamped limit as described by the Langevin equation $d\vec{r}_i/dt = (1/\Gamma)\vec{f}_i(t) + \vec{\eta}_i(t)$. Here $\vec{f}$ represents the deterministic force due to the nonlinear elastic interaction, and the force exerted by the fluid particles divides into two parts: the average viscous force $-\Gamma\vec{v}$ and a random force $\vec{\zeta}(t) \equiv \Gamma\vec{\eta}(t)$ whose time average is zero. We assume a Gaussian white noise that satisfies $\langle \eta_i(t)\eta_j(t')\rangle = 2D\delta_{ij}\delta(t-t')$. As usual, Γ and D denote the drag coefficient and diffusion constant, respectively. Lengths are expressed in units of L_e. We applied periodic boundary conditions.

We first show the evolution of the mean squared displacement (MSD) with respect to the *initial* equilibrium positions of the nodes. We simulated a system of size 5^3 with soft bonds ($b \equiv \beta\gamma = 1$) at a low temperature ($\beta = 30$). When the elasticity onset L_e is comparable with the initial mesh size, R, of both subnetworks, elastic stretching is immediately felt as soon as thermal buffeting displaces any of

the nodes from their equilibrium locations, and therefore, the whole network just wiggles about the underlying BCC lattice, which defines the unique minimum of the system's energy landscape. As shown in Fig. 2.9(b), in this case the two subnetworks act in a concerted manner with their mean squared displacements fluctuating almost "in phase", suggesting the whole BCC network does not show symmetry breaking.

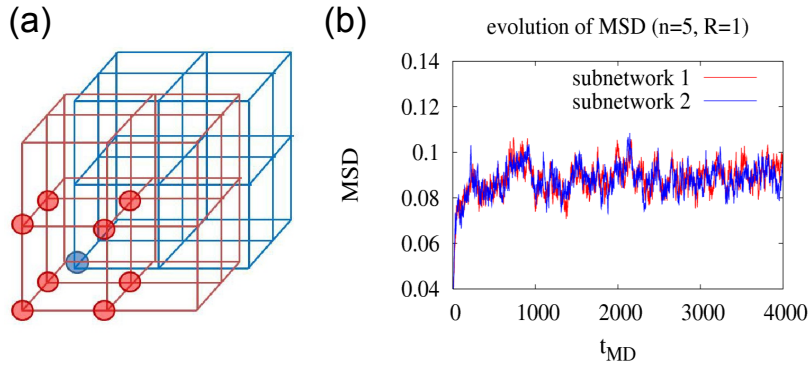

Figure 2.9: (a) An illustration of the subnetwork division. The bipartite nature of the original BCC lattice allows for separation of one SC subnetwork (red) from the other (blue). Each node on one subnetwork (blue sphere) interacts with its 8 neighboring nodes (red spheres) on the other subnetwork. (b) The MSD of both subnetworks ($n = 5$) versus simulation time in MD units for a moderate elasticity onset to mean separation ratio $L_e/R = 1$. $\Gamma = 50, \beta = 30$.

When the system parameters are modified to be in the regime of bifurcation by increasing the L_e/R ratio to 10 (other parameters unchanged), however, the MSD exhibits a much larger average amplitude (after a steady value is reached) and stronger fluctuations around it; furthermore, the two subnetworks fluctuate in a correlated manner but are almost completely out of phase with each other, see Fig. 2.10(a). In this case, the initial network presents no elastic constraints on the nodes, thus the system is free to expand until it reaches a steady size where the mean separation between the bonded neighbors is comparable with the length for elasticity onset; the correlated fluctuations result from alternate distortions between the subnetworks within a system of moderate size as 5^3. As we enlarge the system to $n = 10$ (Fig. 2.10(b)), the steady amplitude of MSD maintains

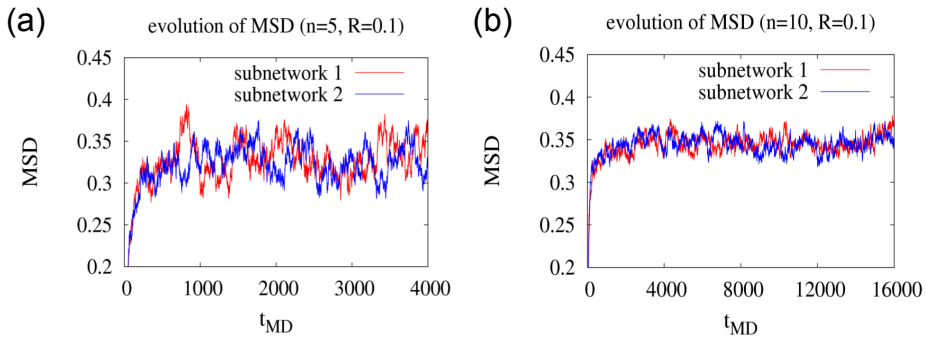

Figure 2.10: Effect of the system size on the behavior of MSD in the regime of bifurcation. Both: $L_e/R = 10, \Gamma = 50, \beta = 30$. (a) $n = 5$; (b) $n = 10$.

($\sqrt{MSD} \sim 0.6$ stretching could occur under thermal driving), yet the fluctuations about the average become much weaker.

The above observation raises the intriguing possibility of a "martensitic-like" phase consisting of (frustrated) domains with (complementary) distortions. To examine further this possibility, we also queried vectorial information about the directions of motion (lost in MSD) by examining the evolution of displacement vectors. We divided the simulation cell evenly along each initial dimension to get 8 domains each with the same number of nodes, and traced the subsequent motion within each domain. We chose a time window $t_{MD} = 4000$–6000 after the steady size was reached, and used the running time averaged position of the nodes as the reference with respect to which the displacements were defined. We present in Fig. 2.11 the bulk-averaged (left column) and domain-averaged (right column) displacement components. The evolution of the displacement vectors in these two cases shows several contrasting features. First, the maximal amplitude of the domain-averaged displacements is about one order of magnitude larger than the maximal amplitude of the bulk-averaged displacements. Second, the bulk-averaged displacements of the two subnetworks are exactly oriented in the opposition directions with essentially the same amplitude, whereas in individual domains two subnetworks move almost in the same direction yet with different amplitudes. These two contrasting features support the picture of localized distortions with

different orientations in different domains. In addition, the peak value of the displacement amplitude occurs at different times for different domains, which suggests "frustration" between the domains.

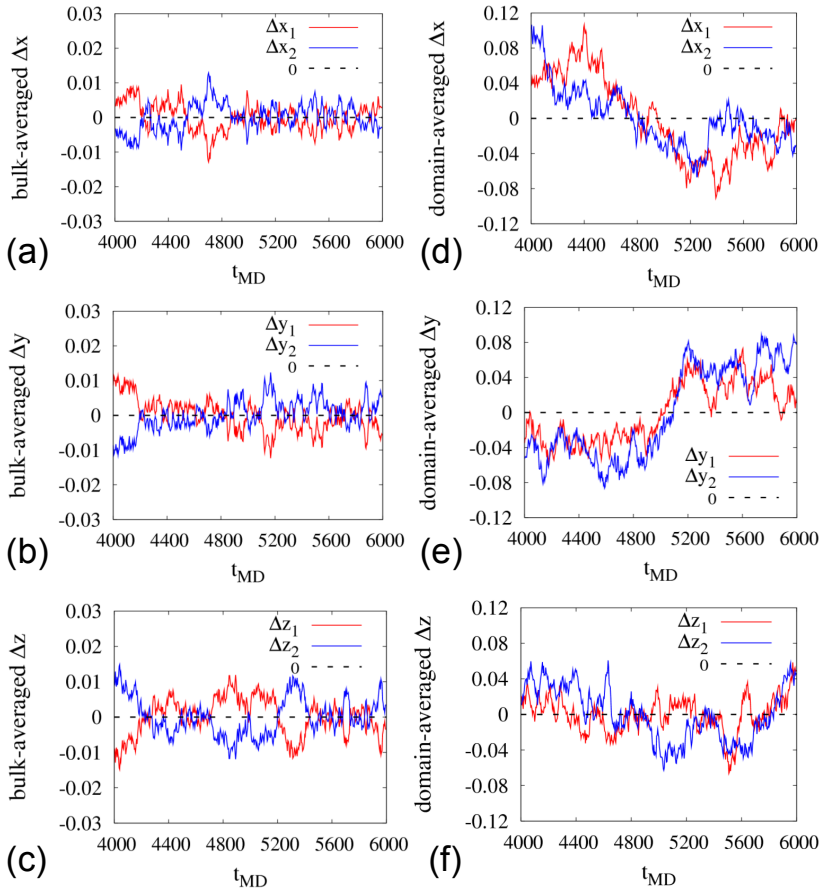

Figure 2.11: The bulk-averaged and domain-averaged displacement components for both subnetworks. $n = 10, L_e/R = 10, \Gamma = 50, \beta = 30$. (a)-(c) average over the whole simulated region; (d)-(f) average over one of the 8 domains. (a)(d) x component; (b)(e) y component; (c)(f) z component.

To roughly estimate the domain size and to quantify the orientational correlation within the domains, we made equal-width shells centered at each node (the diameter of the outermost shell was taken to be equal to the box size of the simulated system), and computed two measures: (1) the average projection of director (i.e. the unit vector of the corresponding displacement) in each shell onto that of the central node, and then averaged over all possible central nodes. In

mathematical terms, we monitor $P_m(t) \equiv (1/N)\sum_{i=1}^{N} \hat{r}_i(t) \cdot \left(\frac{1}{N_m}\sum_{j_m=1}^{N_m} \hat{r}_{j_m}(t)\right)$, where N is the total number of nodes and N_m the number of nodes within the m^{th} shell of the central node; $\hat{r}_i$ and $\hat{r}_{j_m}$ are instantaneous directors of the central and in-shell nodes, respectively; (2) the average tensor product of directors constructed as $Q_m(t) \equiv (1/N)\sum_{i=1}^{N} (\hat{r}_i(t) \cdot \hat{y}) \left(\frac{1}{N_m}\sum_{j_m=1}^{N_m} (\hat{y} \cdot \hat{r}_{j_m}(t))\right)$, where $\hat{y}$ is the unit vector pointing from the instantaneous position of node i to that of node j_m. This measure thus reflects the degree of alignment of two directors along the line connecting their positions.

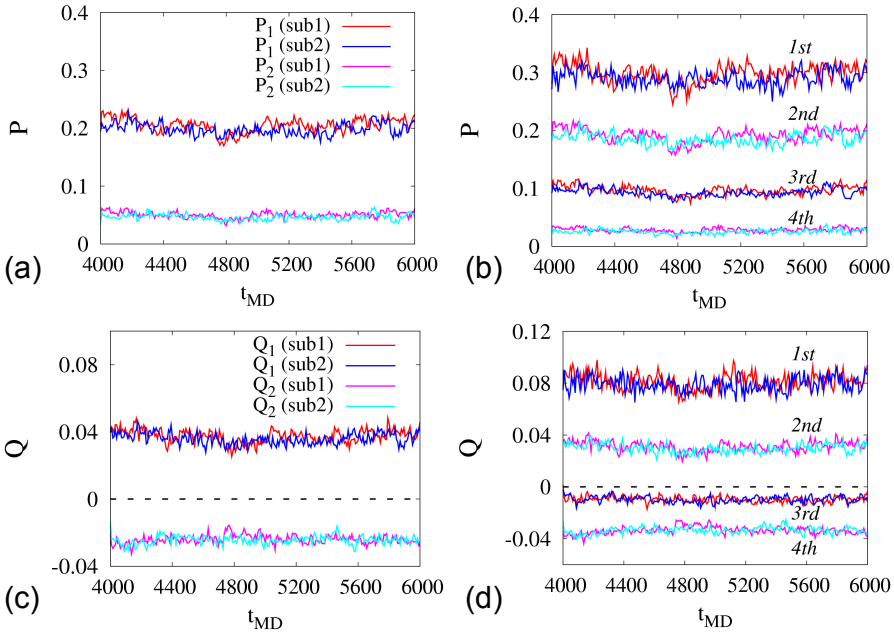

Figure 2.12: The evolution of two measures of the orientational correlation for both subnetworks. $n = 10, L_e/R = 10, \Gamma = 50, \beta = 30$. (upper) the average director projection P for 2 shells (a) and 4 shells (b); (lower) the average tensor product of directors Q for 2 shells (c) and 4 shells (d). In each panel, shown from top to bottom are values of the measure from the inner to the outer shell(s); red/magenta denotes subnetwork 1, and blue/cyan denotes subnetwork 2.

We show in Fig. 2.12 the evolution of these two measures for the cases of 2 shells (left column) and 4 shells (right column). The average director projection P, in each shell, fluctuates about a steady value, which decays from around 0.2 to 0.05 as we go from the inner to the outer shell in the case of 2 shells (panel (a)).

This spatial decay in average P indicates that the domain size is roughly half of the box size, i.e., 5 times the initial lattice spacing. As expected, the fluctuations in P become weaker for outer shells due to the larger number of nodes to be averaged over; this trend is clearly exhibited in the case of 4 shells (panel (b)).

In contrast to the positive steady value of P in all shells, the average tensor product of directors Q becomes negative for the outer shell(s) (lower panels of Fig. 2.12). Since Q encodes the angular location of the in-shell node relative to the central node, a negative value of Q implies the two directors point in the opposite directions along the line that connects them. A stronger opposite alignment would give a more negative Q value. Q thus serves as an indicator of the loss in orientational correlation. Also, negative Qs are smaller in amplitude than positive Qs.

To make the situation more apparent, we visualized the ensemble-averaged displacement vectors at different angles and different distances from the central node for the case of 2 shells (Fig. 2.13). We took the ensemble-averaged direction of motion of the central node as reference. Within the first shell (colored in pink) the average displacement in any angular range gives a positive projection on the reference direction, in other words, the displacement field is anisotropic and the movements occur mainly along the same direction as that of the central node. The aligned movement is most significant near the "equator". The displacement vectors in the second shell (colored in blue), however, no longer exhibit a preferred orientation, instead they reorient considerably. Close to the "south pole", the outward movements are almost perpendicular to the reference direction, whereas small inward movements occur near the "north pole". The spatial decay in orientational correlation is thus apparently observable and consistent with the features exhibited by our correlation measures.

In sum, in addition to the multiple solution regime which may be related to the saddle point solution pictured as ergodic droplets formed against a glassy background in a finite-range system, our mean-field level calculation also predicts a parameter regime where nonlinear-elasticity-induced spatial inhomogeneity is exhibited through a "martensitic-like" phase with local oriented distortions.

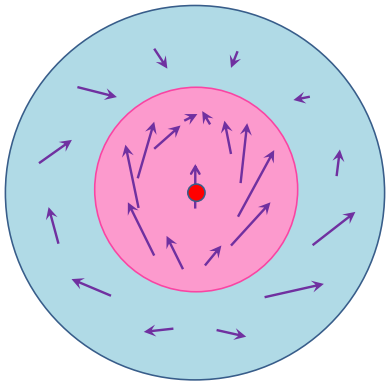

Figure 2.13: Average displacement vectors (purple arrows) at different angles and different distances (inner and outer shells) from the central node (red sphere). Shown for one cross section of the spherical region.

Typical examples

We plot the 2D surfaces of α_{liq} and α_{gl} against $\rho^*(=\rho)$ and $\gamma^*(=\beta\gamma)$ at a given L_e to examine how these physical parameters modulate the phase boundaries. The contour maps are also projected on the bottom as reference for the upcoming state diagrams. We choose two particular values of the elasticity onset L_e that characterize typical tense networks ($L_e = 1.2$) and floppy networks ($L_e = 1.8$).

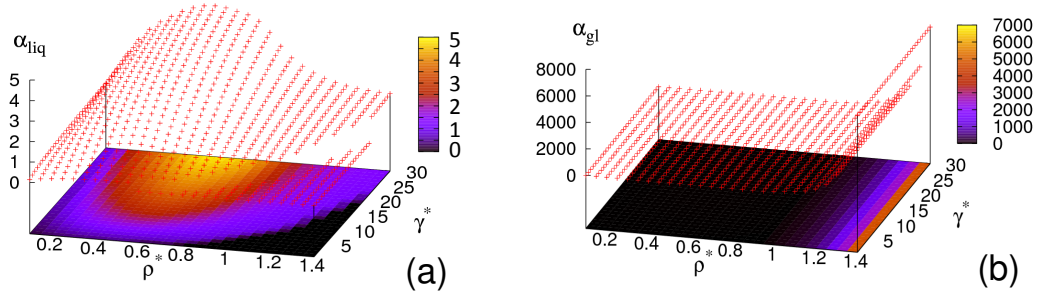

Figure 2.14: 2D surface of localization strength over the parameter space extended by bead density (ρ^*) and elastic stiffness (γ^*) in the case of $L_e = 1.8$ characterized by mostly floppy bonds. Here ρ^* runs through 0.1 to 1.4 and γ^* ranges from 1 to 30. We show the α surface and its contour map for liquid-like (a) and glassy (b) solutions. The color scheme indicates the relative measure of the α values; the highest value within a given range is colored as bright yellow and the lowest as black.

We start with $L_e = 1.8$ case. For this relatively long onset length, liquid-like and glassy solutions are quite distinct over the whole parameter space. As can be seen from Fig. 2.14(a), the liquid-like localization strength takes on a "hump" shape along the ρ-axis peaking around $\rho = 0.6$, and elevates smoothly in the γ^* direction. However, the stable α_{liq} solution terminates at a sharp boundary defined by $\rho_{th}(\gamma^*, L_e)$ beyond which the mean field α_{liq} solution becomes destabilized. This instability region, located in the high-ρ low-γ^* corner, presents a quasi-triangular shape which indicates the increased need of stiffer bonds to stabilize the loosely arrested state as density increases. The ML phase may arise as a possible consequence of this (elastic-)nonlinearity-induced mechanical instability. On the other hand, α_{gl} emerges at $\rho_{cr} \simeq 1$. The values of the critical density and of α_{gl} are nearly independent of γ^*, as shown in Fig. 2.14(b); such stiffness-independence arises from takeover of the dominant role by HS repulsion in reconfiguring a densely packed system.

The corresponding state diagram on ρ-γ^* plane is displayed in Fig. 2.15(a). The trajectories marked by ρ_{th} (blue curve) and ρ_{cr} (dashed line) unambiguously divide the state space into four distinct phase regions: distinct liquid-like ($\rho < \rho_{th}, \rho_{cr}$) and glassy ($\rho > \rho_{th}, \rho_{cr}$) phases locate at the opposite corners diagonally, while the rest of the space naturally divides into the ML and the MS phases depending on whether $\gamma^* < \gamma_c^*$ ($\rho_{th} < \rho_{cr}$) or $\gamma^* > \gamma_c^*$ ($\rho_{th} > \rho_{cr}$), respectively. For a given L_e, ρ_{th} increases with γ^* whereas ρ_{cr} is topologically determined, consequently when $\gamma^* < \gamma_c^*$ and $\rho_{th} < \rho < \rho_{cr}$, the region of the ML phase narrows down as γ^* increases due to decreasing $(\rho_{cr} - \rho_{th})$ until it disappears at $\gamma^* = \gamma_c^*$ ($\rho_{th} = \rho_{cr}$); when $\gamma^* > \gamma_c^*$ and $\rho_{cr} < \rho < \rho_{th}$, the MS phase takes over and broadens as γ^* rises because of growing $(\rho_{th} - \rho_{cr})$.

In addition to the four types of phases exhibited by the floppy network ($L_e = 1.8$), the state diagram for the tense network ($L_e = 1.2$) presents a novel phase boundary separating out a large region featuring a crossover behavior. When we compare the 2D surface for α_{liq} with that for α_{gl} over the whole parameter plane, we find that they almost coincide except for a stripe-shaped region in the low-γ^* high-ρ^* corner. When we zoom in on this region (contour map shown in

Fig. 2.16(d)) that peels off the smoothly ascending α-surface (see upper panels of Fig. 2.16), we observe that the diagram appears like a "squeezed version" of that for the $L_e = 1.8$ case; namely, α_{liq} also exhibits a non-monotonic density dependence, and ρ_{th} locates the stability limit of such mean-field solution at each γ^*. As for the glassy state, however, α_{gl} proceeds with its γ^*-independent behavior as soon as the density exceeds $\rho_{cr} \simeq 1$ (see Fig. 2.16(c)). Therefore, similar to what was seen for the case of $L_e = 1.8$, this stripe-shaped region presents LL, MS and RG phases. Noteworthy is that short L_e dramatically reduces the region corresponding to the MS phase, indicating a rapid loss of the configurational degrees of freedom (upon bond stiffness increase). Moreover, the ML phase doesn't emerge for tense networks since the instability is avoided by early elasticity onset.

Beyond the upper boundary of this stripe-shaped phase region, the α-surface gently mounts up toward the high-γ^* high-ρ^* direction and smoothly crossovers from the elasticity sensitive behavior to the glass-like behavior as ρ_{cr} is approached; consequently, in this crossover regime ρ_{cr} no longer marks a clear transition boundary. The resultant state diagram is presented in Fig. 2.15(b).

Characteristic densities

Due to the bonding constraints inherent in a network structure, the stabilized state in our model always possesses a finite localization strength, i.e. $\alpha > 0$. Thus in this case the dynamical transition density ρ_{cr} (or called ρ_A as in literature), rather than being the lowest density to give a non-zero α as occurred in pure or sticky HS systems, is defined as the lowest density to trigger persistent high-α solutions over the whole γ^* range of interest. In our model system, ρ_{cr} signals the emergence of an extensive number of glassy metastable states, yet does not mark the termination of bonding effect.

While the SCP theory alone allows us to find ρ_A, the "Kauzmann density", ρ_K, at which the Helmholtz free energies of the liquid-like and glassy phases match and the configurational entropy ceases to be extensive also relies on the specific form of the free energy functionals we use for these two types of states. The ratio ρ_A/ρ_K dimensionlessly characterizes the thermodynamic aspects. To connect

to the kinetic laboratory glass transition, we note the laboratory transition is defined to occur when the viscosity reaches 10^4 Poise. Random first order transition (RFOT) theory predicts this to be when the configurational entropy is about $1.0\,k_B$ per particle. To translate our thermodynamic results to the laboratory transition density, we will therefore mean by ρ_G the density where the liquid and glass free energies differ by $1.0\,k_BT$ per particle. Despite the universality of configurational entropy at laboratory transition experimentally confirmed in a wide variety of molecular glasses, this universality must be examined further to see if it is valid in the cytoskeletal system which is an active biological material. Here we just use this fiducial entropy to discuss the qualitative features of our model system.

Possible transitions

Visual inspection shows that the phase partition in the upper portion ($\gamma^* > \gamma_c^*$) of $L_e = 1.8$ state diagram exhibits qualitatively identical behavior to that found near the bottom of the stripe-shaped phase region in the diagram of $L_e = 1.2$ case, again indicating that high γ^* and short L_e are comparably competent for making effectively more tense bonds. In this regime, melting from RG via MS region to LL state is expected as ρ is lowered passing ρ_{th} and ρ_{cr} in succession. As for the lower section ($\gamma^* < \gamma_c^*$) of $L_e = 1.8$ diagram, upon increasing density, original homogeneous LL phase becomes destabilized and develops into the proposed ML phase where spatial heterogeneity develops, until finally the RG phase takes the lead. At the crossing point, i.e. $\gamma^* = \gamma_c^*$, RG melts into LL state without going via any intermediate phase. In the case of $L_e = 1.2$, as we go across the phase boundary ρ_{CO} by increasing density, the CO state would transform into the MS phase whereby the distinction between the two types of arrested states with different mechanisms of localization is recovered.

The effective bond stiffness can be varied by manipulating the crosslinking and/or bundling properties or by changing the temperature. Some general features can be extracted from the presented state diagrams, that is high elastic stiffness tends to (1) stabilize the LL state and (2) facilitate the crossover to glassy behavior. The first effect is quite explicit in $L_e = 1.8$ case: as γ^* increases, the elastic-

nonlinearity-induced ML phase evolves into LL state with a single stable α_{liq} when $\rho < \rho_{cr}$, whereas purely RG state develops into the MS state when $\rho > \rho_{cr}$. The second effect is clear in $L_e = 1.2$ case; starting either from distinct LL state or from the MS phase, the system would end up with CO behavior as long as γ^* transcends the phase boundary $\gamma^*_{CO}(\rho)$ (inversion of $\rho_{CO}(\gamma^*)$).

Actually the parameter-modulated transformation of the phase behavior in terms of the order parameter α can be directly detected in α_{tagged} versus $\alpha_{neighbor}$ plots, which explicitly show the emergence and disappearance of, as well as transitions among, various fixed points under the parameter control. In other words, the phase boundaries essentially indicate switching between different fixed point structures of the self-consistent equations. For example, the ρ_{CO} boundary marks the disappearance of the lowest-α fixed point: in LL$\rightarrow$CO case, modest discontinuity in α value arises from stability shift to a newly established fixed point in proximity; while a considerable jump in α value is observed in MS$\rightarrow$CO case, since no intermediate fixed point develops, the high-α fixed point becomes the only stable attractor. Across the $\gamma^*_{th}(\rho)$ (inversion of $\rho_{th}(\gamma^*)$) boundary from below, the initially bifurcation-generating unstable fixed point becomes stabilized by enhanced stiffness.

In addition to the information obtained from the mechanical stability, the integrated thermodynamic characteristics are more informative of the glassy aspects. In the direction of vitrification, kinetic laboratory glass transition is expected at ρ_G in view of the landscape-dominated transport mechanism triggered at ρ_A and the presence of extensively many possible frozen-in states [33, 34, 35]. Whereas the Kauzmann density ρ_K, at which the configurational entropy ceases to be extensive and the glassy configurations are no longer metastable, indicates a thermodynamic transition that ultimately may underlie the kinetic arrest. Though hard to achieve on practical timescale, ρ_K does provide a mean-field estimate of how dense the liquid can be below which a glass transition would be forced to intervene to avoid the entropy crisis [36].

Bonded-fraction dependence of mechanical and thermodynamical properties

So far, we have implicitly assumed that all the nearest-neighbor pairs are bonded, i.e. the network is fully connected and there are no free beads at all. In biological fact, however, apart from the fibrous cytoskeletal network, there also exists a colloidal suspension of protein molecules (including detached ABPs, recycled actin monomers, etc.) that contributes equally, if not more, to the crowding interior of a cell, and thus to the excluded volume effect. We mimic such a suspension of molecules simply as a collection of free beads, in which is immersed the nonlinear elastic fiber network which is anchored on the bonded beads. In our mean-field context, the fraction of bonded beads against the free ones is equivalent to the probability for a nearest-neighbor pair to be bonded. We assign an independent parameter $P_b \in (0, 1]$ to indicate this bonded fraction or network connectivity, and assume P_b to be independent of the overall bead density and the effective bond stiffness to purify its influence.

The self-consistent equation to determine α and the expressions of f_{liq} and f_{gl} are modified accordingly:

$$\begin{aligned} \alpha &= \frac{\rho}{6}\int_{1st\,shell} d^3\vec{R}\, g(\rho, R)\left\{ P_b\, Tr\Big[\nabla\nabla\beta V^{eff}_{model}(R, \alpha; \beta\gamma, L_e)\Big]\right. \\ &+ \left.(1 - P_b)\, Tr\Big[\nabla\nabla\beta V^{eff}_{HS}(R, \alpha)\Big]\right\}, \end{aligned} \tag{2.14}$$

$$\begin{aligned} f_{liq} &= P_b\left[\frac{3}{2}\ln\left(\frac{\alpha_{liq}\Lambda^2}{\pi e}\right) - 1\right] + (1 - P_b)\,\left(\ln\rho\Lambda^3 - 1\right) + \int_0^{\eta}\left(Z_{CS}(\eta') - 1\right)\frac{d\eta'}{\eta'} \\ &+ P_b\,\rho\int_{1st\,shell} d^3\vec{R}\, g(\eta, R)\left[\beta V^{eff}_{model}(R, \alpha_{liq}; \beta\gamma, L_e) - \beta V^{eff}_{HS}(R, \alpha_{liq})\right], \end{aligned} \tag{2.15}$$

$$
\begin{aligned}
f_{gl} &= P_b\,\rho \int_{1st\ shell} d^3\vec{R}\, g(\rho,R)\beta V^{eff}_{model}(R,\alpha_{gl};\beta\gamma,L_e) \\
&+ (1-P_b)\,\rho \int_{1st\ shell} d^3\vec{R}\, g(\rho,R)\beta V^{eff}_{HS}(R,\alpha_{gl}) \\
&+ \left\{ \frac{3}{2}\ln\left(\frac{\alpha_{gl}\Lambda^2}{\pi}\right) - 3\ln\left[erf(\sqrt{\alpha_{gl}}D)\right] \right\} - \delta f. \qquad (2.16)
\end{aligned}
$$

In equations for α and f_{gl}, P_b and $(1-P_b)$ lead the effective potential between bonded and non-bonded pairs, respectively; and the influence due to bonded fraction change on the cell constraint term (i.e. the second order term in the effective potential expansion) is contained in the self-consistently determined α_{gl}. As for f_{liq}, the bonded fraction not only modifies the bonding correction to the HS interaction, it also separates the bonded from non-bonded contributions to the entropy cost: for free particles $\ln\rho\Lambda^3 - 1$ should suffice to describe the density dependence of the entropy cost, whereas we use $\frac{3}{2}\ln(\alpha_{liq}\Lambda^2/\pi e) - 1$ for the bonded beads. Notice the fact that as bonds melt (i.e. P_b decreases), increasing translational symmetry would lower the entropy cost to localize the density waves. We shall show that the logarithmic dependence on α_{liq} used here could at least qualitatively incorporate this feature. Moreover, the bonding entropy due to various choices of bonded pairs among nearest neighbors is not explicitly included, since only the difference between f_{gl} and f_{liq} matters for current purposes. It is easily seen that as $P_b \to 1$ our earlier expressions for a fully connected network (Eqs. (2.5)(2.7)(2.8)) are recovered.

We show in Fig. 2.17 and Fig. 2.18 the state diagrams at $P_b = 0.8$ and $P_b = 0.5$ for both typical networks. The corresponding contour maps of α_{liq} and α_{gl} solutions (not shown here) indicate that the behavior of the liquid-like localization strength is not qualitatively affected by changing the bonded fraction, and the glassy solutions are almost quantitatively intact. Yet the transition boundaries are significantly shifted as the bonded fraction varies. For the floppy network (Fig. 2.17), as P_b decreases, the slower increase of ρ_{th} with γ^* (which implies a lower destabilization density for the liquid-like solution) yields a shrinking MS region and enlarged RG and possibly ML regions. This behavior can be understood

as arising from the fact that weaker network connectivity makes the stabilization via "bond trapping" less efficient. In the tense network (Fig. 2.18), as the bonded fraction drops, both ρ_{th} and ρ_{CO} boundaries shift upward resulting in an extension of both MS and RG regions into a higher γ^* regime. This observation implies a higher bond stiffness is needed to stabilize the liquid-like solutions so as to trigger the crossover to glassy behavior. As for the dynamical transition density ρ_A (i.e. the critical density ρ_{cr} analyzed in earlier sections), it modestly increases with lowering P_b in the tense network (rises from 0.91 to 0.97 as P_b drops from 1.0 to 0.5) while it remains constant (~ 1) in the floppy network; concomitantly α_A halves its value ($115 \to 55$) in the tense network while it stays the same (~ 50) for the floppy case.

We next examine the variation in thermodynamics due to the change of bonded fraction. In both networks, ρ_G and ρ_K are found to persist upon decrease in P_b (with the order of $\rho_A < \rho_G < \rho_K$ maintained). In the tense network, ρ_G and ρ_K develop moderate γ^* dependence and shift toward lower density as P_b decreases, as shown in Fig. 2.18. In the floppy network, ρ_G and ρ_K emerge at considerably higher γ^* as P_b drops indicating greater difficulty in stabilizing LL motion, yet become insensitive to $\beta\gamma$-value thereafter, as seen in Fig. 2.17(a). When P_b is further lowered to 0.5 (i.e. network being half-connected) transition densities are absent due to the limited range of $\beta\gamma$ shown here (see Fig. 2.17(b)) and would reappear if we extend $\beta\gamma$ sufficiently.

In contrast, if we use $\ln \rho\Lambda^3 - 1$ for both the bonded and non-bonded contributions to the entropy cost, a dramatic change in ρ_G and ρ_K is found (not shown here): when $P_b = 0.8$, in both networks, ρ_K is barely above ρ_A while ρ_G is entirely skipped; if P_b is further lowered to 0.5, then $f_{liq} > f_{gl}$ for all $\rho \geq \rho_A$ in MS region, indicating a negative configurational entropy which is not physically meaningful. Actually in our model the highly-localized glassy motion is insensitive to the degree of network connectivity since $\left\langle \beta V^{eff}_{model}(\alpha_{gl}; \rho > \rho_A; \gamma^*, L_e) \right\rangle \simeq \left\langle \beta V^{eff}_{HS}(\alpha_{gl}; \rho > \rho_A) \right\rangle$ and $\left\langle \nabla^2 \beta V^{eff}_{model}(\alpha_{gl}; \rho > \rho_A; \gamma^*, L_e) \right\rangle \simeq \left\langle \nabla^2 \beta V^{eff}_{HS}(\alpha_{gl}; \rho > \rho_A) \right\rangle$, thus such a significant drop in transition densities results from an enhanced attractive interaction in the liquid-like phase due to stronger thermal fluctuations (smaller α_{liq}) induced

by reduced bond constraints (lower P_b). This energetic enhancement in f_{liq} is balanced, partly, by the decrease in entropic cost (to localize density wave) when $\frac{3}{2}\ln(\alpha_{liq}\Lambda^2/\pi e) - 1$ is used, thereby mitigating the bonded-fraction modulation upon the transition densities, and resulting in a persistent transition possibility over a large P_b range.

In sum, the overall tendencies are clear: decreases in the bonded fraction lower the transition densities ρ_G and ρ_K implying that the system becomes less capable of reconfiguring (or easier to become glassy) upon weakening of the network connectivity; in this sense, the model nonlinear-elastic-bonded interaction encourages liquid-like motion and thereby facilitates more efficient structural rearrangements.

2.4 Conclusions

In this paper, we have modeled the cytoskeleton as an amorphous network of rigidly cross-linked nonlinear-elastic bonds that become tense beyond an intrinsic onset length and buckle otherwise. We study the equilibrium mechanical properties of the model system within the framework established by the self-consistent phonon theory and the free energy functional formulation.

We have obtained an initial understanding of the physical behavior via the calculation of several representative thermodynamic quantities, and by examining the state diagram of typical systems. Diverse mechanical properties of a generic cytoskeleton can be recognized by analyzing the featured phases and possible transitions: the permanent network structure excludes a completely ergodic fluid phase, whereas the nonlinearity in the elastic interaction induces spatial heterogeneity that exhibits through a "martensitic-like" phase with domains of oriented distortions. The probable coexistence of the liquid-like and glassy behavior implies the capability of making structural rearrangements with varying agility in response to mechanical stimuli. The effective bond stiffness tends to stabilize the liquid-like state and facilitates its crossover to glassy behavior, whereas the relative position of the elasticity onset with respect to the nearest-neighbor shell dramati-

cally modulates the transition boundaries; the critical density may no longer mark a sharp transition in certain situations when crossover takes place. In sum, the elasticity onset length determines all possible mechanical phases within a practical parameter range, while the bond stiffness decides which transitions occur upon the variation of cross-link concentration (thus of the bead density).

We further investigated how the bonded fraction or network connectivity modulates the phase boundaries as well as the thermodynamic terms of the transition densities (ρ_G and ρ_K). We found that decreasing the bonded fraction results in an upward shift of both ρ_{th} and ρ_{CO} boundaries, indicating the need for a higher bond stiffness to compensate for any loss in connectivity, so as to stabilize the liquid-like motion and to trigger its crossover to glassy behavior; on the other hand, the expanded multiple-solution phase region allows for a large stiffness range with extensive configurational degrees of freedom. As for the thermodynamics, the characteristic densities show little dependence on bond stiffness in floppy networks; for tense networks, however, ρ_G and ρ_K become lower upon enhanced bond stiffness, suggesting decreasing configurational degrees of freedom at a certain density as bonds stiffen. Further, for a given density, possible glass transition takes place at a much lower stiffness in tense networks than in floppy ones, while for a certain bond stiffness, the model system becomes vitrified at a lower bead density as more bonds tense up.

As exhibited clearly in the tense network, the logarithmic dependence of the entropy cost (for bonded interaction in the liquid-like phase) on particle localization strength adopted in our free energy functional contains the feature that as more bonds form, the kinetic glass transition would occur at a higher density, suggesting that the nonlinear-elastic-bonded interaction might help resolve local/steric constraints and facilitate escape from topological trapping, resulting in a more dense packing when stuck finally. Fleshing out this conjecture may require coming to term with finite range consideration; we need to go beyond mean-field level and consider activated events among various metastable states (probably via "droplet relaxation" in a mosaic structure [37]). In a biological sense, cells may prefer an interconnected structural skeleton, not only to maintain their architecture, but to

realize more efficient structural rearrangements when necessary. As argued by Ingber, the tensed/prestressed hierarchical networks play a central role in producing a well-orchestrated multiscale mechanical response [38].

This work provides a general scheme to study macroscopic mechanical phases in terms of the stability to local mechanical environment, and our current equilibrium model sets up a test field for further incorporated features for a more realistic model, in particular, the motorization effect that makes the system active, far from equilibrium and makes it physically distinct from an ordinary polymer network. It will be interesting to study the interplay of bond constraints and force-environment-sensitive motors in maintaining the cell's architecture and modulating the transition behavior. We also plan to investigate the effect of spatial heterogeneity and visualize the structural rearrangements by combining analytic schemes with simulation techniques.

Chapter 2, in full, is a reprint of the material as it appears in the Journal of Chemical Physics **134** 014510 (2011), S. Wang, T. Shen, and P. G. Wolynes. The dissertation/thesis author was the primary investigator and author of this paper.

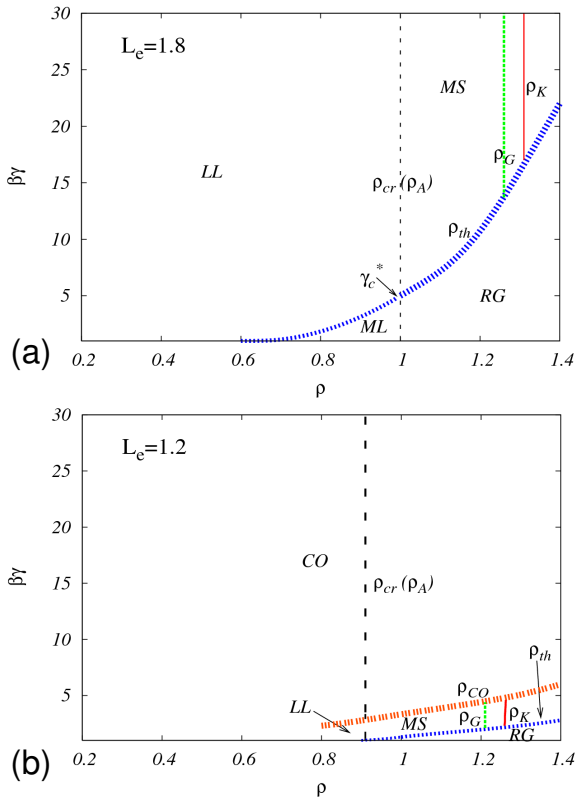

Figure 2.15: The state diagrams of a typical floppy network with $L_e = 1.8$ (a) and a typical tense network with $L_e = 1.2$ (b). These diagrams are constructed against the corresponding contour maps of liquid-like and glassy solutions, summarizing all possible phases partitioned by transition boundaries. In the $L_e = 1.8$ diagram, γ_c^* marks the crossing point of ρ_{th} curve (blue) and ρ_{cr} (or ρ_A) line (black dashed). The "mechanical" diagrams are further integrated with thermodynamic characteristics — laboratory glass transition density ρ_G (green dotted line) and Kauzmann density ρ_K (red full line). The floppy network exhibits higher ρ_G and ρ_K than the tense network does.

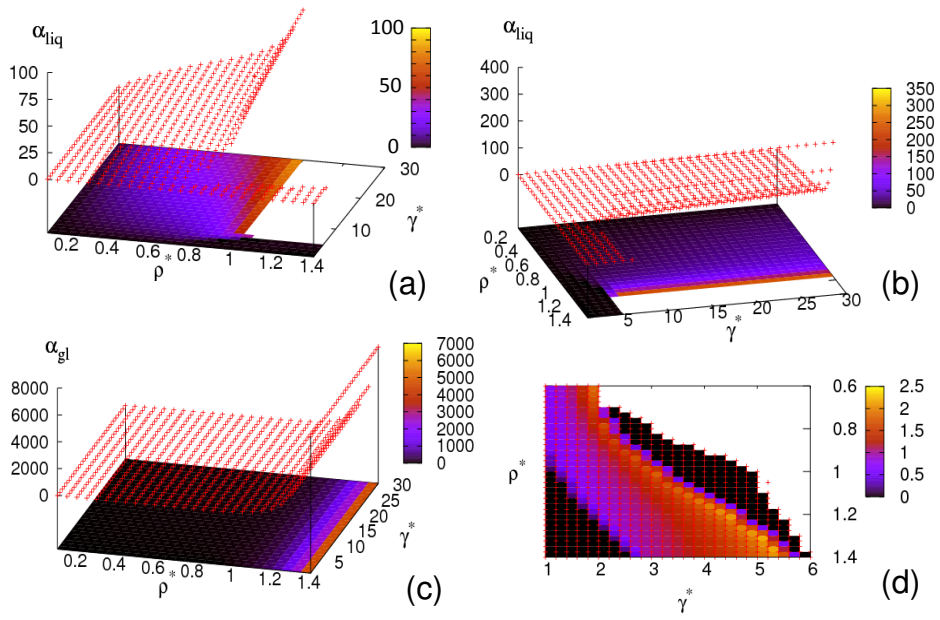

Figure 2.16: 2D surface and contour map of the localization strength for the case of $L_e = 1.2$ that features a persistent fraction of tense bonds. Upper panels: liquid-like solutions up to $\alpha_{liq} = 100$ (a) and $\alpha_{liq} = 350$ (b). Both the peeling-off stripe-shaped region for distinct liquid-like solutions and the smooth crossover to glassy behavior are explicitly displayed. (d) Amplified contour map for the stripe-shaped region; (c) glassy solutions over the whole parameter regime.

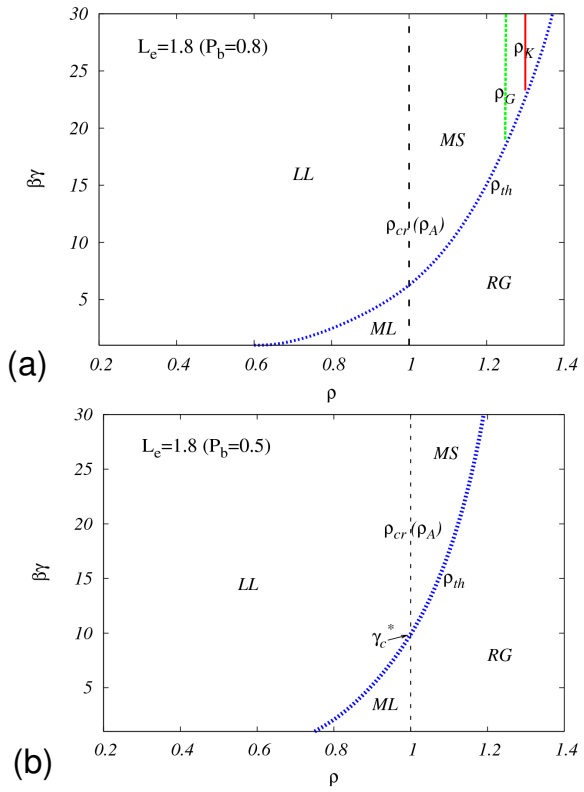

Figure 2.17: The state diagrams of a typical floppy network ($L_e = 1.8$) with different bonded fraction. ρ_K (red) and ρ_G (green) are defined as former. (a) $P_b = 0.8$; (b) $P_b = 0.5$: transition densities are absent due to the limited $\beta\gamma$ range shown here.

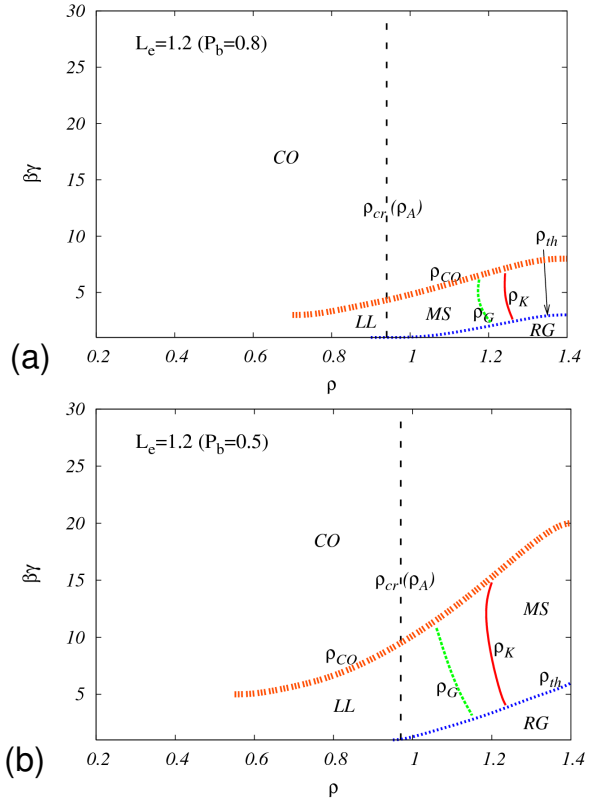

Figure 2.18: The state diagrams of a typical tense network ($L_e = 1.2$) with different bonded fraction. (a) $P_b = 0.8$; (b) $P_b = 0.5$. ρ_G and ρ_K become lower as the bonded fraction decreases.

Bibliography

[1] Howard, J. *Mechanics of Motor Proteins and the Cytoskeleton*, (Sinauer Assoc., Sunderland, MA, 2001).

[2] Michie, K. A. & Löwe, J. Dynamic filaments of the bacterial cytoskeleton. *Annu. Rev. Biochem.* **75,** 467–492 (2006).

[3] Xu, J. Y., Schwarz, W. H., Käs, J. A., Stossel, T. P., Janmey, P. A. & Pollard, T. D. Mechanical properties of actin filament networks depend on preparation, polymerization conditions, and storage of actin monomers. *Biophys. J.* **74,** 2731–2740 (1998).

[4] Pollard, T. D. & Borisy, G. G. Cellular motility driven by assembly and disassembly of actin filaments. *Cell* **112,** 453–465 (2003).

[5] Cameron, L. A., Robbins, J. R., Footer, M. J. & Theriot, J. A. Biophysical parameters influence actin-based movement, trajectory, and initiation in a cell-free system. *Mol. Biol. Cell* **15,** 2312–2323 (2004).

[6] Parekh, S. H., Chaudhuri, O., Theriot, J. A. & Fletcher, D. A. Loading history determines the velocity of actin-network growth. *Nat. Cell Biol.* **7,** 1219–1223 (2005).

[7] Chaudhuri, O., Parekh, S. H. & Fletcher, D. A. Reversible stress softening of actin networks. *Nature* **445,** 295–298 (2007).

[8] Weeds A. Actin-binding proteins–regulators of cell architecture and motility. *Nature* **296,** 811 (1982).

[9] Cunningham, C. C., Gorlin, J. B., Kwiatkowski, D. J., Hartwig, J. H., Janmey, P. A., Byers, H. R. & Stossel, T. P. Actin-binding protein requirement for cortical stability and efficient locomotion. *Science* **255,** 325–327 (1992).

[10] Janmey, P. A. Mechanical properties of cytoskeletal polymers. *Curr. Opin. Cell Biol.* **3,** 4–11 (1991).

[11] Boal, D. H. *Mechanics of the Cell* (Cambridge University Press, New York, 2002).

[12] Bausch, A. R. & Kroy, K. A bottom-up approach to cell mechanics. *Nature Phys.* **2,** 231–238 (2006).

[13] Janmey, P. A., McCormick, M. E., Rammensee, S., Leight, J. L., Georges, P. C. & MacKintosh, F. C. Negative normal stress in semiflexible biopolymer gels. *Nat. Mater.* **6,** 48–51 (2007).

[14] Costa, K. D., Hucker, W. J. & Yin, F. C. -P. Buckling of actin stress fibers: A new wrinkle in the cytoskeletal tapestry. *Cell Motil. Cytoskelet.* **52,** 266–274 (2002).

[15] Bendix, P. M., Koenderink, G. H., Cuvelier, D., Dogic, Z., Koeleman, B. N., Brieher, W. M., Field, C. M., Mahadevan, L. & Weitz, D. A. A quantitative analysis of contractility in active cytoskeletal protein networks. *Biophys. J.* **94,** 3126–3136 (2008).

[16] Fabry, B., Maksym, G. N., Butler, J. P., Glogauer, M., Navajas, D. & Fredberg, J. J. Scaling the microrheology of living cells. *Phys. Rev. Lett.* **87,** 148102 (2001).

[17] Gunst, S. J. & Fredberg, J. J. The first three minutes: smooth muscle contraction, cytoskeletal events, and soft glasses. *J. Appl. Physiol.* **95,** 413–425 (2003).

[18] Gardel, M. L., Shin, J. H., MacKintosh, F. C., Mahadevan, L., Matsudaira, P. & Weitz, D. A. Elastic behavior of cross-linked and bundled actin networks. *Science* **304,** 1301–1305 (2004).

[19] Trepat, X., Deng, L., An, S. S., Navajas, D., Tschumperlin, D. J., Gerthoffer, W. T., Butler, J. P. & Fredberg, J. J. Universal physical responses to stretch in the living cell. *Nature* **447,** 592–595 (2007).

[20] Zhou, E. H., Trepat, X., Park, C. Y., Lenormand, G., Oliver, M. N., Mijailovich, S. M., Hardin, C., Weitz, D. A., Butler, J. P. & Fredberg, J. J. Universal behavior of the osmotically compressed cell and its analogy to the colloidal glass transition. *Proc. Natl. Acad. Sci. USA* **106,** 10632–10637 (2009).

[21] Huisman, E. M., van Dillen, T., Onck, P. R. & Van der Giessen, E. Three-dimensional cross-linked F-Actin networks: Relation between network architecture and mechanical behavior. *Phys. Rev. Lett.* **99,** 208103 (2007).

[22] Shen, T. & Wolynes, P. G. Statistical mechanics of a cat's cradle. *New J. Phys.* **8,** 273 (2006).

[23] Koenderink, G. H., Dogic, Z., Nakamura, F., Bendix, P. M., MacKintosh, F. C., Hartwig, J. H., Stossel, T. P. & Weitz, D. A. An active biopolymer network

controlled by molecular motors. *Proc. Natl. Acad. Sci. USA* **106,** 15192–15197 (2009).

[24] Lenormand, G. & Fredberg, J. J. Deformability, dynamics, and remodeling of cytoskeleton of the adherent living cell. *Biorheology* **43,** 1–30 (2006).

[25] Verlet, L. & Weis, J. -J. Equilibrium theory of simple liquids. *Phys. Rev. A* **5,** 939–952 (1972).

[26] Fixman, M. Highly anharmonic crystal. *J. Chem. Phys.* **51,** 3270 (1969).

[27] Hall, R. W. & Wolynes, P. G. Microscopic theory of network glasses. *Phys. Rev. Lett.* **90,** 085505 (2003).

[28] Shen, T. & Wolynes, P. G. Nonequilibrium statistical mechanical models for cytoskeletal assembly: Towards understanding tensegrity in cells. *Phys. Rev. E* **72,** 041927 (2005).

[29] Stevenson, J. D., Walczak, A. M., Hall, R. W. & Wolynes, P. G. Constructing explicit magnetic analogies for the dynamics of glass forming liquids. *J. Chem. Phys.* **129,** 194505 (2008).

[30] Singh, Y., Stoessel, J. P. & Wolynes, P. G. Hard-sphere glass and the density-functional theory of aperiodic crystals. *Phys. Rev. Lett.* **54,** 1059 (1985).

[31] Hall, R. W. & Wolynes, P. G. Intermolecular forces and the glass transition. *J. Phys. Chem. B* **112,** 301–312 (2008).

[32] Zaccarelli, E. & Poon, W. C. K. Colloidal glasses and gels: The interplay of bonding and caging. *Proc. Natl. Acad. Sci. USA* **106,** 15203–15208 (2009).

[33] Kirkpatrick, T. R. & Wolynes, P. G. Connections between some kinetic and equilibrium theories of the glass transition. *Phys. Rev. A* **35,** 3072–3080 (1987).

[34] Kirkpatrick, T. R. & Thirumalai, D. Dynamics of the structural glass transition and the p-spin–interaction spin-glass model. *Phys. Rev. Lett.* **58,** 2091–2094 (1987).

[35] Kirkpatrick, T. R. & Wolynes, P. G. Stable and metastable states in mean-field Potts and structural glasses. *Phys. Rev. B* **36,** 8552–8564 (1987).

[36] Kauzmann, W. The nature of the glassy state and the behavior of liquids at low temperatures. *Chem. Rev.* **43,** 219–256 (1948).

[37] Dzero, M., Schmalian, J. & Wolynes, P. G. Activated events in glasses: The structure of entropic droplets. *Phys. Rev. B* **72,** 100201(R) (2005).

[38] Ingber, D. E. Cellular mechanotransduction: putting all the pieces together again. *FASEB J.* **20,** 811–827 (2006).

Chapter 3

Effective temperature and glassy dynamics of active matter

At the nanoscale and above we encounter active forms of matter in which internal or external energy sources supplement passive Brownian motion to allow large-scale structural rearrangements. Constant agitation by biomolecular motors and force-generating polymerizations allows the cytoskeleton of eukaryotes to undergo adaptive dynamical and structural changes in response to environmental disturbances. Other forms of active matter range from assemblies of entire microorganisms [1] to collections of artificial microscopic swimmers which are self-propelled [2, 3] and turbulently agitated active suspensions on the colloidal scale [4].

In this paper we show that, the steady-state statistical mechanics of these diverse out-of-equilibrium forms of active matter as well as their low-frequency fluctuations and responses can be described using the concept of an effective temperature. The notion of effective temperature has been useful in describing passive glassy systems [5], weakly driven systems such as gently sheared supercooled liquids and glasses [6, 7] and vibrated granular matter [8], driven vortex matter [9, 10], as well as in approximate theories and simulations of active biological matter [11, 12, 13, 14].

Modification of the fluctuation-dissipation theorem, signalling the nonequilibrium nature of the active processes like those in cells, has been directly observed

in the mechanical properties of reconstituted cytoskeletal networks [15, 16]. These measurements were consistent with an effective temperature nearly 100-fold higher than the ambient thermal temperature.

In this Communication we will show that on long time scales the effective temperature for systems with motor-driven active processes can be directly related to the properties of the motors. We describe the motors as generating a time series of isotropic kicks leading to a master equation description for the dynamics. By investigating this master equation in the small kick size limit we obtain an expression for T_{eff} explicitly depending on the total motor activity and the susceptibility of the motor dynamics to imposed mechanical forces. Motors lead to an enhanced diffusion for the active system regardless of their susceptibility. Our theory predicts also a linear relation between the effective diffusion coefficient and the rescaled effective temperature, which depends on motor susceptibility. Our prediction is confirmed by recent numerical studies of systems with adamant motors [17].

An important consequence of our analysis is that the effective temperature allows a simple rescaling of the equilibrium phase diagram to be used for the nonequilibrium motorized system. We show that the effective temperature coincides with the results based on previous self-consistent-field calculations [18]. Active matter often is jammed and in a glassy state. The present analysis implies that Lubchenko-Wolynes aging theory [19] can be taken over to describe jammed active matter simply by assigning the ambient temperature in that theory to be the motorized effective temperature and treating the fictive temperature, which measures the statistical structure of the system, as a history-dependent dynamically controlled variable as in structural glasses below their glass transition.

We start by following Shen and Wolynes [20] who modeled the stochastic nature of motor kicking via a master equation for the many-body probability distribution function $\Psi(\{\vec{r}\},t)$

$$\frac{\partial}{\partial t}\Psi(\{\vec{r}\},t) = (\hat{L}_{\text{FP}} + \hat{L}_{\text{NE}})\Psi(\{\vec{r}\},t). \tag{3.1}$$

Here $\hat{L}_{\text{FP}} = D_0 \sum_i \nabla_i \cdot \nabla_i - D_0\beta \sum_i \nabla_i \cdot (-\nabla_i U)$ is the usual many-body Fokker-Planck operator describing passive Brownian motion with D_0 denoting the thermal diffusion constant at bath temperature T and $\beta = 1/k_{\text{B}}T$. Hydrodynamic inter-

actions can be accounted for by extending the scalar diffusion coefficient D_0 to a diffusion tensor, $\boldsymbol{D}_{ij}$ [21], which depends on the particle configuration. This extension can be shown to respect the validity of an effective temperature which may become structure dependent. The gradient of the many-body interaction potential $U(\{\vec{r}\}) = U(\vec{r}_1, \vec{r}_2, \cdots, \vec{r}_n) = \sum_{<ij>} u(\vec{r}_i - \vec{r}_j)$ gives the local force thus the thermal drift motion of individual particles and $\vec{r}_i$ is the position of the ith particle. The potential U reflects an average over the solvent degrees of freedom and internal degrees of freedom of the motors and is thus strictly speaking a free energy. The effect of the nonequilibrium motor processes is summarized by an integral kernel $\hat{L}_{\mathrm{NE}}\Psi(\{\vec{r}\}, t) = \int \Pi_i d\vec{r_i'}[K(\{\vec{r'}\} \to \{\vec{r}\})\Psi(\{\vec{r'}\}, t) - K(\{\vec{r}\} \to \{\vec{r'}\})\Psi(\{\vec{r}\}, t)]$, where $K(\{\vec{r'}\} \to \{\vec{r}\})$ encodes the probability of transitions between different particle configurations. The (motor) kicking noise is thus a finite jump process with a rate that depends on whether the free energy is increased or decreased by a motor step

$$k = \kappa[\Theta(\Delta U)\exp(-s_u\beta\Delta U) + \Theta(-\Delta U)\exp(-s_d\beta\Delta U)]. \tag{3.2}$$

Here Θ is the Heaviside step function and $\Delta U = U\left(\vec{r} + \vec{l}\right) - U\left(\vec{r}\right)$ is the free energy change due to the kick identified by a vector $\vec{l}$. The kick step size l and the basal kicking rate κ define the dimensionless motor activity $\Delta := \kappa l^2/D_0$ which is analogous to the Peclet number in turbulent diffusion. This model rate couples the chemical reactions leading to the motor activity to the local mechanical forces acting on the motor; the assumed dependence upon *instantaneous* particle configuration reflects an assumed Markovian character of the dynamics without significant time delays. This is an idealization of the biochemical mechanism of real motors that doubtless possess intermediates in their function; such a non-Markovian character will lead to a frequency-dependence of the effective temperature. Also note that on time scales shorter than the inverse of the kicking rate, dynamics is governed by the usual Fokker-Planck part at thermal temperature, much as in collision models of chemical kinetics [22]. We parametrize the coupling of a motor to the external forces it must overcome by the motor susceptibility s which may take different values for uphill (s_u) moves and for downhill (s_d) moves. s_u and s_d depend on the chemical mechanism of the motors. When $s \to 1$ the motors are suscepti-

ble; they slow down when they go up against mechanical obstacles and accelerate when they take energetically downhill steps; in contrast $s \to 0$ corresponds to completely adamant motors which kick at an unperturbed rate being unaware of the instantaneous free energy landscape. Adamant motors use and waste a lot of energy.

Explicitly we write

$$\begin{aligned}\hat{L}_{\rm NE}\Psi(\{\vec{r}\},t) &= \kappa\sum_i \int d\hat{n}\int d\vec{r_i}\Big\{\delta(\vec{r_i}-\vec{r'}_i-\vec{l}\,)\\ &\times\ w[U(\cdots,\vec{r'}_i,\cdots)-U(\cdots,\vec{r}_i,\cdots)]\Psi(\{\vec{r'}\},t)\\ &-\ \delta(\vec{r}_i-\vec{r'}_i+\vec{l}\,)w[U(\cdots,\vec{r}_i,\cdots)-U(\cdots,\vec{r'}_i,\cdots)]\Psi(\{\vec{r}\},t)\Big\}.\end{aligned} \tag{3.3}$$

The angular integration denoted by $\int d\hat{n}$ averages over possible directions of kicking. For simplicity we provide results for the isotropic case. Again for simplicity we assume a fixed step length in the pair of delta functions. Our description of the rates gives $w[U_i-U_f] = \Theta(U_f-U_i)\exp[-s_u\beta(U_f-U_i)]+\Theta(U_i-U_f)\exp[-s_d\beta(U_f-U_i)]$.

When $s_u = s_d = s$, one finds even more simply

$$\begin{aligned}\hat{L}_{\rm NE}\Psi(\{\vec{r}\},t) = \kappa\sum_i\int d\hat{n}\Big\{&e^{-s\beta[U(\vec{r}_i)-U(\vec{r}_i-\vec{l})]}\\ &\times\Psi(\{\cdots,\vec{r'}_i=\vec{r}_i-\vec{l},\cdots\},t)\\ -&e^{-s\beta[U(\vec{r}_i+\vec{l})-U(\vec{r}_i)]}\Psi(\{\cdots,\vec{r}_i,\cdots\},t)\Big\}.\end{aligned} \tag{3.4}$$

We assume the kicking of different particles at any time is uncorrelated.

To obtain our promised results, we expand the distribution function and the kinetic rate in powers of $\vec{l}$ up to the quadratic order. This immediately leads to an effective Fokker-Planck equation

$$\frac{\partial}{\partial t}\Psi(\{\vec{r}\},t) = D_{\rm eff}\sum_i\Big\{\nabla_i^2\Psi-\nabla_i\cdot[(-\nabla_i\beta_{\rm eff}U)\Psi]\Big\}, \tag{3.5}$$

where

$$D_{\rm eff} = D_0\left(1+\frac{1}{2d}\frac{\kappa l^2}{D_0}\right), \tag{3.6}$$

$$(\beta_{\text{eff}}/\beta)^{-1} = T_{\text{eff}}/T = \left(1 + \frac{1}{2d}\frac{\kappa l^2}{D_0}\right) \Big/ \left(1 + \frac{s}{d}\frac{\kappa l^2}{D_0}\right). \tag{3.7}$$

Here the identity $\langle \cos^2\theta \rangle_{\hat{n}} = 1/d$ is used for general spatial dimension d. Rotational symmetry in motor susceptibility eliminates odd powers in $\vec{l}$ upon the angular integration.

These simple expressions (4.3)–(6.21) valid for general dimensions have nontrivial implications. First, in the small kick limit (kick step size is small compared to average particle separation yet the kicking rate can be quite high), the active system, while far from equilibrium in a strict sense, behaves as if it is at an effective equilibrium characterized by an effective temperature T_{eff} which will however be quite different from the thermal temperature T. It follows that the steady state is described by the effective Boltzmann distribution as $\Psi(\{\vec{r}\}) \propto \exp[-U(\{\vec{r}\})/k_{\text{B}}T_{\text{eff}}]$. Second, the approach to effective equilibrium is governed by an effective diffusion constant D_{eff} (Eq. (6.9)) which is enhanced by the active processes regardless of the motor adamancy. This is consistent with recent experimental observation on enhanced cytoplasmic diffusion which plays an important role in cytoskeletal assembly [16]. Finally, it is clear from Eq. (6.21) that T_{eff} can be predicted knowing only the motor activity $\Delta = \kappa l^2/D_0$ and the motor susceptibility s; susceptible motors with $s > 1/2$ yield $T_{\text{eff}} < T$; more interestingly, for very high motor activity, i.e., $\Delta \gg 1$, the effective temperature diverges as $T_{\text{eff}}/T \sim 1/(2s)$ as $s \to 0$, indicating that intense kicking by adamant motors leads to a very high effective temperature just as observed in experiments and simulation studies. In principle motors could have slip bonds [23, 24] leading to negative s and negative effective temperatures, a situation we will explore in another publication.

The results are easily generalized to the case of asymmetric susceptibility. It is not difficult to show that the factor $(s_u - s_d)$ accompanies all the cubic-and-above odd powers in $\vec{l}$ and thus doesn't modify the effective equilibrium at quadratic order. Eqs. (4.3)-(6.21) remain intact except for a direct substitution of $(s_u + s_d)/2$ for s. The effective temperature depends only on the *sum* of uphill and downhill susceptibility, and if $s_u + s_d = 1$ (i.e. $s = 1/2$) we have $T_{\text{eff}} = T$.

These predictions can be easily verified using results for various motile sys-

tems already studied numerically or experimentally. A testable prediction of our analysis is that $D_{\text{eff}}/D_0 = T_{\text{eff}}/T$ for completely adamant motors with $s = 0$. Numerical measurements of both the active diffusion constant and the effective temperature have been made by Loi *et al.* [17] for an adamantly motorized semi-flexible polymer melt simulated using molecular dynamics techniques. Our theoretical prediction is plotted in Fig. 3.1 along with their simulation results. The data points nicely fall on the predicted straight line at low-T_{eff} regime; even at relatively high T_{eff} ($\geq 4T$), only a modest deviation from the slope-1 line occurs which slowly increases with rising T_{eff}. The deviation is consistent with our scheme being perturbative in the kick size. There are of course also larger error bars in numerical experiments for the larger T_{eff} values. It will be interesting to test our theory for partially susceptible motors experimentally. Since D_{eff} is independent of s, for a given motor activity Δ, a higher susceptibility yields a lower T_{eff} and thus a larger slope for the linear relation between D_{eff}/D_0 and T_{eff}/T.

Besides this relation our theory suggests T_{eff} should increase quadratically with the kick step size for adamant motors, just as is experimentally observed for the dependence on the Peclet number found both in sedimentation experiments [3] for active colloidal suspensions under gravity, and in a numerical study of an active polymer melt [17].

In an earlier study of the glassy dynamics of an assembly of motorized particles Shen and Wolynes [20] pictured the motors as introducing a modification to the Debye-Waller factors of the localized particles. Their non-Hermitian variational approach to finding the steady state solution of the master equation turns out to be equivalent to closures for dynamic moments leading to an expression of the deviation of the total localization strength $\widetilde{\alpha}$ from its mechanical value α in terms of the motor properties. On the other hand local mechanical feedback within the self-consistent phonon theory [25] gives back an α for the central particle that depends on the $\widetilde{\alpha}$ of all its neighbors. Combining these two aspects allows a self-consistent determination of mean-field $(\alpha, \widetilde{\alpha})$ solutions and identification of stability behavior accordingly.

Assuming $s_u = s_d = s$, the second moment closure given earlier [20] reduces

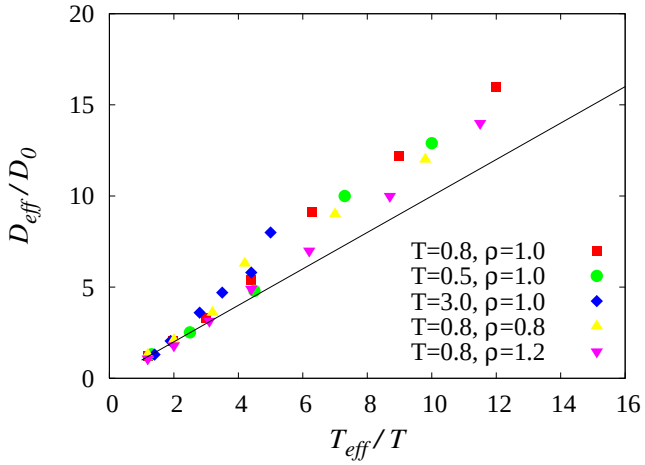

Figure 3.1: Rescaled diffusion constant versus rescaled effective temperature for a motorized semi-flexible polymer melt. The data points (colored symbols) were converted from Fig. 18 of Ref. [17]. The solid line with slope 1 gives the result predicted by the present theory.

to a simple expression

$$\frac{\tilde{\alpha}-\alpha}{\tilde{\alpha}} = \left(s-\frac{1}{2}\right)\frac{\kappa l^2}{dD_0}\, e^{s(s-1)\alpha l^2}. \tag{3.8}$$

Thus for $s = 1/2$ ($T_{\rm eff} = T$) chemical noise does not modify the mechanical stability ($\tilde{\alpha} = \alpha$); for $s < 1/2$ ($T_{\rm eff} > T$) stability is weakened ($\tilde{\alpha} < \alpha$) whereas for $s > 1/2$ ($T_{\rm eff} < T$) stability is enhanced ($\tilde{\alpha} > \alpha$).

Here we illustrate the connection to glassy dynamics by carrying out a self-consistent calculation (see Ref. [20] for the detailed procedure) for a motorized version of the cytoskeletal network modeled as a "cat's cradle" with excluded volume [18]. Superimposing the phase diagrams for active and equilibrium cases over the same parameter ranges as shown in Fig. 3.2 demonstrates that phase boundaries and characteristic densities scale just as we would predict from the kick size expansion.

The phase diagram shows diverse mechanical phases and possible transitions in between depending on the density (ρ) of the constituents and the effective stiffness ($\beta\gamma$) of the filamentous elements. In particular the coexistence of a loosely-tethered (LT) mobile phase and a repulsive-glass (RG) phase in the multiple-solution (MS) regime allows one to estimate the kinetic (ρ_G) and thermodynamic

(ρ_K) glass transition densities by matching the free energies of the mobile and glassy states.

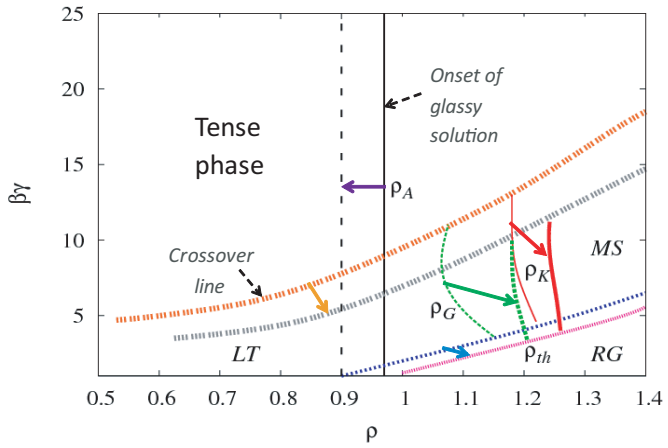

Figure 3.2: Superposed phase diagrams for the equilibrium and active cases for a cat's cradle with excluded volume having $D_0 = 0.025\,\mu\text{m}^2\text{s}^{-1}$, $s = 1$, $\kappa = 10\,\text{s}^{-1}$, and $l = 0.05\,\mu$m. Parameters are comparable to those for a cytoskeleton. The motor kick size l is much smaller than the typical crosslink separation which is on the order of 1-10μm. Solid arrows show the changes in characteristic behavior, pointing from the phase boundaries and glass transition densities for the equilibrium case to those for the active case. Above the upper phase boundary (the crossover line) the system is in the tense phase characterized by a smooth crossover from the loosely-tethered (LT) phase to the repulsive-glass (RG) phase as the crosslink density ρ increases. Below the lower phase boundary (marked by ρ_{th}) the mobile phase becomes unstable and only the glassy state can be stabilized. Ref. [18] gives details of the analysis for the equilibrium case.

With both susceptible ($s = 1$) and small-size ($l = 0.05\mu$m) motor kicks, the variety of mechanical phases remains intact; but the phase boundaries shift due to the nonequilibrium effects. The decrease in ρ_A leads to an enlarged stability region for the glassy state, while increases in glass transition densities ρ_G and ρ_K suggest that susceptible motor kicking can help resolve local constraints and thus allows a deeper descent into the energy landscape, leading to a denser packing where eventually structural rearrangements become too slow to be observed. The downward shift of both phase boundaries is simply captured by rescaling the equilibrium phase diagram with the inverse temperature ratio β_{eff}/β given by Eq. (6.21). Adamant motor kicking gives rise to the opposite effect heating the

system above its thermal temperature and reducing the glass transition density. Therefore equilibrium phase diagrams are still valid in the small kick limit yet with T being replaced by T_{eff}.

The fact that the master equation precisely reduces to a Fokker-Planck equation allows us to apply the effective temperature to analyze the dynamics/kinetics of systems that are structurally out-of-equilibrium, i.e., jammed. The slow relaxation of the cytoskeletal mechanics [26] thus is related to glassy behavior in the aging regime. Quantitatively, jammed cytoskeletal systems should be described by the aging theory for structural glasses developed by Lubchenko and Wolynes [19]. It is only necessary to replace in their theory the absolute ambient temperature which describes vibrations in glasses by the effective temperature of the motors. The fictive temperature reflecting the statistical structure of the cytoskeleton will be history dependent. This mapping should make it possible to predict the dependence on motor properties of the rheology of active matter.

Chapter 3, in full, is a reprint of the material as it appears in the Journal of Chemical Physics **135** 051101 (2011), S. Wang and P. G. Wolynes. The dissertation/thesis author was the primary investigator and author of this paper.

Bibliography

[1] Simha, R. A. & Ramaswamy, S. Hydrodynamic fluctuations and instabilities in ordered suspensions of self-propelled particles. *Phys. Rev. Lett.* **89,** 058101 (2002); Hatwalne, Y., Ramaswamy, S., Rao, M. & Simha, R. A. Rheology of active-particle suspensions. *Phys. Rev. Lett.* **92**, 118101 (2004).

[2] Deseigne, J., Dauchot, O. & Chaté, H. Collective motion of vibrated polar disks. *Phys. Rev. Lett.* **105,** 098001 (2010).

[3] Palacci, J., Cottin-Bizonne, C., Ybert, C. & Bocquet, L. Sedimentation and effective temperature of active colloidal suspensions. *Phys. Rev. Lett.* **105,** 088304 (2010).

[4] Ilievski, F., Mani, M., Whitesides, G. M. & Brenner, M. P. Self-assembly of magnetically interacting cubes by a turbulent fluid flow. *Phys. Rev. E* **83,** 017301(2011).

[5] Cugliandolo, L. F., Kurchan, J. & Peliti, L. Energy flow, partial equilibration, and effective temperatures in systems with slow dynamics. *Phys. Rev. E* **55,** 3898 (1997).

[6] Berthier, L. & Barrat, J.-L. Nonequilibrium dynamics and fluctuation-dissipation relation in a sheared fluid. *J. Chem. Phys.* **116,** 6228 (2002); *Phys. Rev. Lett.* **89,** 095702 (2002).

[7] Haxton, T. K. & Liu, A. J. Activated dynamics and effective temperature in a steady state sheared glass. *Phys. Rev. Lett.* **99,** 195701 (2007).

[8] Makse, H. & Kurchan, J. Testing the thermodynamic approach to granular matter with a numerical model of a decisive experiment. *Nature (London)* **415,** 614–617 (2002).

[9] Koshelev, A. E. & Vinokur, V. M. Dynamic melting of the vortex lattice. *Phys. Rev. Lett.***73,** 3580 (1994).

[10] Kolton, A. B., Exartier, R., Cugliandolo, L. F., Domínguez, D. & Grønbech-Jensen, N. Effective temperature in driven vortex lattices with random pinning. *Phys. Rev. Lett.* **89,** 227001 (2002).

[11] Martin, P., Hudspeth, A. J. & Jülicher, F. Comparison of a hair bundle's spontaneous oscillations with its response to mechanical stimulation reveals the underlying active process. *Proc. Natl. Acad. Sci. USA* **98,** 14380–14385 (2001).

[12] Lu, T., Hasty, J. & Wolynes, P. G. Effective temperature in stochastic kinetics and gene networks. *Biophys. J.* **91,** 84–94 (2006).

[13] Ziebert, F. & Aranson, I. S. Rheological and structural properties of dilute active filament solutions. *Phys. Rev. E* **77,** 011918 (2008).

[14] Loi, D., Mossa, S. & Cugliandolo, L. F. Effective temperature of active matter. *Phys. Rev. E* **77,** 051111(2008); Effective temperature of active complex matter. *Soft Matter* **7,** 3726–3729 (2011).

[15] Mizuno, D., Tardin, C., Schmidt, C. F. & MacKintosh, F. C. Nonequilibrium mechanics of active cytoskeletal networks. *Science* **315,** 370–373 (2007).

[16] Brangwynne, C. P., Koenderink, G. H., MacKintosh, F. C. & Weitz, D. A. Cytoplasmic diffusion: molecular motors mix it up. *J. Cell Biol.* **183,** 583–587 (2008).

[17] Loi, D., Mossa, S. & Cugliandolo, L. F. Effective temperature of active complex matter. *Soft Matter* **7,** 3726–3729 (2011).

[18] Wang, S., Shen, T. & Wolynes, P. G. The interplay of nonlinearity and architecture in equilibrium cytoskeletal mechanics. *J. Chem. Phys.* **134,** 014510 (2011).

[19] Lubchenko, V. & Wolynes, P. G. Theory of aging in structural glasses. *J. Chem. Phys.* **121,** 2852 (2004).

[20] Shen, T. & Wolynes, P. G. Stability and dynamics of crystals and glasses of motorized particles. *Proc. Natl. Acad. Sci. USA* **101,** 8547–8550 (2004); Nonequilibrium statistical mechanical models for cytoskeletal assembly: Towards understanding tensegrity in cells. *Phys. Rev. E* **72,** 041927 (2005).

[21] Wolynes, P. G. & Deutch, J. M. Dynamical orientation correlations in solution. *J. Chem. Phys.* **67**, 733 (1977).

[22] Skinner, J. L. & Wolynes, P. G. Derivation of Smoluchowski equations with corrections for Fokker-Planck and BGK collision models. *Physica***96A,** 561–572 (1979).

[23] Alon, R., Hammer, D. A. & Springer, T. A. Lifetime of the P-selectin-carbohydrate bond and its response to tensile force in hydrodynamic flow. *Nature***374,** 539–542 (1995).

[24] Dudko, T. A., Hummer, G. & Szabo, A. Intrinsic rates and activation free energies from single-molecule pulling experiments. *Phys. Rev. Lett.* **96,** 108101 (2006).

[25] Fixman, M. Highly anharmonic crystal. *J. Chem. Phys.* **51,** 3270 (1969).

[26] Bursac, P., Lenormand, G., Fabry, B., Oliver, M., Weitz, D. A., Viasnoff, V., Butler, J. P., & Fredberg, J. J. Cytoskeletal remodelling and slow dynamics in the living cell. *Nature Mater.* **4,** 557–561 (2005).

Chapter 4

On the spontaneous collective motion of active matter

4.1 Introduction

Spontaneous directed motion driven by active processes is crucial to biology. Such motion is only possible because the cell is a far-from-equilibrium many-body system. The cytoskeleton of eukaryotic cells is built, maintained and adaptively reorganized through active transport and force generation powered by ATP hydrolysis. Oscillations of the mitotic spindle during cell division [1] and cytoplasmic streaming [2] dramatically illustrate that the cell is not at equilibrium. Driven motions of cells are also important at higher levels of organization in living things ranging from mechanosensation [3] to the developmental processes in which the genetic code unfolds to create a multicellar organism [4]. Sustained spontaneous collective motion is quite remarkable in many-body physics. Superfluidity and superconductivity are examples of metastable states of motion made possible by quantum statistics. The biological example provided by the cytoskeleton is seemingly quite different leading not to infinitely long-lived states but to ones that go away when the cell is depleted of fuel and dies. Nevertheless, like the quantum examples, the motion of the cytoskeleton is an emergent many-body phenomenon reflecting broken symmetries.

Here we explore the origin of spontaneous collective motion for systems of many interacting biomacromolecules with motor-driven active processes using a systematic perturbative expansion of the many-body master equation treating nonequilibrium motorized processes. We model the motors as generating a time series of isotropic kicks on the constituents of a many-body assembly. Earlier [5] we showed that quite generally the corresponding master equation, when expanded to the lowest order in the kick step size, yields an effective temperature, $T_{\rm eff}$, which explicitly depends on the total motor activity and on the way in which motors respond to imposed forces. A system described by an effective temperature alone [6, 7, 8] cannot undergo spontaneous directed motion unless it is quantum mechanical so that spatial and momentum degrees of freedom are coupled by the uncertainty principle. Pursuing the expansion to higher order, however, reveals the possible emergence of spontaneous directed collective motion quite generally from a quiescent homogeneous state, albeit one with rigidity owing to broken translational symmetry, as in a glass. The underlying dynamic instability is induced by a sufficiently strong internal agitation in terms of kick step size. This provides a general mechanism for spontaneous flows in an active assembly of interacting constituents.

Combining a linear stability analysis with a trial solution of the many-body master equation allows us to identify possible dynamic phases that depend on the motor kick step size and susceptibility. We find that for sufficiently large kicks and high activity, susceptible motors, i.e., motors whose kick rate depends on the forces exerted on them, can generate spontaneous flow, whereas adamant motors, indifferent to imposed forces, would merely drive fluidization of an active system. We have also carried out simulations on a minimal cytoskeleton model incorporating motor dynamics to compare with our analytical predictions. The simulations not only verify the predicted phase diagram, but also highlight how the combination of network connectivity with motor susceptibility determines the formation of nonequilibrium structures. The simulations show an oscillatory phase separation at intermediate network connectivity and formation of aster-like patterns/bundle-connected poles when driven by motors with negative susceptibility, i.e., motors

that move against the force, energetically uphill. The latter corresponds to a negative-temperature system where interesting structures emerge much like vortex condensation in two-dimensional turbulence [9, 10, 11].

We are far from the first to try to understand the physics of spontaneous collective motion in biology. Jülicher and Prost [12] studied a one-dimensional stochastic model which assumed an underlying ratchet potential already breaking translational symmetry. Motor cooperativity then leads to a dynamical phase transition to spontaneous directed motion despite the system's spatial symmetry. Thinking of the cytoskeleton, an assembly of filamentous polar polymers actively connected by crosslinkers, as an active polar gel has allowed the construction of continuum theories, based on conservation laws and symmetry considerations, which also generate active flows [13, 14, 15, 16]. Pattern formation in active fluids has also been discussed based on a reaction-diffusion-advection mechanism [17].

4.2 Model

Here we model the stochastic nature of the motor kicking via a master equation for the many-body probability distribution function $\Psi(\{\vec{r}\},t)$ [18, 19]

$$\frac{\partial}{\partial t}\Psi(\{\vec{r}\},t) = (\hat{L}_{\rm FP} + \hat{L}_{\rm NE})\Psi(\{\vec{r}\},t). \tag{4.1}$$

Here $\hat{L}_{\rm FP} = D_0 \sum_i \nabla_i \cdot \nabla_i - D_0\beta \sum_i \nabla_i \cdot (-\nabla_i U)$ is the usual many-body Fokker-Planck operator describing passive Brownian motion with D_0 denoting the ordinary diffusion coefficient at ambient temperature T and $\beta = 1/k_{\rm B}T$. The gradients of the many-body interaction potential $U(\{\vec{r}\}) = U(\vec{r}_1, \vec{r}_2, \cdots, \vec{r}_n) = \sum_{<ij>} u(\vec{r}_i - \vec{r}_j)$ give the local forces acting on individual particles, where $\vec{r}_i$ is the position of the ith particle and $\langle \cdots \rangle$ denotes the nearest neighbor pairs. Note that the potential U reflects an average over the solvent degrees of freedom and internal degrees of freedom of the motors and is thus strictly speaking a free energy. The effects due to nonequilibrium motorized processes are summarized by an integral kernel $\hat{L}_{\rm NE}\Psi(\{\vec{r}\},t) = \int \Pi_i d\vec{r_i'}[K(\{\vec{r'}\} \to \{\vec{r}\})\Psi(\{\vec{r'}\},t) - K(\{\vec{r}\} \to \{\vec{r'}\})\Psi(\{\vec{r}\},t)]$, where $K(\{\vec{r'}\} \to \{\vec{r}\})$ encodes the probability of transitions between different particle configurations per unit time. Motor kicking noise is a finite jump process with a

rate that depends on whether the free energy is increased or decreased when a step is made

$$k = \kappa[\Theta(\Delta U)\exp(-s_u\beta\Delta U) + \Theta(-\Delta U)\exp(-s_d\beta\Delta U)]. \tag{4.2}$$

Here Θ is the Heaviside step function and $\Delta U = U\left(\vec{r}+\vec{l}\right) - U\left(\vec{r}\right)$ is the free energy change due to the kick identified by a vector $\vec{l} = l\hat{n}$. The kick step size l and the basal kicking rate κ define the dimensionless motor activity $\Delta := \kappa l^2/D_0$, an analog of the Peclet number in turbulent diffusion. This model rate couples the chemical reactions leading to the motor activity to the local mechanical forces acting on the motor being parametrized by the susceptibility s which may take different values for uphill (s_u) moves and for downhill (s_d) moves depending on the biochemical mechanism of the motors. When $s \to 1$ the motors are susceptible, slowing down when they climb up against obstacles and accelerating when they move energetically downhill; in contrast $s \to 0$ corresponds to completely adamant motors which kick at a rate unperturbed by the free energy landscape.

4.3 Systematic expansion and stability analysis

To examine the small kick size limit, we first expand the equation in powers of $\vec{l}$ up to the quadratic order. The simplest case, isotropic kicking and symmetric susceptibility (i.e., $s_u = s_d = s$) leads directly to an effective Fokker-Planck equation [5]

$$\frac{\partial}{\partial t}\Psi(\{\vec{r}\},t) = D_{\text{eff}}\sum_i\left\{\nabla_i^2\Psi - \nabla_i\cdot[(-\nabla_i\beta_{\text{eff}}U)\Psi]\right\}, \tag{4.3}$$

where

$$D_{\text{eff}} = D_0\left(1+\frac{1}{2d}\frac{\kappa l^2}{D_0}\right), \tag{4.4}$$

$$(\beta_{\text{eff}}/\beta)^{-1} = T_{\text{eff}}/T = \left(1+\frac{1}{2d}\frac{\kappa l^2}{D_0}\right)\Big/\left(1+\frac{s}{d}\frac{\kappa l^2}{D_0}\right). \tag{4.5}$$

These simple expressions (Eqs. 4.3–6.21) valid for general spatial dimensions d have nontrivial implications. In the small kick limit, the active system, while out of equilibrium, behaves as if it is at an effective canonical equilibrium characterized by an effective temperature T_{eff}. The effective diffusion constant D_{eff} (Eq. 6.9) is

enhanced by the active processes regardless of motor adamancy, consistent with recent observations of enhanced cytoplasmic diffusion [20]. T_{eff} (Eq. 6.21) is fully determined by the motor activity $\Delta = \kappa l^2/D_0$ and the motor susceptibility s; susceptible motors with $s > 1/2$ yield $T_{\text{eff}} < T$. When motor activity dominates over thermal noise, i.e., $\Delta \gg 1$, the effective temperature diverges as $T_{\text{eff}}/T \sim 1/(2s)$ as $s \to 0$. Thus intense kicking by adamant motors leads to a very high effective temperature just as observed in experiments [21] and simulation studies [22, 23]. A more detailed discussion can be found in a separate work [5].

To probe the dynamic instability that may give rise to the spontaneous motion, we must go beyond the effective equilibrium and expand to quartic order in l obtaining

$$\begin{aligned} \frac{\partial}{\partial t}\Psi(\{\vec{r}\},t) &= D_{\text{eff}}\sum_i \left\{\nabla_i^2\Psi - \nabla_i\cdot[(-\nabla_i\beta_{\text{eff}}U)\Psi]\right\} \\ &+ \kappa l^4\langle\cos^4\theta\rangle_{\hat{n}} \times \sum_i F_i(\nabla_i^{(m)}U, \nabla_i^{(n)}\Psi). \end{aligned} \tag{4.6}$$

The functional F_i is the divergence of a flux, i.e., $F_i = -\nabla_i\cdot\vec{J}_i^a$, where $\vec{J}_i^a$ is the probability current due to active events on particle i given by

$$\begin{aligned} -\vec{J}_i^a &= \frac{1}{24}\nabla_i^3\Psi + \frac{s}{12}\nabla_i\left(\nabla_i^2\beta U\Psi\right) + \frac{s}{6}\nabla_i\beta U\nabla_i^2\Psi \\ &+ \frac{s^2}{4}(\nabla_i\beta U)^2\nabla_i\Psi + \frac{s^3}{6}(\nabla_i\beta U)^3\Psi. \end{aligned} \tag{4.7}$$

While at quadratic order in l a motor-driven system exhibits enhanced diffusive dynamics at an effective equilibrium, at quartic order, a net streaming flow becomes possible, as in models of nonequilibrium gene switch [24].

In an earlier study of the stability and dynamics of a motorized assembly Shen and Wolynes [18] pictured the motors as introducing a modification to the Debye-Waller factors of the localized particles. They found an expression of the deviation of the total localization strength $\widetilde{\alpha}$ from its thermal value α in terms of the motor properties. Thermal self-consistent phonon theory [25] gives α for a central particle that depends on the $\widetilde{\alpha}$ of all its neighbors. Combining these two aspects allows a self-consistent determination of mean-field $(\alpha, \widetilde{\alpha})$ solutions allowing an identification of static stability limits. Assuming $s_u = s_d = s$,

the second moment closure [19] reduces to a simple expression $(\widetilde{\alpha} - \alpha)/\widetilde{\alpha} = (s - 1/2)\exp\left[s(s-1)\alpha l^2\right]\kappa l^2/dD_0$. Thus for $s = 1/2$ ($T_{\text{eff}} = T$) chemical noise does not modify the mechanical stability ($\widetilde{\alpha} = \alpha$); for $s < 1/2$ ($T_{\text{eff}} > T$) stability is weakened ($\widetilde{\alpha} < \alpha$) whereas for $s > 1/2$ ($T_{\text{eff}} < T$) stability is enhanced ($\widetilde{\alpha} > \alpha$).

For spontaneous collective motion there must be a nontrivial dynamic first moment that indicates a moving fiducial lattice. The second moment still has its steady-state value describing vibrations about the fiducial configuration. We thus write down a trial function of the master equation as a collection of Gaussians with moving centers and a steady variance

$$\Psi(\{\vec{r}_i\};\widetilde{\alpha}) = \Pi_i \left(\widetilde{\alpha}/\pi\right)^{d/2} e^{-\widetilde{\alpha}[\vec{w}_i - \vec{m}_i(t)]^2}, \tag{4.8}$$

where $\vec{w}_i = \vec{r}_i - \vec{R}_i$ denotes the displacement of particle i from its equilibrium position $\vec{R}_i$, $\vec{m}_i(t) = \langle \vec{w}_i | \Psi \rangle$ defines the dynamic first moment of particle i, and the total localization strength $\widetilde{\alpha}$ of individual particles is inversely related to the second moment.

To account for the neighbor-coupling effects we adopt the *coupled*-oscillator expansion of the effective potential, V_e, used earlier by Stoessel and Wolynes [26]. Here the gradient of the general many-body free energy becomes $\nabla_i \beta U = \sum_{j \in n.n.} \nabla_i \nabla_i \beta V_e(R_{ij}) \cdot (\vec{w}_i - \vec{w}_j)$, where $R_{ij} = |\vec{R}_i - \vec{R}_j|$ denotes the equilibrium separation between the central particle i and its nearest neighbor j. The curvature then follows $\nabla_i^2 \beta U = \sum_{j \in n.n.} Tr[\nabla_i \nabla_i \beta V_e(R_{ij})] = 2d\,\alpha$. The mechanical localization strength is defined by $\alpha = (1/2d)\sum_j \nabla_{R_{ij}}^2 \beta V_e(R_{ij})$. Higher order gradients of βU vanish at this level of coupling. A nonzero α reflects a (possibly amorphous) state of broken translational invariance, as in a gel. Applying the first moment closure $\partial_t \langle \vec{w}_i | \Psi \rangle = \langle \vec{w}_i | (\hat{L}_{\text{FP}} + \hat{L}_{\text{NE}}) \Psi \rangle$ to Eq. 4.6 with the Gaussian ansatz (Eq. 4.8) as well as the coupled-oscillator expansion of the effective potential leads to coupled equations for the $\vec{m}_i$'s.

To investigate the emergence of directed motion, we carry out a linear stability analysis about the non-moving state (i.e. $\vec{m}_i = 0$). In view of the biological relevance of one-dimensional scenarios, such as the filament sliding in motility assay [27] and flow in the cell cortex [28], we focus here on the 1D case. Consider a

spatially varying trial solution of the form

$$m_i(t) = \Re[\bar{m}\, e^{r_k t + \mathrm{i}kR_i}], \tag{4.9}$$

where $\bar{m}$ denotes the amplitude of the first moment, k the wavenumber of the spatial modulation and r_k the growth rate. Even if kicks are isotropic and the interaction Hamiltonian preserves rotational symmetry, spontaneous symmetry breaking occurs giving flow in a specific direction.

In the long-wavelength limit one finds

$$\partial_t m_i = \frac{k^2}{2}\Big\{ \sum_j \partial_i^2 \beta V_e(R_{ij})(R_j - R_i)^2 \Big\} f(l, s; \alpha, \widetilde{\alpha}) m_i, \tag{4.10}$$

where

$$\begin{aligned} f(l, s; \alpha, \widetilde{\alpha}) &= -D_0 - s\kappa l^2 + s^2 \kappa l^4 \alpha \\ &- s^3 \kappa l^4 \Big\{ \frac{\alpha^2}{\widetilde{\alpha}} + \frac{1}{4\widetilde{\alpha}} \sum_j \left[\partial_i^2 \beta V_e(R_{ij})\right]^2 \Big\}. \end{aligned} \tag{4.11}$$

Since $\partial_t m_i = r_k m_i$, the growth rate is proportional to $k^2 f(l, s; \alpha, \widetilde{\alpha})$ up to $O(k^2)$. It follows that a strictly uniform state ($k = 0$) would not undergo small-amplitude dynamic instability regardless of the motor activity and susceptibility but the non-moving state is barely stable in the absence of spatial modulation. Moreover, the sign of $f(l, s; \alpha, \widetilde{\alpha})$ determines the stability behavior for small but finite k. When the kick step size l is small, f is negative indicating diffusive relaxation towards the non-moving state. As l increases, instabilities grow: f, thus r_k, becomes positive, signifying a collective flow in a spatially modulated state, when l exceeds a threshold value l_{th} given by

$$l_{\mathrm{th}}^2 = \frac{1 + \sqrt{1 + 4\frac{\alpha D_0}{\kappa}\left(1 - s\{\frac{\alpha}{\widetilde{\alpha}} + \frac{1}{4\alpha\widetilde{\alpha}} \sum_j \left[\partial_i^2 \beta V_e(R_{ij})\right]^2\}\right)}}{2(s\alpha)\left(1 - s\{\frac{\alpha}{\widetilde{\alpha}} + \frac{1}{4\alpha\widetilde{\alpha}} \sum_j \left[\partial_i^2 \beta V_e(R_{ij})\right]^2\}\right)}. \tag{4.12}$$

At high motor activity such that $\widetilde{\alpha} \gg \alpha$ and $\kappa \gg \alpha D_0$, $l_{\mathrm{th}}^2 \sim 1/(s\alpha) + D_0/(s\kappa)$. Thus high susceptibility s and kicking rate κ and large α lead to a low instability threshold (see Supplementary Fig. 4.6 for a detailed illustration). Note that assuming a statistically homogeneous structure will remove the i-dependence of f

and l_{th}. For the case of asymmetric susceptibility ($s_u \neq s_d$), the factor ($s_u - s_d$) accompanies all the cubic-and-above odd powers in $\vec{l}$ in the expansion, leading to a smaller threshold kick size compared to that for the symmetric case where corrections start at quartic order in l.

We carried out the self-consistent calculation described earlier on a minimal model of the cytoskeleton as a cat's cradle [29, 30] to determine $(\alpha, \widetilde{\alpha})$ and used this to obtain the growth rate for a model network consisting of nonlinear elastic filaments characterized by relaxed length L_e and stretching stiffness $\beta\gamma$ built on a three dimensional random lattice of crosslinks at density ρ. The network connectivity P_c is defined as the fraction of nearest-neighbor pairs of crosslinks connected by filaments. The unit of length is the average separation between the neighboring crosslinks.

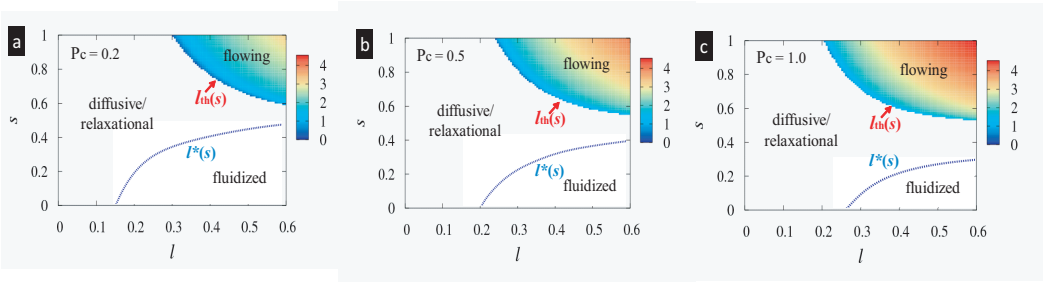

Figure 4.1: Phase diagram for possible dynamic states. The parameter plane indicates the motor kick step size l and the motor susceptibility s. The model cytoskeleton used to obtain α and $\widetilde{\alpha}$ is characterized by crosslink density $\rho = 0.8$, relaxed length of the filaments $L_e = 1.2$ and stretching stiffness $\beta\gamma = 5$. From panel (a) to (c), the network connectivity varies with $P_c = 0.2, 0.5$, and 1, respectively. $D_0 = 0.1$ and $\kappa = 20$. In the flowing regime, there are stable nontrivial (α,$\widetilde{\alpha}$) solutions and positive r_k; in the diffusive/relaxational regime, while there are stable nontrivial (α,$\widetilde{\alpha}$) solutions there is a small negative r_k; in the fluidized regime, finite (α,$\widetilde{\alpha}$) solutions are unstable. As network connectivity rises, the flowing phase region expands whereas the fluidized state region shrinks. The logarithm of the normalized growth rate r_k/k^2 for flowing instability is color-coded, showing the increase of instability with l and s.

In Fig. 4.1 we show the phase diagrams for possible dynamic states as a function of kick size l and susceptibility s for several values of the network connectivity. In all the cases, there are two stability boundaries, one for small s

($s < 1/2$), one for large s ($s > 1/2$). In the low-s regime, as l reaches a critical value, $l^*(s)$ (blue dotted line), finite solutions for $(\alpha, \widetilde{\alpha})$ become unstable, i.e., the system becomes fluidized. In the high-s corner, when l exceeds a threshold value $l_{\rm th}$ (lower boundary of the color-coded region), instability occurs for small but finite k modes indicating the emergence of modulated flowing states. In this region, stable finite $(\alpha, \widetilde{\alpha})$ solutions exist with $\widetilde{\alpha}$ being considerably larger than α, reflecting the enhancement of stability by susceptible motor kicking. Note that as motor susceptibility increases, the threshold kick step size decreases. In the rest of the diagram, α and $\widetilde{\alpha}$ are comparable and the negative growth rate indicates diffusive modes. (Close to detailed balance, $s = 1/2$, diffusive modes persist over the entire relevant range of l.)

In the figures, we color-code the logarithm of the normalized growth rate r_k/k^2 for the flow instability; the growth rate increases with l and s. Comparing the diagrams for different values of connectivity, we see that as P_c increases, the region corresponding to the fluidized state shrinks, since increasing the number of bond constraints stabilizes the system against fluidization. On the other hand, the region corresponding to flow expands toward lower l (and lower s slightly), suggesting that as the mechanical feedback increases (larger α due to higher P_c), a smaller kick is able to trigger the flowing instability when the motors are susceptible.

4.4 Simulations

To check these predictions we performed dynamic Monte Carlo [31] simulations on the model cytoskeleton [29, 30]. In these simulations we generated initially a three-dimensional random lattice of volumeless nodes (mimicking the crosslinking proteins) and connected the nearest-neighbor nodes (defined by the first shell of the pair distribution function) with nonlinear elastic bonds [30] (mimicking the filamentous proteins) at a given probability P_c. Thermal steps obey Brownian dynamics [32] whereas chemical moves follow the stochastic process defined by the model kicking statistics (5.1). The simulations reveal an interesting interplay of network connectivity with the motor susceptibility dramatically affecting struc-

tural development.

At a relatively high network connectivity, $P_c \simeq 0.5$ (average coordination number $z \simeq 6$), force transmission through the bonds is efficient and the network structure remains statistically homogeneous in the presence of the motor-driven processes. Nevertheless, varying motor susceptibility drastically changes the dynamics.

Fluidized state: Under completely adamant kicks ($s = 0$) with a moderately large step size ($l > l^*$), nodes rapidly become fluidized. Elastic stretching of the bonds imposes no constraint on the node motion resulting in vanishing localization strength and zero net flow ($\vec{m} = 0$). Consequently, as shown in Fig. 4.2a, almost all the initially floppy bonds (in green) get stretched (in red) and the network becomes very tense.

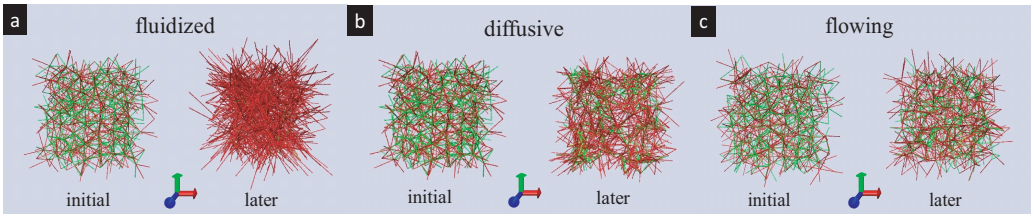

Figure 4.2: Network structure for various dynamic phases. (a) Fluidized phase with $s = 0$. An initially relaxed (left) network rapidly tenses up (right) under completely adamant motor kicking. Localization strength of the nodes vanishes and there is no net flow. (b) Diffusive phase with $s = 0.2$. Spots of concentrated tense/floppy filaments are visible. Nodes exhibit enhanced diffusive motion with a finite localization strength. No spontaneous flow occurs. (c) Flowing phase with $s = 1$. Network structure remains homogeneous despite the spontaneous flowing motion, reflecting the enhanced rigidity of the structure and coherence of motion by susceptible motor kicking. $L_e = 1.2$, $\beta\gamma = 5$, $P_c = 0.5$ and $l = 0.25$. Red lines stand for tense filaments and green lines for floppy filaments.

Flowing state: At the other extreme, however, under susceptible kicks ($s = 1$) with above-threshold step size $l > l_{\text{th}}$, a self-sustained flow develops and the nodes vibrate about a steadily moving fiducial lattice (see Supplementary Fig. 4.7 for statistical characteristics of the flowing state) both for regular lattices and for random structures. Apparently disorder in the structure, inherent in the quenched connectivity or dynamically generated through initial random motions, gives rise

to local force asymmetry. Sufficiently large kicks then trigger dynamic instability of the quiescent state; the resultant nucleation and propagation of local coordinated motion, mediated by force transmission and orchestrated by susceptible motor kicking, finally leads to a global concerted movement of the whole lattice. High motor susceptibility promotes cooperativity, resulting in "rigidity" of the structure and coherent collective motion. As can be seen in Fig. 4.2c, the network structure remains homogenous without significant local distortions.

Diffusive state: When the motors are only moderately susceptible ($s : 0.2 - 0.5$) but not sufficiently cooperative to drive spontaneous flow, the system exhibits enhanced diffusive relaxation toward the effective equilibrium characterized by T_{eff}, leading to a homogeneous network structure with modest local density fluctuations. The magnitude of density fluctuations and the tenseness of the network depend on the susceptibility. At relatively low susceptibility ($s \leq 0.3$), homogeneously distributed spots of concentrated tense or floppy filaments are visible (Fig. 4.2b); as the susceptibility rises ($s \sim 0.5$), density fluctuations get weaker and the network becomes more homogeneous with a lower degree of stretching, closely resembling the flowing state (Fig. 4.2c). At relatively high connectivity the simulations thus verify the possible dynamic phases predicted by the analytical theory.

At intermediate connectivity $P_c \simeq 0.3$ ($z \simeq 3$–4) network connectivity is sufficient for tension percolation yet local force asymmetry becomes significant and widespread over the network. Now under susceptible motor kicks with a considerable step size, dramatic spatial heterogeneity emerges and oscillations of the network in a particular spontaneously chosen spatial direction occur (Fig. 4.3. Apparently the overall tenseness of the structure is reduced by collapsing the network into clumps at the cost of a few highly stretched inter-clump filaments. Figures 4.3c,d display the planar clumps where the floppy filaments (in green) concentrate and which are connected by highly stretched inter-clump bonds (in red). Our previous analytical mean-field study of an equilibrium nonlinear-elastic network [30] already suggests the possibility of phase separation in this system at a finite effective temperature; the pressure exhibits a non-monotonic dependence on the node concentration leading to mechanical instability of homogeneous states. (Phase sep-

aration induced by contractile instability has also been predicted for active polar gels [13].) When confined by boundaries, such as the cell membrane, these oscillating clumps may become stationary wave patterns with a characteristic length scale of modulation, reminiscent of the mitotic spindles.

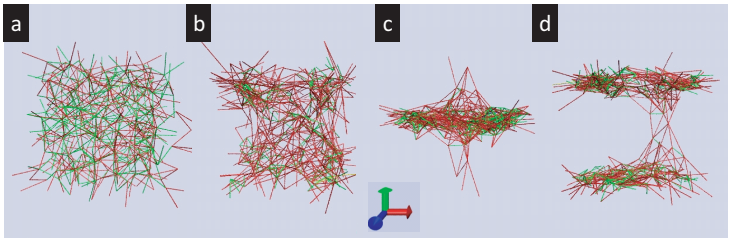

Figure 4.3: Temporal development of the phase separation. At intermediate connectivity $P_c = 0.3$ and under susceptible motor kicking ($s = 1$) with a considerable step size $l = 0.25$, the initially homogeneous system (a) phase separates into oscillating clumps and voids (b-d). Notice that the relaxed filaments (green) become concentrated within the planar clumps as well as the presence of highly stretched inter-clump filaments (red). $L_e = 1.2, \beta\gamma = 5$.

In the presence of susceptible motor kicking ($s \geq 0.6$), failure of force percolation at lower values of the network connectivity $P_c \leq 0.2\,(z < 3)$ also yields phase separation but without any collective motion. Conversely when there are too many bond constraints at $P_c \geq 0.6$ ($z > 7$) there are significant mechanical barriers which seem to slow down flow initiation and to reduce flow speed.

The analytic stability analysis leads to a similar connection between instability growth and the number of bond constraints via the localization strength of individual nodes. In Fig. 4.4 we display the two dimensional surface as well as the contour map of the growth rate r_k/k^2 given by Eq. 4.10 in the flowing regime ($r_k > 0$) as a function of localization strength α and kick size l for a series of susceptibilities s. Close to detailed balance, i.e., $s = 0.5$ (panel a), flowing instability emerges only at very high α and large l, and the growth rate increases with α. At $s = 0.55$ (b), a plateau in the growth rate develops at relatively high α. For susceptible motors with $s \geq 0.6$ (c and d), the growth rate has a non-monotonic dependence on α. As the localization strength of individual constituents increases, the flow instability first speeds up and then slows down with α. There exists an optimal localization strength (or network connectivity) for most efficient flow. This

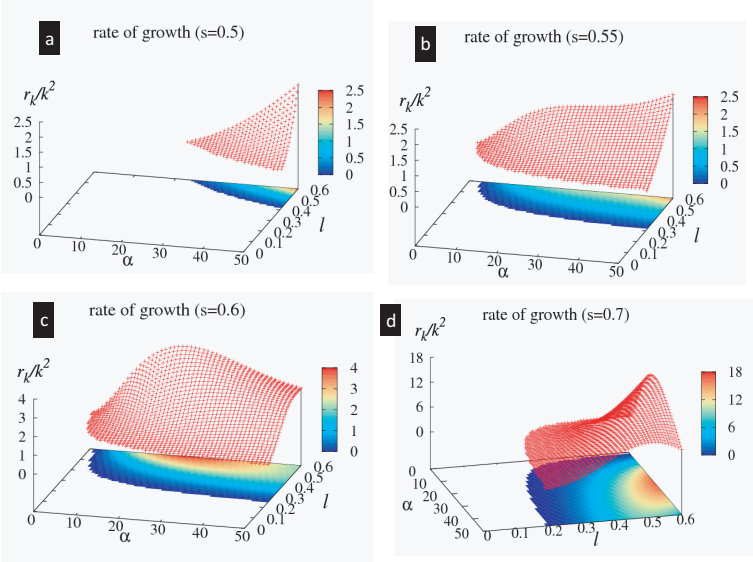

Figure 4.4: Dependence of growth rate upon localization strength at different motor susceptibility. The 2D surface and the contour map of the growth rate r_k/k^2 for flowing instability are displayed over the parameter plane extended by the localization strength α of individual particles and the motor kick step size l. $D_0 = 0.1$ and $\kappa = 20$. (a) $s = 0.5$; (b) $s = 0.55$; (c) $s = 0.6$; (d) $s = 0.7$. For susceptible motors with $s \geq 0.6$, the growth rate develops a non-monotonic dependence on the localization strength at a sufficiently large kick size, suggesting an optimal strength of mechanical feedback for an efficient flowing motion.

is consistent with simulations.

Biological motors can have slip bonds [33, 34] so that an applied force lowers the energy barrier for up-hill moves. Slip-bond behavior leads to a negative motor susceptibility which in turn leads to a negative effective temperature. This implies an intrinsic thermodynamic instability. We investigated this thermodynamically unusual situation. We consider the case for $s_u = -1, s_d = 0$ where motors are insensitive to energetically downhill slope while they run faster when they go up against obstacles. Starting with a disordered structure at a high connectivity ($P_c = 0.5$), the motorized network rapidly develops into a highly ordered and tense structure as shown in Fig. 4.5.

This interesting behavior is not hard to understand: due to the negative s_u, consistent with the negative effective temperature, the kicks maximize the total energy by separating the bonded nodes as far as possible from each other. The

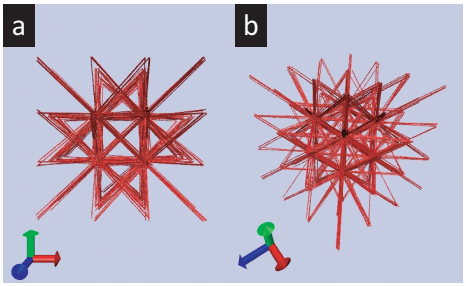

Figure 4.5: Aster-like patterns/Bundle-connected poles formed under kicks of uphill-prone motors with a negative susceptibility. $s_u = -1$, $s_d = 0$; $L_e = 1.2$, $\beta\gamma = 5$, $P_c = 0.5$, and $l = 0.25$. (a) and (b) are snapshots of the system taken at the same instant from different view angles.

resulting "aster-like" patterns closely resemble those formed by *in vitro* reconstituted active gels [35], where unidirectional movement of myosin II motors along the polar filament tracks toward the aster core (concentrated 'plus' ends of actin filaments) results in considerable stress accumulation at the center, giving rise to the so-called "novas of asters". Clearly motor susceptibility dramatically affects development of nonequilibrium structures.

In sum we have derived an analytical expression for the stability limits of quiescent active gels and proposed a mechanism for spontaneous collective motion within a unified theoretical framework. Simulations of a model cytoskeletal network further highlight that the interplay of network connectivity with motor susceptibility dramatically affects the formation of nonequilibrium structures: force percolation and mechano-chemical coupling conspire to drive and maintain spontaneous flow, whereas adamant motor kicks promote fluidization. Significant force imbalance sensed by susceptible motors induces phase separation into oscillating clumps. Uphill-prone motors with a negative susceptibility give rise to a system at a negative effective temperature. Aster-like patterns form resembling those seen in reconstituted active gels.

Chapter 4, in full, is a reprint of the material as it appears in the Proceedings of the National Academy of Sciences **108** 15184-15189 (2011), S. Wang and P. G. Wolynes. The dissertation/thesis author was the primary investigator and author of this paper.

Bibliography

[1] Pecreaux, J. *et al.* Spindle oscillations during asymmetric cell division require a threshold number of active cortical force generators. *Curr. Biol.* **16,** 2111–2122 (2006).

[2] Bray, D. *Cell Movements*, (Garland, New York, 2001).

[3] Martin, P., Bozovic, D., Choe, Y. & Hudspeth, A. J. Spontaneous oscillation by hair bundles of the bullfrog's sacculus. *J. Neurosci.* **23,** 4533–4548 (2003).

[4] Spemann, H. *Embryonic Development and Induction*, (Garland, New York, 1988).

[5] Wang, S. & Wolynes, P. G. Effective temperature and glassy dynamics of active matter. *J. Chem. Phys.* **135,** 051101 (2011).

[6] Cugliandolo, L. F., Kurchan, J. & Peliti, L. Energy flow, partial equilibration, and effective temperatures in systems with slow dynamics. *Phys. Rev. E* **55,** 3898–3914 (1997).

[7] Berthier, L. & Barrat, J. -L. Nonequilibrium dynamics and fluctuation-dissipation in a sheared fluid. *J. Chem. Phys.* **116,** 6228–6242 (2002).

[8] Kurchan, J. In and out of equilibrium. *Nature* **433,** 222–225 (2005).

[9] Onsager, L. Statistical hydrodynamics. *Nuovo Cimento* **6,** 279–287 (1949).

[10] Cantwell, B. J. Organized motion in turbulent flow. *Ann. Rev. Fluid Mech.* **13,** 457–515 (1981).

[11] Feng, H. & Wang, J. Correlation function, response function and effective temperature of gene networks. *Chem. Phys. Lett.* **510,** 267–272 (2011).

[12] Jülicher, F. & Prost, J. Cooperative molecular motors. *Phys. Rev. Lett.* **75,** 2618 (1995).

[13] Voituriez, R., Joanny, J. F. & Prost, J. Generic phase diagram of active polar films. *Phys. Rev. Lett.* **96,** 028102 (2006).

[14] Voituriez, R., Joanny, J. F. & Prost, J. Spontaneous flow transition in active polar gels. *Europhys. Lett.* **70,** 404–410 (2005).

[15] Liverpool, T. B. & Marchetti, M. C. Instabilities of isotropic solutions of active polar filaments. *Phys. Rev. Lett.* **90,** 138102 (2003).

[16] Banerjee, S. & Marchetti, M. C. Instabilities and oscillations in isotropic active gels. *Soft Matter* **7,** 463–473 (2011).

[17] Bois, J. S., Jülicher, F. & Grill, S. W. Pattern formation in active fluids. *Phys. Rev. Lett.* **106,** 028103 (2011).

[18] Shen, T. & Wolynes, P. G. Stability and dynamics of crystals and glasses of motorized particles. *Proc. Natl. Acad. Sci. USA* **101,** 8547–8550 (2004).

[19] Shen, T. & Wolynes, P. G. Nonequilibrium statistical mechanical model for cytoskeletal assembly: Towards understanding tensegrity in cells. *Phys. Rev. E* **72,** 041927 (2005).

[20] Brangwynne, C. P., Koenderink, G. H., MacKintosh, F. C. & Weitz, D. A. Cytoplasmic diffusion: molecular motors mix it up. *J. Cell Biol.* **183,** 583–587 (2008).

[21] Mizuno, D., Tardin, C., Schmidt, C. F. & MacKintosh, F. C. Nonequilibrium mechanics of active cytoskeletal networks. *Science* **315,** 370–373 (2007).

[22] Ziebert, F. & Aranson, I. S. Rheological and structural properties of dilute active filament solutions. *Phys. Rev. E* **77,** 011918 (2008).

[23] Loi, D., Mossa, S. & Cugliandolo, L. F. Effective temperature of active complex matter. *Soft Matter* **7,** 3726–3729 (2011).

[24] Wang, J., Xu, L. & Wang, E. K. Potential landscape and flux framework of nonequilibrium networks: robustness, dissipation and coherence of biochemical oscillations. *Proc. Natl. Acad. Sci. USA* **105,** 12271–12276 (2008).

[25] Fixman, M. Highly anharmonic crystal. *J. Chem. Phys.* **51,** 3270–3279 (1969).

[26] Stoessel, J. P. & Wolynes, P. G. Linear excitations and the stability of the hard sphere glass. *J. Chem. Phys.* **80,** 4502–4512 (1984).

[27] Uyeda, T. Q. P., Kron, S. J. & Spudich, J. A. Myosin step size: estimation from slow sliding movement of actin over low densities of heavy meromyosin. *J. Mol. Biol.* **214,** 699–710 (1990).

[28] Salbreux, G., Prost, J. & Joanny, J. F. Hydrodynamics of cellular cortical flows and the formation of contractile rings. *Phys. Rev. Lett.* **103,** 058102 (2009).

[29] Shen, T. & Wolynes, P. G. Statistical mechanics of a cat's cradle. *New J. Phys.* **8,** 273 (2006).

[30] Wang, S., Shen, T. & Wolynes, P. G. The interplay of nonlinearity and architecture in equilibrium cytoskeletal mechanics. *J. Chem. Phys.* **134,** 014510 (2011).

[31] Gillespie, D. T. A General Method for Numerically Simulating the Stochastic Time Evolution of Coupled Chemical Reactions. *J. Comp. Phys.* **22,** 403–434 (1976).

[32] Ermak, D. L. & McCammon, J. A. Brownian dynamics with hydrodynamic interactions. *J. Chem. Phys.* **69,** 1352–1360 (1978).

[33] Alon, R., Hammer, D. A. & Springer, T. A. Lifetime of the P-selectin-carbohydrate bond and its response to tensile force in hydrodynamic flow. *Nature* **374,** 539–542 (1995).

[34] Dudko, O. K., Hummer, G. & Szabo, A. Intrinsic rates and activation free energies from single-molecule pulling experiments. *Phys. Rev. Lett.* **96,** 108101 (2006).

[35] Backouche, F., Haviv, L., Groswasser, D. & Bernheim-Groswasser, A. Active gels: dynamics of patterning and self-organization. *Phys. Biol.* **3,** 264–273 (2006).

Supplementary figures

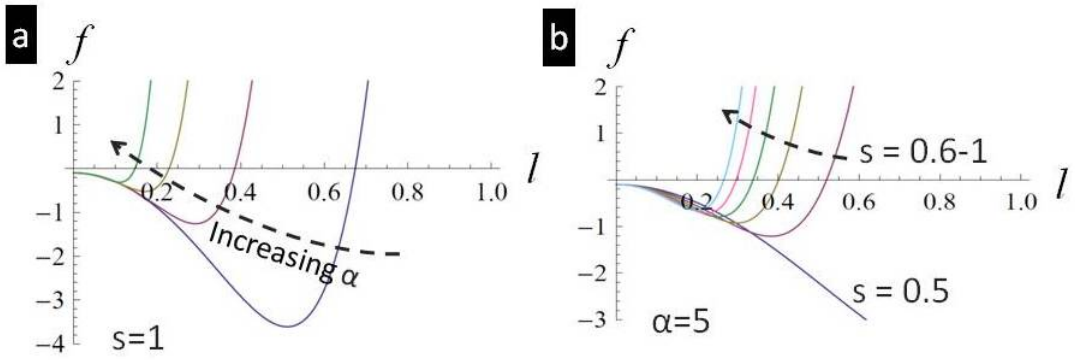

Figure 4.6: Dependence of threshold kick step size upon mechanical gradient α and motor susceptibility s. We plot $f(l, s; \alpha, \tilde{\alpha})$ given by equation (11) in the main text as a function of kick step size l for $\kappa = 20, D_0 = 0.1$. The crossing point of f-curve with l-axis locates l_{th}. (a) From right to left, $\alpha = 0.1, 1, 10$ and 100; $s = 1$. l_{th} decreases with increasing α value (dashed arrow), indicating that strong mechanical feedback facilitates instability onset. (b) For a moderate α value ($\alpha = 5$), no instability onset occurs for $s \leq 0.5$; only after s reaches approximately 0.6 does an instability emerge and increasing s (dashed arrow) leads to lower l_{th}. Meanwhile, for a given l, f increases with s, suggesting that more susceptible motors drive faster flows.

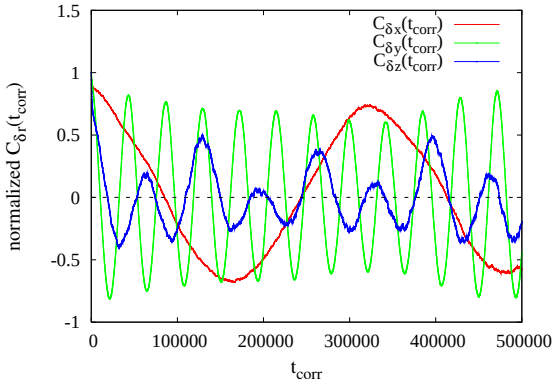

Figure 4.7: Statistical characteristics for the flowing state. We plot the ensemble-averaged temporal correlation of displacement fluctuations defined via the correlation function $C_{\delta\vec{r}}(t_{\rm corr}) = \frac{1}{t_f - t_0}\int_{t_0}^{t_f} d\tau [\frac{1}{N}\sum_{i=1}^{N}\delta\vec{r}_i(\tau)][\frac{1}{N}\sum_{j=1}^{N}\delta\vec{r}_j(\tau + t_{\rm corr})]$, where $\delta\vec{r}_i(t) = \vec{r}_i(t) - \langle\vec{r}_i(t)\rangle$ with the bracket indicating an average over a steady-state time window. The integral averages the starting time τ over a wide time range (t_0, t_f). Correlations in three orthogonal spatial directions (x: red; y: green; z: blue) all exhibit periodic oscillations in time (in Monte Carlo units) reflecting the spontaneous and coherent flowing motion across the periodic simulation box. Other correlation measures exhibit consistent oscillatory patterns. $L_e = 1.2$, $\beta\gamma = 5$, $P_c = 0.5$; $l = 0.25, s = 1$.

Chapter 5

Active contractility in actomyosin networks

5.1 Introduction

Contractile forces are essential for many processes vital to development, ranging from cytokinesis and cell motility [1] to wound healing and gastrulation [2]. Networks of filamentous actin (F-actin) and the molecular motor, type II myosin have been identified as the major components of the contractile machinery. The actin network provides a structural scaffold on which the myosin motors move, powered by ATP hydrolysis. Actomyosin networks generate contractile forces through the activity of myosin motors, which themselves assemble into bipolar minifilaments that generate sustained sliding of neighboring actin filaments relative to each other in order to reorganize F-actin networks and generate tension [3]. When coupled to the cell substrate or using cell-cell adhesions, contractile actomyosin networks transmit forces to their environment.

In addition to the microtubule-kinesin system, another important filament-motor assembly in cells that forms well-focused mitotic spindle poles driven by polarity sorting mechanism [4, 5] to accomplish high-accuracy segregation of duplicated chromosomes, actomyosin condensates appear in diverse tissues and organisms as transient structures that coalesce into still larger arrays that exert

contractile forces. Examples include the contractile rings driving cytokinesis and wound healing, and the contractile networks that deform epithelial cell layers in developing embryos and drive polarizing cortical flows [6, 7].

Some recent theoretical efforts have modeled the contractile actin cortex as an active polar gel and have derived effective continuum theories within a hydrodynamic framework [8, 9, 10, 11, 12, 13]. These macroscopic approaches based on generic symmetry considerations predict the formation of diverse patterns in acto-myosin gels such as asters and ring-like structures, which have been observed in studies *in vitro* [14].

Recently Bendix and coworkers have reconstituted contractility in a simplified system of F-actin, muscle myosin II motors, and α-actinin crosslinks [15]. The well-controlled nature of this in vitro system allows a systematic study of the dependence of contractility on *microscopic* parameters, such as the number and activity of myosin motors, crosslink density and actin network connectivity. It has been shown that contractility occurs above a threshold motor concentration and within a *window* of crosslink concentrations. Whereas earlier experiments on purified actomyosin solutions have established that contraction of F-actin networks by myosin II motors at physiological ATP level requires the presence of F-actin crosslinks [16, 17], as has been confirmed by recent theoretical work [18], this newly observed non-monotonic dependence of contraction tendency on crosslinking strength still calls for explanation.

There are two important aspects in actomyosin self-organization: (1) Actin filaments have a highly asymmetric response to axial loading: They strongly resist tensile forces but easily buckle under compressive loads of several piconewtons. The ability to sustain large tension allows the motor-induced stresses to propagate significant distances through the network, whereas the buckling instability promotes formation of local actomyosin aggregates that coalesce into larger arrays exerting contractile forces (as exemplified in the spontaneous formation of myosin foci starting from a uniform distribution in an isotropic actin network [19, 20]). (2) Motor-induced movements come in correlated pairs: the motor acts on a pair of parallel filaments to slide them past one another, inducing a pair of equal and

oppositely directed moves at the crosslinks which are thus pulled together. Despite the success of hydrodynamic theories in predicting diverse patterns, a more microscopic model that could capture the nonlinear buckling behavior and the correlated motor-driven events, both of which are crucial for actomyosin self-organization and active contractility, is needed.

Here we provide a microscopic dynamic model for active contractility that combines the motor-driven stochastic processes (modeled as correlated kicks on motor-bonded crosslinks) with the asymmetric load response of individual actin filaments. This minimal model will be shown to exhibit the experimentally observed dependence of macroscopic contraction on motor concentration and actin network connectivity. The model also highlights the key role, in structural development, of motor susceptibility, a parameter characterizing how sensitively the motors respond to imposed forces.

By performing dynamic Monte Carlo simulations, we investigate the formation and dynamics of nonequilibrium structures in an actomyosin network modeled as a "cat's cradle" [21, 22] consisting of crosslinked nonlinear-elastic filaments subject to anti-correlated kicks on motor-bonded crosslinks (see Fig. 5.1 for a schematic illustration). We first study how the concentration and susceptibility of motors determine the collective behavior generating diverse patterns. We further construct a phase diagram for active contractility as a function of motor concentration and network connectivity at a given motor susceptibility. This diagram identifies the threshold motor concentrations and contains a window of network connectivity for active macroscopic contraction, consistent with observation [15]. We also find that at high connectivity contraction can still occur (at intermediate motor concentrations) but only if the excluded volume effect is negligibly small. We finally compare the structures that develop for systems with correlated kicks to those when there are only uncorrelated kicks as in our earlier work [23]. In particular, under uphill-prone motor kicks, the formation of "asters" is replaced by the formation of disordered condensates resulting from an active multistage aggregation process due to buckling of connected actin structures induced by cooperative anti-correlated kicks. This prediction receives support from recent in vitro experimental

studies on how the collective action of myosin motors organizes actin filaments into contractile structures [20].

Multiple factors that cause dynamic remodeling in cells are clearly absent in the reconstituted assay [15], such as the disassembly of contractile structures and the transience of physiological actin cross-linking proteins. In our numerical model, we likewise assume that network connectivity and motor distribution are quenched once initially assigned, in line with the fact that *in vitro* structures are irreversibly assembled because many *in vivo* factors allowing fast pattern renewals are left out. Therefore the nonequilibrium dynamics and structures exhibited in our numerical study arise solely from the intrinsic activity of motors firmly built into the actin network driving correlated movements stochastically. This contrasts with the two-fluid model that treats the cytoskeletal network as an elastic continuum where motor (un)binding kinetics leads to enhanced low-frequency stress fluctuations [10]. The discreteness of the power strokes and thus the kick steps in our model bears relevance to the pulsed contraction observed in actomyosin networks *in vivo* [24].

5.2 Model

5.2.1 Model system and dynamic rule

We model the actomyosin network as a cat's cradle [21, 22] consisting of nonlinear elastic filaments built on a three dimensional random lattice of volumeless crosslinks (Fig. 5.1). These nonlinear filaments stretch elastically with effective stiffness $\beta\gamma$ when their contour length r exceeds the relaxed length L_e but buckle and become floppy upon shortening, as described by the pair interaction potential between bonded neighboring crosslinks $\beta U(r) = \Theta(r - L_e)\beta\gamma(r - L_e)^2/2$ where $\beta = 1/k_BT$ and $\Theta(\cdot)$ is the Heaviside step function. The assumed weakness of the excluded volume effect allows large-scale structural rearrangements. We assign two mean field parameters to characterize the architecture of this filament-motor assembly: (1) the network connectivity, P_c, which denotes the fraction of nearest-neighbor pairs of crosslinks bonded by filaments; (2) the motor concentration,

P_a, which indicates the fraction of active bonds, i.e. those attached by motors which induce equal and oppositely directed kicks on the connected crosslink pair. Network connectivity and motor concentration determine the fraction of active nodes against passive nodes: active nodes have motor-attached bonds and are subject to anti-correlated kicks with their motor-bonded neighbors whereas passive nodes have no motor-attached bonds and only undergo Brownian motion.

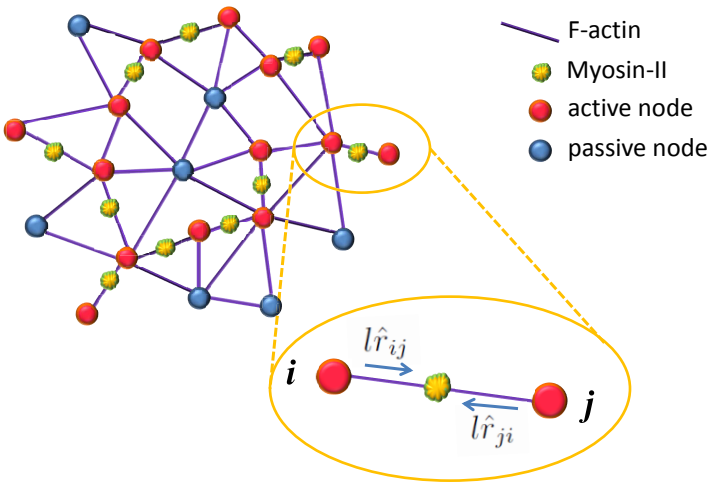

Figure 5.1: Schematic of the model system: A cat's cradle composed of a three dimensional amorphous network of crosslinked nonlinear-elastic bonds (purple lines) where motor-driven anti-correlated kicks induce pulsed local bond contraction and node aggregation. Spheres represent nodes/crosslinks and the yellow fuzzy objects stand for myosin II motor proteins. The size of the nodes and motors is exaggerated; excluded volume interaction is not implemented in current simulations. Red nodes are active nodes having motor-attached bonds. These are subject to motor kicks. Blue nodes are passive nodes only undergoing Brownian motion. An enlarged view of a unit of local contraction (circled) shows a pair of motor-bonded crosslinks undergoing anti-correlated kicks with fixed step size l along the line connecting their centers where $\hat{r}_{ij}$ is a unit vector pointing from node i to node j.

To mimic the motor-driven filament sliding in actomyosin networks we describe the motors as generating anti-correlated kicks on pairs of crosslinks along

their lines of centers. Assuming a fixed kick step size l, consistent with the nearly periodic structure of the actin filaments, an anti-correlated kick pair acting on nodes i and j can be represented by $(\vec{l}_{ij}, \vec{l}_{ji}) = l(\hat{r}_{ij}, -\hat{r}_{ij})$, where $\hat{r}_{ij}$ is a unit vector pointing from node i to node j. These anti-correlated kick pairs with equal size automatically satisfy momentum conservation on the macroscopic scale. Yet if we include explicitly the aqueous environment in which the actomyosin network is immersed, hydrodynamic interactions between the nodes via the solvent should be taken into account. These interactions might modify the current simplified picture and counteract any motor-induced force imbalance on individual nodes, thus validating momentum conservation on the microscopic scale.

Dynamical evolution of the many-particle configuration $\{\vec{r}_i\}$ due to these motor-driven nonequilibrium processes can be described by a master equation $\partial\Psi/\partial t = \hat{L}_{\rm NE}\Psi$ for the configurational probability density $\Psi(\{\vec{r}_i\}; t)$ with $\hat{L}_{\rm NE}\Psi(\{\vec{r}\}, t) = \int \Pi_i d\vec{r}'_i [K(\{\vec{r}'\} \to \{\vec{r}\})\Psi(\{\vec{r}'\}, t) - K(\{\vec{r}\} \to \{\vec{r}'\})\Psi(\{\vec{r}\}, t)]$ where the integral kernel $K(\{\vec{r}'_i\} \to \{\vec{r}_i\})$ encodes the probability of transitions between different crosslink/node configurations. Our earlier description [23, 25] of the motor kicking rate, k, still applies to the current case of correlated kicks, i.e.,

$$k = \kappa[\Theta(\Delta U)\exp(-s_u\beta\Delta U) + \Theta(-\Delta U)\exp(-s_d\beta\Delta U)], \tag{5.1}$$

where κ is the basal kicking rate and $s_u(s_d)$ denotes motor susceptibility to energetically uphill (downhill) moves, except that the free energy change ΔU now arises from *pairs* of displacements. Explicitly we write

$$\begin{aligned}
\hat{L}_{\rm NE}\Psi(\{\vec{r}_i\}; t) &= \frac{1}{2}\kappa \sum_i \sum_j C_{ij} \int d\vec{r}'_i \int d\vec{r}'_j \\
&\times \Big\{\delta(\vec{r}_i - \vec{r}'_i - \vec{l}_{ij})\delta(\vec{r}_j - \vec{r}'_j + \vec{l}_{ij}) \\
&\times w\Big[U(\cdots, \vec{r}'_i, \cdots, \vec{r}'_j, \cdots) - U(\cdots, \vec{r}_i, \cdots, \vec{r}_j, \cdots)\Big]\Psi(\{\vec{r}'_i\}; t) \\
&- \delta(\vec{r}_i - \vec{r}'_i + \vec{l}_{ij})\delta(\vec{r}_j - \vec{r}'_j - \vec{l}_{ij}) \\
&\times w\Big[U(\cdots, \vec{r}_i, \cdots, \vec{r}_j, \cdots) - U(\cdots, \vec{r}'_i, \cdots, \vec{r}'_j, \cdots)\Big]\Psi(\{\vec{r}_i\}; t)\Big\}.
\end{aligned}$$

The factor $1/2$ avoids double counting in the summation over all pairs. The quantity C_{ij}, much like an element of a contact map in description of protein structures,

defines whether the node pair (i, j) is connected by an active bond and thus subject to anti-correlated displacements $(\vec{l}_{ij}, -\vec{l}_{ij})$: $C_{ij} = C_{ji} = 1$ for motor-bonded pairs while $C_{ij} = C_{ji} = 0$ for non-bonded pairs. Our description of the rates gives $w[U_i - U_f] = \Theta(U_f - U_i) \exp[-s_u\beta(U_f - U_i)] + \Theta(U_i - U_f) \exp[-s_d\beta(U_f - U_i)]$.

Assuming symmetric motor susceptibility, i.e. $s_u = s_d = s$, one finds more simply

$$\hat{L}_{\text{NE}}\Psi(\{\vec{r}_i\}; t) = \frac{1}{2}\kappa \sum_i \sum_j C_{ij}$$
$$\times\Big\{e^{-s\beta\left[U(\vec{r}_i,\vec{r}_j)-U(\vec{r}_i-\vec{l}_{ij},\vec{r}_j+\vec{l}_{ij})\right]}\Psi(\{\cdots, \vec{r'}_i = \vec{r}_i - \vec{l}_{ij}, \cdots, \vec{r'}_j = \vec{r}_j + \vec{l}_{ij}, \cdots\}; t)$$
$$-e^{-s\beta\left[U(\vec{r}_i+\vec{l}_{ij},\vec{r}_j-\vec{l}_{ij})-U(\vec{r}_i,\vec{r}_j)\right]}\Psi(\{\cdots, \vec{r}_i, \cdots, \vec{r}_j, \cdots\}; t)\Big\}. \tag{5.2}$$

We assume that kicks on different node pairs at any time are uncorrelated. The rates of possible kicking events depend on the *instantaneous* node configuration reflecting an assumed Markovian character of the dynamics. There is no angular average due to the definiteness of kicking directions for a given configuration.

Note that the motor power strokes and thus kick steps are discrete occurring in a stochastic fashion. The correlated motions pull in slack locally while pulling taut neighboring filaments until a global balance is reached or a macroscopic collapse occurs, depending on whether the motors are downhill-prone (with a large positive s) or load-resisting (with a small or negative s), respectively. The latter may be relevant to the contractile rachet-like behavior [24] that operates to *incrementally* drive cell shape change and deform tissues.

5.2.2 Numerical translation: dynamic Monte Carlo simulation

To realize the finite-jump Markov process described by the (chemical) master equation (Eq. 6.6) we performed dynamic Monte Carlo [26] simulations on the model actomyosin network (Fig. 5.1). In these simulations we generated initially a three-dimensional random lattice of volumeless nodes (mimicking the crosslinking proteins) and connected the nearest-neighbor nodes (defined by the first shell of the pair distribution function) with nonlinear elastic bonds [22] (mimicking the

actin filaments) at a given probability P_c. We then distributed the myosin motors uniformly to the bonds at a given probability P_a and obtained an active bond map. Considering the anti-correlated kicks along individual active bonds as chemical reaction channels, we adopted a stochastic simulation algorithm [26] to execute the moves following the stochastic process defined by the model motor kicking noise (Eq. 5.1). For a sufficiently large system, kicking events on different node pairs are effectively decoupled (consistent with summing over independent reaction channels in the master equation). Intermediate thermal moves between successive chemical moves obey Brownian dynamics [27] implemented via the position Langevin equation.

The bond properties are given by the elasticity onset or relaxed length of actin filaments $L_e = 1.2$ and the effective stretch modulus $\beta\gamma = 2$. Since the relaxed length is larger than the mean node separation (set as the length unit), the initial homogeneous (but amorphous) network has a considerable fraction of floppy bonds. We assumed a relatively high basal kicking rate ($\kappa = 0.01$) and a large kick step size ($l = 0.2$) such that the dimensionless motor activity (defined as $\kappa l^2/D_0$ where D_0 is the thermal diffusion constant) is close to 1 and thus the strength of chemical noise is at least comparable to that of the thermal noise. The system size is $N = 256$ and periodic boundary conditions are applied. The relevant biophysical parameters to vary include network connectivity (P_c) as well as motor concentration (P_a) and susceptibility (s).

5.3 Main Findings

5.3.1 Role of motor susceptibility and concentration in contractile behavior

We first study how the concentration (P_a) and susceptibility (s) of motors contribute to the collective behavior. As illustrated in Fig. 5.2, depending on the specific combinations of P_a and s, distinct nonequilibrium structures emerge. For a force-percolating network (i.e. one with connectivity beyond the perco-

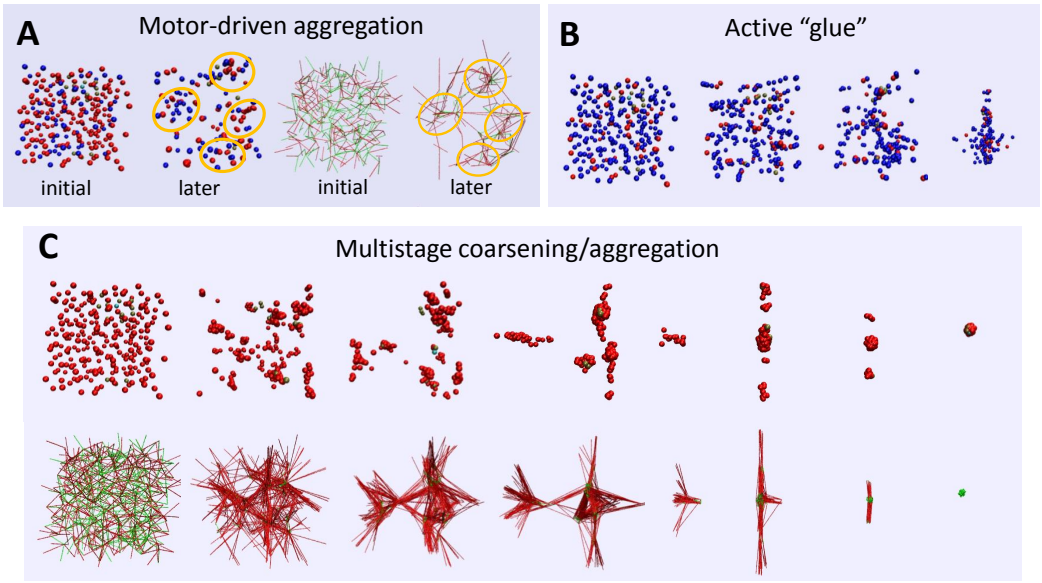

Figure 5.2: Illustration of how motor concentration P_a and susceptibility s contribute to their collective behavior. (a) Left: motor-driven aggregation of active nodes (red spheres) among the passive nodes (blue spheres); right: formation of dense floppy clumps (concentrated short green lines) inter-connected by tense bonds (long red lines). Circles mark the corresponding regions of node aggregation and bond collapse. $P_c = 0.2, P_a = 0.5, s = 1$. (b) Active nodes tend to "glue" together passive nodes and their aggregates. $P_c = 0.5, P_a = 0.2, s = 0$. (c) Multistage coarsening/aggregation of active condensates driven by high-concentration ($P_a = 1$) uphill-prone ($s = -0.5$) motors. $P_c = 0.5$. Shown are the temporal evolution of the node configuration (upper row) and of the corresponding network structure (lower row).

lation threshold) when partially motorized ($P_a < 1$) under susceptible (large s) anti-correlated kicks, the active nodes (those with motor-attached bonds; shown as red spheres) begin to aggregate and tend to separate from the passive nodes (those with no active bonds; shown as blue spheres). The left panel of Fig. 5.2a shows snapshots of both the initial and later node configurations. The corresponding developed network structure (Fig. 5.2a right) exhibits clumps of floppy bonds (concentrated short green lines) connected by tense bonds (long red lines). The overall rigidity (i.e. homogeneity on large scales) of the structure is protected by susceptible motors which tune the balance between local bond contraction and neighboring bond stretching such that energetically unfavorable tense states are

avoided. At a low concentration of adamant motors (small s), however, active nodes and their aggregates tend to "glue" together progressively the passive nodes and their condensates (Fig. 5.2b). A finite spatial extent of the condensate and a non-vanishing fraction of taut bonds remain due to the insufficient cooperativity (low P_a) between local aggregation events. More dramatically, significant spatial heterogeneity forms when the system is driven by a large number of uphill-prone motors with negative susceptibility: the cooperative action of load-resisting motors induces a multistage aggregation and coarsening of the nodes (Fig. 5.2c upper row) finally leading to a macroscopic contraction of an initially homogeneous network into a dense clump of buckled filaments (Fig. 5.2c lower row). This multistage coarsening process involves three steps: (1) local bond contraction and node aggregation giving floppy clumps connected by tense filaments; (2) coarsening of the aggregates leading to filament alignment and formation of tense bundles; (3) coalescence of the larger aggregates into a single condensate accompanies collapse of the tense bundles into a floppy clump. The aligned tense bundles formed before the eventual collapse constitute a taut state that can generate contractile forces.

We will investigate the scenario of motor-driven aggregation and pursue its analogy to arrested phase separation later. In the present work we will focus on the regime for macroscopic contraction.

To identify the required motor properties for active contractility, we performed many simulations to obtain the evolution (in Monte Carlo time t_{MC}) of the statistical characteristics for a series of motor susceptibilities (Fig. 5.5a) and concentrations (Fig. 5.5b). These measures consistently indicate the existence of a threshold motor concentration ($(P_a)_{\mathrm{th}}$) and a threshold susceptibility (s_{th}) for the onset of macroscopic contraction within the simulation time window. When s is less than s_{th} at an intermediate P_a value (Fig. 5.5a: $s \leq 0.02, P_a = 0.5$) or for $P_a > (P_a)_{\mathrm{th}}$ at a small s value (Fig. 5.5b: $P_a \geq 0.3, s = 0$), the fraction of taut bonds drops to essentially zero, indicating that an initially homogeneous percolating network collapses into a floppy clump. More interestingly, the total energy first rapidly rises and reaches a maximum before falling to zero with the fraction of taut bonds. This nonmonotonic behavior suggests that the system first works

against an energy barrier due to the formation of a *transient* tense state (having highly stretched bundles induced by adamant or uphill-prone motor kicks), and then cooperative action of sufficiently load-resisting motors drives the system over the barrier to allow energetically downhill moves via subsequent coarsening (as shown in Fig. 5.2c). The rapid increase and saturation of the mean squared displacement (MSD) mirrors the evolution of the fraction of taut bonds and results from the formation of a single isolated floppy clump. Larger s and/or higher P_a yields a lower barrier to the collapsed state (as indicated by arrows in Fig. 5.5). Moreover, lower P_a necessitates having a smaller s to induce macroscopic contraction. In other words, weaker motor cooperativity requires a stronger load-resisting tendency to trigger contractile instability. When $P_a < (P_a)_{\rm th}$ and/or $s > s_{\rm th}$ the structure remains homogeneous except for modest *local* node aggregation and network deformation.

5.3.2 State diagram for active contractility: Interplay of network connectivity and motor cooperativity

We now examine the interplay of network connectivity (P_c) and motor concentration (P_a) in forming contractile structures. The equivalence between the crosslink concentration and the fraction of bonded neighboring crosslinks P_c (both are proportional to the number of inter-crosslink segments and define the number of bond constraints), and between the motor concentration and the fraction of active bonds P_a (both are proportional to the number of crosslinks subject to motor kicks and determine the spatial cooperativity between motors) allows us to compare our state diagram constructed on the P_a-P_c plane with the experimental result [15] shown for the parameter space of concentration ratios [myosin]/[actin] versus [α-actinin]/[actin].

We present our state diagram showing the dependence of macroscopic contractility on the network connectivity and motor concentration at a small s value ($s = 0.01$) in Fig. 5.3. Red crosses denote contractile networks while blue circles denote non-contractile networks. By "contractile" we mean a complete collapse of an initially homogeneous network into a floppy clump within 10^7 MC steps, mon-

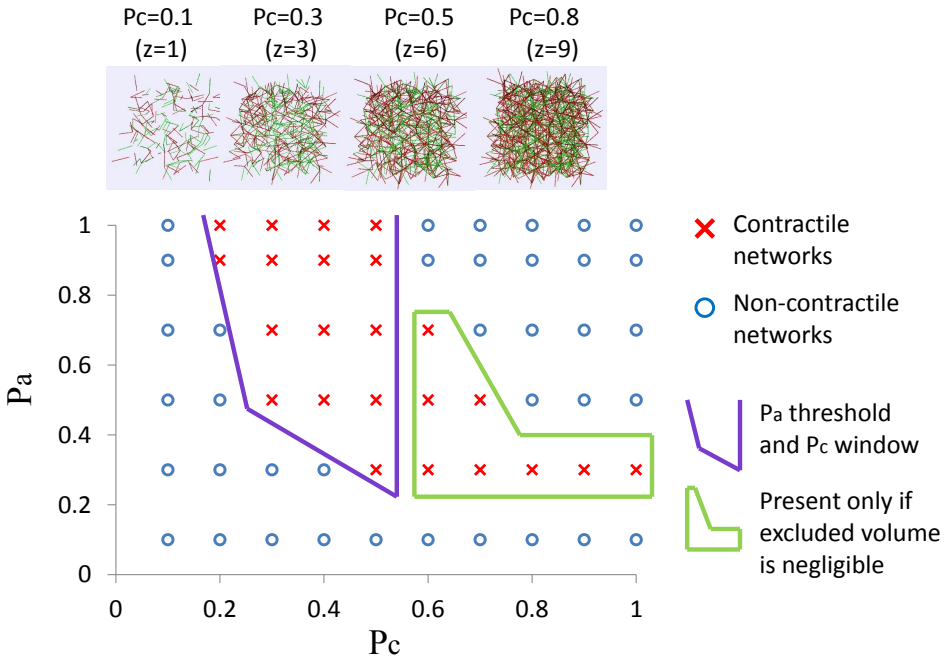

Figure 5.3: State diagram showing the dependence of active contractility on motor concentration P_a and network connectivity P_c. $s = 0.01$. Red crosses denote contractile networks and blue circles denote non-contractile networks. Top row displays the initial homogeneous network structures with increasing connectivity P_c and average number of bonded neighbors z. Macroscopic contraction occurs in the two framed regions: (1) purple open frame: intermediate P_c and above-threshold P_a; (2) green closed frame: high P_c and intermediate P_a.

itored by the vanishing of total potential energy and the fraction of taut bonds. On top of the figure, we display the initial network structures for several typical values of network connectivity P_c with the average number of bonded neighbors z. As observed experimentally [15], we identify a threshold motor concentration and a window of network connectivity for active contractility, which define a parameter region as marked by the purple open frame. The new feature is a small window of motor concentration for contraction at high connectivity (marked by a green closed frame). These two aspects vividly demonstrate the interplay of network connectivity and motor concentration for global contraction: at any connectivity beyond

the percolation threshold ($P_c \geq 0.2$), a sufficiently high motor concentration is required to achieve cooperativity among local contraction events; on the other hand, since the bond constraints are strong at high connectivity, motor concentration cannot be too high since force asymmetry (imbalanced tug-of-war) is necessary to trigger local contraction. In the *in vitro* experiments [15], no macroscopic contraction was observed on the hour time scale at high crosslink concentrations. This observation is not incompatible with our results since inclusion of excluded volume effects should give a dramatic slow-down of the contractile dynamics owing to jamming and/or glass transition which would account for the absence of observable contraction on laboratory time scales.

Outside the framed regions, at low motor concentration and/or low connectivity as well as at high motor concentration and high connectivity, there is no macroscopic contraction. We illustrate the failure of contractility at low connectivity (Fig. 5.6a) or low motor concentration (Fig. 5.5b). For P_c as low as 0.1, the average number of bonded neighbors is no greater than 1, lack of tension percolation thus prevents *global* contraction. This becomes more obvious as we increase the motor concentration; an increasing trend of *local* collapse with rising P_a value is apparent (Fig. 5.5a), leading to more compact aggregates and disconnected floppy clumps (several typical spots have been circled for the highest P_a case). At very low motor concentration $P_a = 0.1$ (Fig. 5.5b), formation of sparse and small active-node foci did not dramatically reshape the network, since rare and separate contraction events are insufficient to trigger global contractile instability.

A quantitative demonstration of the interplay between P_c and P_a is given in Fig. 5.7. Macroscopic contraction occurs either for high motor concentration (upper row, $P_a = 0.7$) at intermediate connectivity ($P_c = 0.3, 0.5$) or for high connectivity (lower row, $P_c = 0.7$) at intermediate motor concentrations ($P_a = 0.3, 0.5$). Lack of percolation at $P_c = 0.1$ is signalled by the diffusive behavior of the mean square node displacement MSD linearly increasing with t_{MC} (red line indicated by arrow in Fig. 5.7a right panel) since the disconnected aggregates merely undergo thermal motion. On the other hand, a small steady value for the MSD at $P_a = 0.1$ (red line indicated by arrow in Fig. 5.7b right panel) reflects the

low cooperativity which causes no more than modest local distortions. A balanced tug-of-war at high P_c and high P_a disfavors even local deformations yielding a lower fraction of taut bonds, lower energy and smaller MSD as P_a increases. This can be seen by comparing the measures for $P_a = 0.1$ and $P_a = 0.7$ at $P_c = 0.7$ in Fig. 5.7b.

5.3.3 Contrast with the case for uncorrelated kicks

Our earlier study of a model cytoskeleton with uncorrelated isotropic kicks acting on individual nodes [23] revealed that force percolation and mechanochemical coupling due to susceptible motors can conspire to maintain a spontaneous flow, whereas adamant motor kicks promote fluidization (characterized by a vanishing localization strength of the nodes and formation of a disordered tense network). Under anti-correlated kicks acting along the lines of centers of motor-bonded node pairs, however, no vectorial flow transition is found even for a very large kick step size ($l \simeq 0.5$). This is probably because the restrictiveness of (local) kicking directions for a given configuration impedes a global concerted *net* movement of the whole lattice. Instead, balanced local contraction and neighboring stretch in the presence of force percolation results in a network of floppy spots connected by tense filaments which remains homogeneous on large scales and bears some resemblance to arrested phase separation occurring in low-packing-fraction physical gels with strong short-range attractions [28]. At intermediate connectivity, force imbalance sensed by susceptible motors still induces phase separation into large floppy clumps connected by taut inter-clump bonds yet oscillations are no longer found. Fluidization is replaced by global contraction at above-threshold motor concentration.

When the uncorrelated-kicking system was driven by uphill-prone motors with negative susceptibility, aster-like patterns formed (Fig. 5.4 left). Instead, now, multistage coarsening and eventual macroscopic collapse occur (Fig. 5.4 right), after surmounting a high energy barrier caused by transient tense states with stretched bundles. Comparing the bond tension patterns for these two cases in Fig. 5.4, we see that global contraction requires *correlated* movements that locally

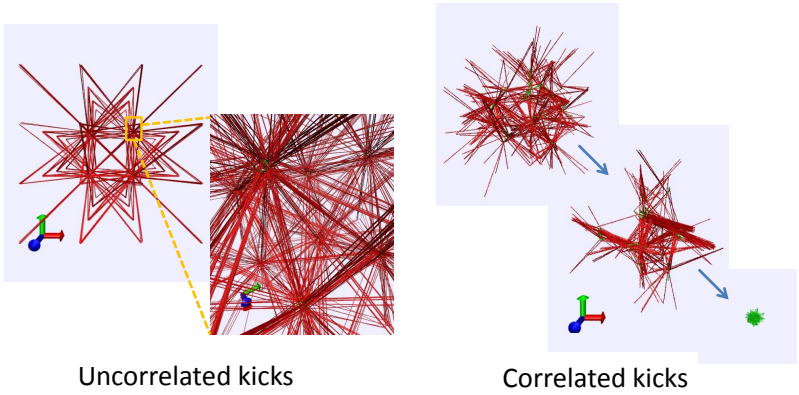

Figure 5.4: Aster versus condensate. $P_c = 0.5, P_a = 1, s = -0.5$. Left: Under uncorrelated kicks, an initially disordered and homogeneous network self-organizes into highly tense and ordered "asters", composed of tense bundles radiating from the junctions where floppy bonds concentrate (see the zoom-in image). Right: Driven by anti-correlated kicks, an initially homogeneous force-percolating network first develops transient tense states consisting of highly-stretched bundles, but then abruptly collapses into a single floppy clump.

buckle a filament yet impose strain on the bonds at *both* ends. Without this correlation the aster pattern cannot collapse. We display in Fig. 5.8 the snapshots in the course of aster formation which clearly demonstrate that node aggregation and coarsening leads to progressively more tight filament bundling and bundle alignment, a mechanism that operates for both the correlated- and uncorrelated-kick cases.

5.4 Conclusion and Discussion

We have simulated a microscopic model for the actomyosin cytoskeleton as a motorized cat's cradle that combines the asymmetric load response of individual actin filaments with correlated motor-driven events. This model reproduces the dependence of active contractility on microscopic parameters observed in reconstituted actomyosin networks. The simulations allow us to identify several necessary conditions for active contractility: highly asymmetric load responses of the filaments are needed for local contractile behavior under anti-correlated kicks, and

a minimal network structure beyond percolation threshold is required to propagate local contraction. Sufficiently cooperative load-resisting motors manage to drive the system through energy-costly intermediate states and incorporate local buckling events into macroscopic contraction via a multistage coarsening process.

This numerical study provides an explanation for the formation and contractile dynamics of disordered condensed state of actomyosin *in vivo*. The fact that such a simplified model is able to mimic cellular self-organization states and their contractile dynamics suggests that purely physical interactions contribute to the regulation of cell and tissue morphogenesis. Nevertheless specific biochemical signaling events [29] certainly contribute to the *localized* assembly and activation of myosin foci such as occurs in cleavage furrow during cytokinesis and in wound borders.

It is clearly necessary in the future to take into account the excluded volume effect which is expected to dramatically slow the contractile dynamics at high crosslink concentrations, thus accounting for the failure to see contractility on laboratory time scales. Long-range hydrodynamic interactions between the node pairs may also change the qualitative physics. Hydrodynamic correlations should facilitate propagation of nearby kicking events and break the continuous symmetry so as to allow spontaneous directed motion with motor-driven hydrodynamics-mediated pulsed contractions. Finally, in vivo one must incorporate motor attachment and detachment and crosslink binding and unbinding for complete realism.

Chapter 5, in full, is a reprint of the material as it appears in the Proceedings of the National Academy of Sciences **109** 6446-6451 (2012), S. Wang and P. G. Wolynes. The dissertation/thesis author was the primary investigator and author of this paper.

Bibliography

[1] Pollard, T. D. & Borisy, G. G. Cellular motility driven by assembly and disassembly of actin filaments. *Cell* **112,** 453–465 (2003).

[2] Holtfreter, J. A study of the mechanics of gastrulation (part 1). *J. Exp. Zool.* **94,** 261–318 (1943).

[3] Martin, A. C. Pulsation and stabilization: contractile forces that underlie morphogenesis. *Dev. Biol.* **341,** 114–125 (2010).

[4] Surrey, T., Nédélec, F., Leibler, S. & Karsenti, E. Physical properties determining self-organization of motors and microtubules. *Science* **292,** 1167–1171 (2001).

[5] Nédélec, F., Surrey, T., Maggs, A. C. & Leibler, S. Self-organization of microtubules and motors. *Nature* **389,** 305–308 (1997).

[6] Hird, S. & White, J. Cortical and cytoplasmic flow polarity in early embryonic cells of Caenorhabditis elegans. *J. Cell Biol.* **121,** 1343–1355 (1993).

[7] Mayer, M., Depken, M., Bois, J. S., Jülicher, F. & Grill, S. W. Anisotropies in cortical tension reveal the physical basis of polarizing cortical flows. *Nature* **467,** 617–621 (2010).

[8] Kruse, K., Joanny, J. F., Jülicher, F., Prost, J. & Sekimoto, K. Asters, vortices, and rotating spirals in active gels of polar filaments. *Phys. Rev. Lett.* **92,** 078101 (2004).

[9] Voituriez, R., Joanny, J. F. & Prost, J. Generic phase diagram of active polar films. *Phys. Rev. Lett.* **96,** 028102 (2006).

[10] MacKintosh, F. C. & Levine, A. J. Nonequilibrium mechanics and dynamics of motor-activated gels. *Phys. Rev. Lett.* **100,** 018104 (2008). Levine, A. J. & MacKintosh, F. C. The mechanics and fluctuation spectrum of active gels. *J. Phys. Chem. B* **113,** 3820–3830 (2009).

[11] Kruse, K. & Jülicher, F. Self-organization and mechanical properties of active filament bundles. *Phys. Rev. E Stat. Nonlin. Soft Matter Phys.* **67,** 051913 (2003).

[12] Lau, A., Hoffmann, B., Davies, A., Crocker, J. & Lubensky, T. Microrheology, stress fluctuations, and active behavior of living cells. *Phys. Rev. Lett.* **91,** 198101–198104 (2003).

[13] Liverpool, T. & Marchetti, M. Instabilities of isotropic solutions of active polar filaments. *Phys. Rev. Lett.* **90,** 138102 (2003).

[14] Backouche, F., Haviv, L., Groswasser, D. & Bernheim-Groswasser, A. Active gels: Dynamics of patterning and self-organization. *Phys. Biol.* **3,** 264–273 (2006).

[15] Bendix, P. M., Koenderink, G. H., Cuvelier, D., Dogic, Z., Koeleman, B. N., Briehera, W. M., Fielda, C. M., Mahadevan, L. & Weitz, D. A. A quantitative analysis of contractility in active cytoskeletal protein networks. *Biophys. J.* **94,** 3126–3136 (2008).

[16] Janson, L. W., Kolega, J. & Taylor, D. L. Modulation of contraction by gelation/solation in a reconstituted motile model. *J. Cell Biol.* **114,** 1005–1015 (1991).

[17] Kane, R. E. Interconversion of structural and contractile actin gels by insertion of myosin during assembly. *J. Cell Biol.* **97,** 1745–1752 (1983).

[18] Carlsson, A. E. Contractile stress generated by actomyosin gels. *Phys. Rev. E Stat. Nonlin. Soft Matter Phys.* **74,** 051912 (2006).

[19] Koenderink, G. H., Dogic, Z., Nakamura, F., Bendix, P. M., MacKintosh, F. C., Hartwig, J. H., Stossel, T. P. & Weitz, D. A. An active biopolymer network controlled by molecular motors. *Proc. Natl. Acad. Sci. USA* **106,** 15192–15197 (2009).

[20] Silva, M. S., Depken, M., Stuhrmann, B., Korsten, M., MacKintosh, F. C. & Koenderink, G. H. Active multistage coarsening of actin networks driven by myosin motors. *Proc. Natl. Acad. Sci. USA* **108,** 9408–9413 (2011).

[21] Shen, T. & Wolynes, P. G. Statistical mechanics of a cat's cradle. *New J. Phys.* **8,** 273 (2006).

[22] Wang, S., Shen, T. & Wolynes, P. G. The interplay of nonlinearity and architecture in equilibrium cytoskeletal mechanics. *J. Chem. Phys.* **134,** 014510 (2011).

[23] Wang, S. & Wolynes, P. G. On the spontaneous collective motion of active matter. *Proc. Natl. Acad. Sci. USA* **108,** 15184–15189 (2011).

[24] Martin, A. C., Kaschube, M. & Wieschaus, E. F. Pulsed contractions of an actin-myosin network drive apical constriction. *Nature* **457,** 495–499 (2009). Mason, F. M. & Martin, A. C. Tuning cell shape change with contractile ratchets. *Curr. Opin. Genet. Dev.* **21,** 671–679 (2011).

[25] Wang, S. & Wolynes, P. G. Effective temperature and glassy dynamics of active matter. *J. Chem. Phys.* **135,** 051101 (2011).

[26] Gillespie, D. T. A general method for numerically simulating the stochastic time evolution of coupled chemical reactions. *J. Comp. Phys.* **22,** 403–434 (1976).

[27] Ermak, D. L. & McCammon, J. A. Brownian dynamics with hydrodynamic interactions. *J. Chem. Phys.* **69,** 1352–1360 (1978).

[28] Zaccarelli, E. Colloidal gels: equilibrium and non-equilibrium routes. *J. Phys.: Condens. Matter* **19,** 323101 (2007).

[29] Tan, J. L., Ravid, S. & Spudich, J. A. Control of nonmuscle myosins by phosphorylation. *Annu. Rev. Biochem.* **61,** 721–759 (1992).

Supplementary figures

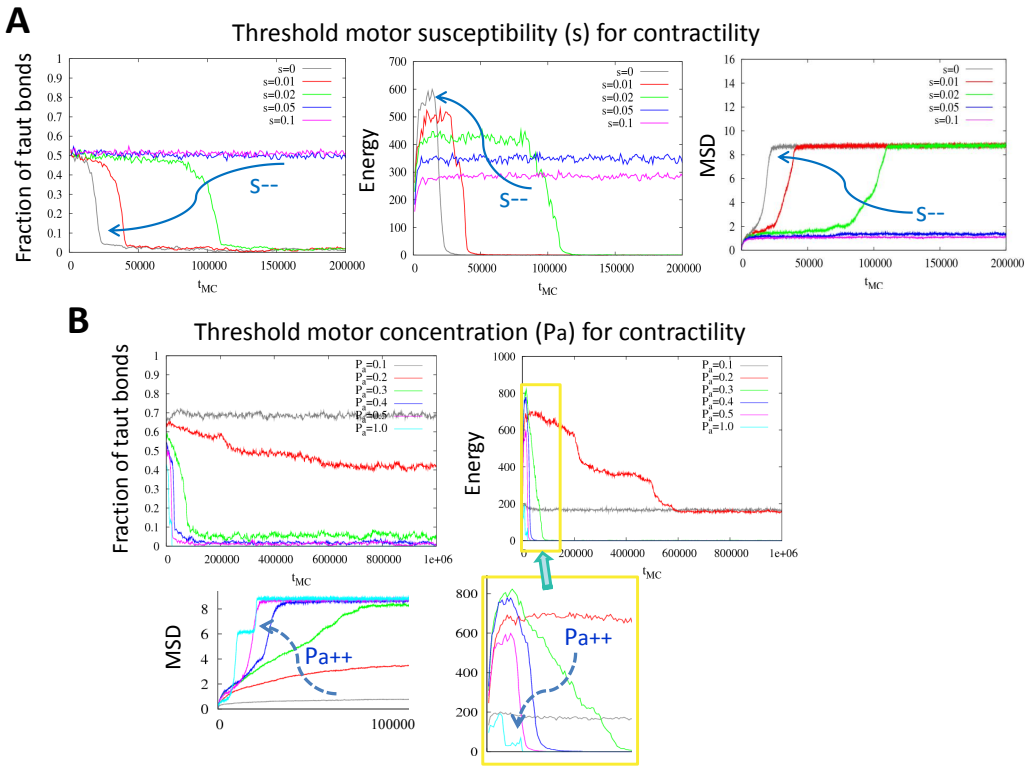

Figure 5.5: Thresholds for active contractility. (a) Evolution of the statistical measures for a series of motor susceptibilities ($s = 0, 0.01, 0.02, 0.05$ and 0.1). $P_c = 0.5, P_a = 0.5$. When $s \leq 0.02$ the fraction of taut bonds and the total energy drop to essentially zero after surmounting an energy barrier due to tense intermediates. Mean square displacement (MSD) mounts to a plateau as a consequence of the formation of a single floppy clump. Smaller s yields a higher barrier and faster collapse (indicated by arrows). (b) Evolution of the measures for a series of motor concentrations ($P_a = 0.1, 0.2, 0.3, 0.4, 0.5$ and 1). $P_c = 0.5, s = 0$. When $P_a \geq 0.3$ global contraction occurs. Larger P_a leads to lower barrier and faster collapse (indicated by arrows).

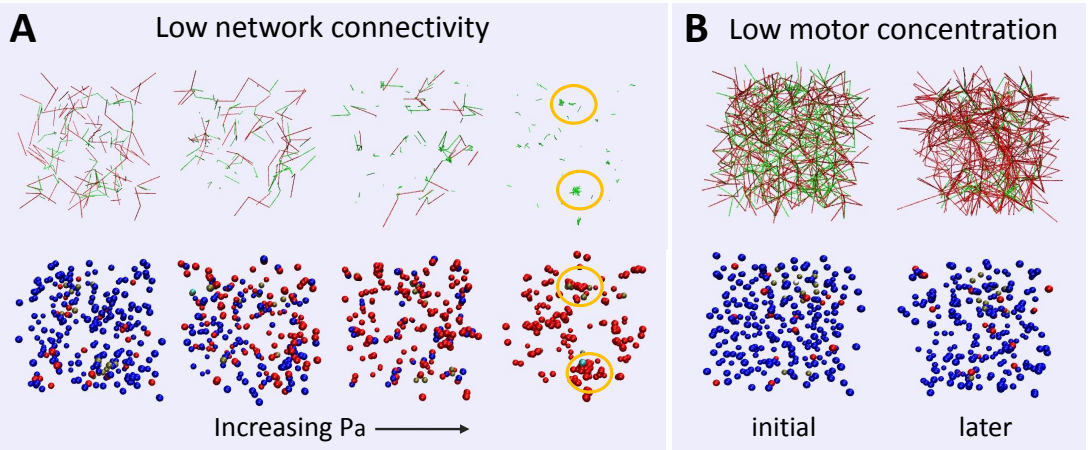

Figure 5.6: Illustrations of the failure of contractility at low network connectivity or low motor concentration. $s = 0$. (a) $P_c = 0.1$. Lack of tension percolation due to low degree of bonding prevents global contraction. As P_a increases (left to right: $P_a = 0.1, 0.5, 0.8$ and 1) system exhibits increasing trend of local aggregation (lower row) resulting in an increased fraction of floppy bonds (upper row). When driven by high-concentration ($P_a = 1$) adamant motors, the initially homogeneous network exhibits local collapses into disconnected clusters of buckled filaments (circles mark the typical regions). (b) $P_a = 0.1, P_c = 0.5$. Sparse and modest local network distortion (upper) and node aggregation (lower) are insufficient to trigger global contractile instability.

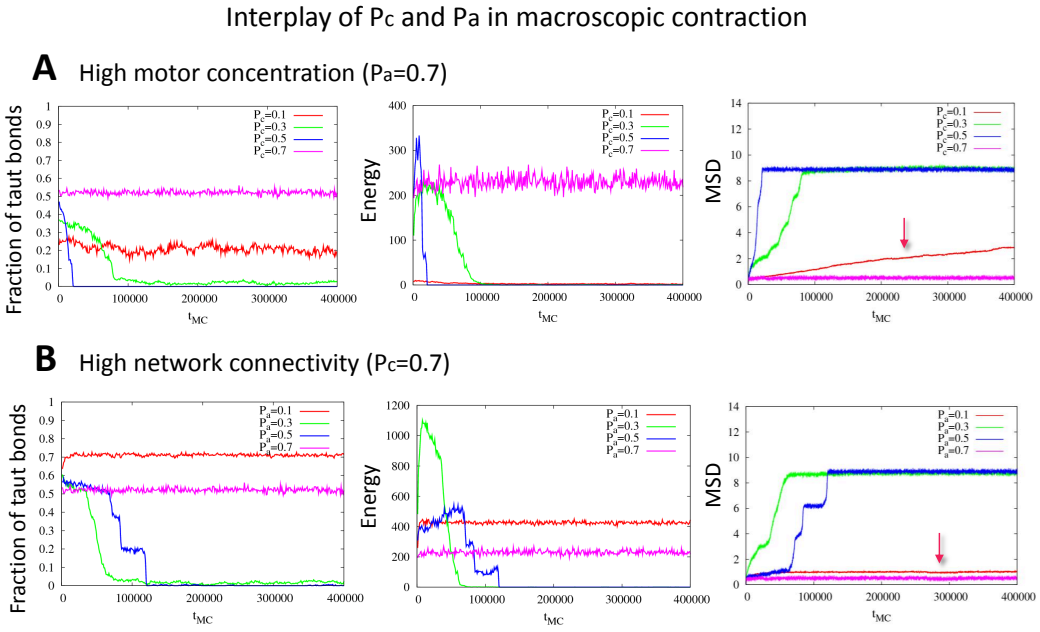

Figure 5.7: Interplay of network connectivity and motor concentration in macroscopic contraction. $s = 0.01$. (a) $P_a = 0.7$, $P_c = 0.1, 0.3, 0.5, 0.7$: contraction occurs for intermediate P_c. Larger P_c yields higher "barrier" to collapsed state since more bond constraints results in more intense tug-of-war. (b) $P_c = 0.7$, $P_a = 0.1, 0.3, 0.5, 0.7$: contraction occurs for intermediate P_a. Larger P_a lowers the barrier since cooperativity between local contraction events is enhanced.

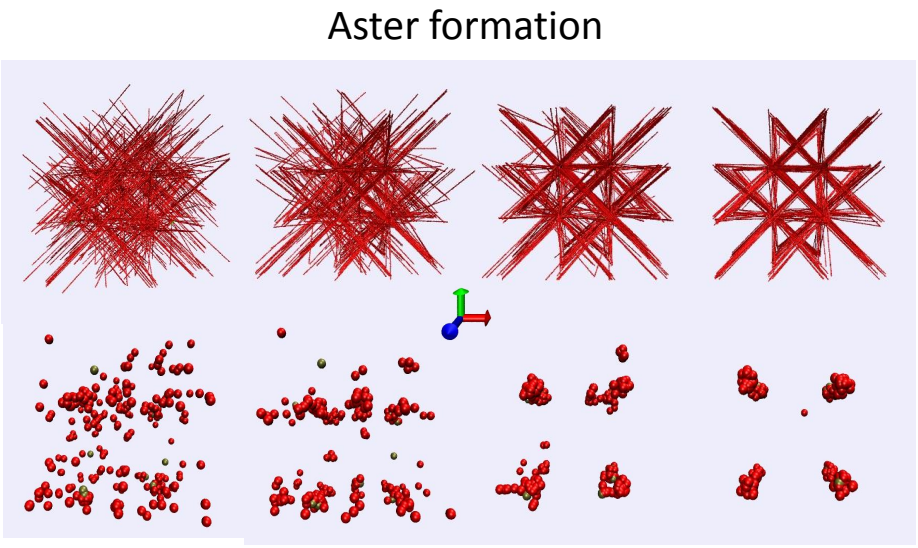

Figure 5.8: Snapshots in the course of aster formation. Upper row shows the bond structure: filament bundling evolves from loose to tight. Lower row presents the corresponding node configuration: aggregation toward the corners of the simulation box becomes progressively more compact. $P_c = 0.3, P_a = 1, s = -0.5$.

Chapter 6

Tensegrity and motor-driven effective interactions in a model cytoskeleton

6.1 Introduction

The mechanical integrity of eukaryotic cells depends on their cytoskeleton. The cytoskeleton is made up of a dense network of protein filaments spanning the cytoplasm. Cytoskeletal networks self-organize into highly dynamic and heterogeneous patterns from the interplay between active force generation by molecular motors and passive dissipation of energy in the crowded cellular interior [1]. Understanding the dynamics of such pattern formation remains a challenge to statistical mechanical theory.

Actomyosin networks are the main components of the cellular contractile machinery essential for processes as diverse as cytokinesis and wound healing. Walking on the structural scaffold provided by an actin network, myosin-II motors themselves self-assemble into bipolar minifilaments that generate sustained sliding of neighboring actin filaments relative to each other. By carrying out this correlated motion the minifilaments reorganize the filamentous actin networks and generate tension ultimately powered by ATP hydrolysis. The formation and coalescence

of actomyosin aggregates to exert contractile forces are manifested in pulsed contractions of an actomyosin network that drive epithelial sheet deformation during morphogenesis [2, 3]. Such aggregates also are responsible for a multistage coarsening process that occurs in a bottom-up model system for contractility which has been reconstituted in vitro [4].

In reconstituted filament-motor assemblies, relatively *regular* patterns such as asters, in which stiff filaments or filament bundles radiate from a common center [5, 6], arise that resemble the mitotic spindles formed in dividing cells. A polarity sorting mechanism [5] has been proposed to explain the observed pattern. On the other hand, irregular *heterogeneous* cluster structures have been seen both in the actomyosin networks of *C. elegans* embryos [7] and in the minimal in vitro network model [8]. In the in vitro system, clusters of various sizes continuously change via fusion and rupture events but the distribution of cluster sizes remains steady. Motor-driven filament sliding and a well-tuned connectivity seem to play a key role in this nonequilibrium steady state.

In the present work, by looking into the intricate interplay between local force generation, network connectivity and collective motor action, we seek to provide a theoretical framework that is capable of accommodating both regular and heterogeneous pattern formation, as well as arrested coarsening and large-scale contraction in a unified manner. Our microscopic model is a motorized cat's cradle [9, 10, 11, 12] which consists of a crosslinked network of nonlinear elastic filaments where motors generate equal but oppositely directed kicks at motor-bonded node pairs. This model encodes two essential aspects of actomyosin self-organization: first that individual actin filaments have highly asymmetric responses to loading, resisting large tensile forces but easily buckling under compressive loads. As a consequence, sheared biopolymer networks exhibit negative normal stresses [13] comparable in magnitude to the shear stress. Secondly the model captures the fact that motor-induced node movements come in anti-correlated pairs owing to the bipolar minifilaments. This anti-correlation mimics the relative sliding of neighboring parallel filaments driven by the attached motors. Both aspects are crucial to capturing the formation of a disordered condensed state of actomyosin

aggregates.

Our coarse-grained model is completely microscopic but bears some resemblance to the macroscopic approach adopted by Levine and MacKintosh that introduces force dipoles into an elastic continuum [14, 15] where motor unbinding kinetics leads to enhanced low-frequency stress fluctuations. In the microscopic model the network connectivity and motor distribution over the bonds of the network are quenched once initially assigned, so that the nonequilibrium dynamics and structures predicted by our model arise solely from the intrinsic activity of motors firmly built into the network driving correlated motions stochastically. This assumption is in line with the fact that the *in vitro* structures are irreversibly assembled because many protein factors found *in vivo* that allow fast pattern renewals are left out of the reconstitution, such as disassembly of contractile structures and transience of actin crosslinking proteins. The model highlights the key role in determining the course of structural development played by the motor susceptibility, a parameter characterizing how sensitively the motors respond to imposed forces. The coupling between motor kinetics and the structure leads to a double-way feedback: Motor action induces structural changes of the network and thus modifies the local mechanical environment of the motors, which in turn changes the load-dependent motor response.

In the same spirit as our earlier work on the statistical mechanics of systems with uncorrelated kicks on each node [11, 12], we adopt a master equation description but treat small-step spatially *anti-correlated* kicks in order to mimic contractile-ratchet-like [2, 3] incremental deformations of actomyosin networks. We again obtain an effective Fokker-Planck equation in the small kick limit. But the correlations lead to *local* effective temperature $\mathbf{T}_{\text{eff}}$ and diffusion coefficients $\mathbf{D}_{\text{eff}}$, which now both become tensors and also depend on the *instantaneous* local network structure. More interestingly, anti-correlated kicking leads to a modification of the bare interaction. Essentially new forces come into play through the action of the motors. This motor-induced force depends linearly on the motor activity to quadratic order in kick step size and decays in space as the inverse distance in three dimensions, resembling a logarithmically growing potential. By

treating the motor-bonded node pairs as "functional units" and deriving a pair-level steady-state solution of the effective Fokker-Planck equation, we demonstrate that the motor-driven anti-correlated movements of actively-bonded nodes give an additional effective pair potential that exhibits a strong short-range attraction regardless of motor susceptibility. The original interaction is also still present but is an enhanced or weakened long-range attraction. For motors with negative susceptibility at sufficiently high activity, the dominant interaction is actually a long-range repulsion. The relative contributions of the various terms yield a diverse range of steady-state structures. This decoupling scheme in the mean-field spirit also allows us to perform a self-consistent calculation to evaluate quasi-thermodynamic phase diagrams. A non-monotonic dependence of the pressure (or tension) upon the node density (under susceptible motor kicks) indicates the possibility of phase separation.

To test the validity of the analytical approach, we compare the steady-state structural features found by Brownian dynamics simulations using the effective temperature and modified potential (both a tensor-parameter formalism and a pair-level scalar-parameter formalism) obtained from the steady-state solutions, with the structural features observed in a dynamic Monte Carlo simulation that is fully consistent with the master equation at thermal temperature and with bare interactions. We find good quantitative agreement suggesting that a non-equilibrium system driven by small-step correlated motor kicks can be thought of as being at an effective equilibrium with modified interactions.

The existence of an effective short-range attraction combined with the predicted tendency for phase separation suggests that the formation of steady heterogeneous cluster structures is an example of arrested phase separation [16, 17]. A force-percolating network consisting of nonlinear elastic fibers attains rigidity when local collapse induced by the motor-driven short-range attraction balances the concomitant neighboring bond stretching. This initially homogeneous network then develops into dense clumps connected by highly stretched bonds, and simultaneously, compact aggregates phase separate from node-poor regions. The coarsening process stops once a global balance is achieved, and the pertinent dynamic process

involves phase separation followed by arrest due to bond constraints. Our model naturally explains the formation of aster patterns through the notion of an effective repulsion.

6.2 Theory

In our earlier work [11] we showed how an effective temperature describes steady-state fluctuations and responses of a model cytoskeleton, treated as an amorphous network of crosslinked nonlinear-elastic filaments, driven by *uncorrelated* motor kicking events. Here we consider *anti-correlated* kicks. As sketched in Fig. 6.1, each motor (myosin minifilament) generates a pair of equal but oppositely directed displacements (red arrows) at the motor-connected crosslinks/nodes (purple spheres). These anti-correlated kicks mimic the contractile-rachet-like incremental movements due to myosin-driven relative sliding of neighboring actin filaments [2, 3]. We point out that myosin motors do not explicitly enter our model; instead, they are exemplified only through the anti-correlated kicks. The cartoon in Fig. 6.1 illustrates how these kicks are generated: A myosin minifilament attaches to two otherwise unconnected actin filaments and pulls the node on either filament toward each other. We then assume, for simplicity, that an implicitly-motor-attached filament/bond connects the node pair, neglecting the detailed architecture of the motor-filament composite (as seen in the zoom-out view in Fig. 6.1 top image). Anti-correlated kicks then act on the nodes at the two ends of such a (motor-attached) active bond.

The asymmetric load response of individual actin filaments is encoded via a nonlinear-elastic interaction between the bonded nodes, defined by the pair interaction potential $\beta U(r) = \Theta(r - L_e)\beta\gamma(r - L_e)^2/2$. Here $\Theta(\cdot)$ is the Heaviside step function and $\beta\gamma$ gives the effective stretching stiffness of the filaments with $\beta = 1/k_BT$. An energy cost arises only when the contour length r of a bond exceeds its relaxed length L_e. We call this interaction a "cat's cradle" interaction [9, 10, 11, 12]. For simplicity, we assume that all the bonds, no matter motor-attached or not, have the same relaxed length. Since the motor-driven forces

exceed by far the piconewton-threshold of affordable compressive loads, the induced buckling within a percolating actin network gives rise to a tensegrity structure composed of collapsed and stretched elements (illustrated in Fig. 6.2): In a permanently crosslinked network of filaments, such as the in vitro reconstituted networks, active sliding of filaments is constrained by passive crosslinking, in other words, local filament or bundle contraction is balanced by the stretching of neighboring filaments. An initially homogeneous network typically then develops into dense floppy clumps (concentrated short green wiggly lines) connected by highly stretched filaments (long red straight lines). This phenomenon leads to the formation of disordered actomyosin condensates [4] and can lead to active contractility [18].

6.2.1 Quadratic expansion of the master equation: effective equilibrium with modified potential

Fokker-Planck (FP)/Smoluchowski equation for Brownian particles

Consider a collection of N Brownian particles (i.e. nodes of our model network) labeled with positional coordinates $\vec{r}_i$ $(i = 1, \cdots, N)$. For infinitesimal step Brownian motion, the configurational probability density $\Psi(\{\vec{r}_i\}; t)$ is locally conserved and thus satisfies a continuity equation $\partial\Psi/\partial t = -\sum_i \nabla_{\vec{r}_i} \cdot \vec{J}_i$, where $\vec{J}_i$ is the probability current density along the coordinate of the ith particle.

For Brownian particles the probability current density is linearly related to the deviation of the configurational probability density from its equilibrium value

$$\vec{J}_i = -\sum_j \boldsymbol{D}^0_{ij}(\{\vec{r}_i\}) \cdot (\nabla_j \Psi + \beta \Psi \nabla_j U)\,. \tag{6.1}$$

Here $U(\{\vec{r}_i\})$ is the thermal equilibrium potential of mean force of the system and $\beta = (k_B T)^{-1}$. The equilibrium distribution $\Psi_{\rm eq}(\{\vec{r}_i\})$ is related to $U(\{\vec{r}_i\})$ according to $\Psi_{\rm eq}(\{\vec{r}_i\}) \propto \exp[-\beta U(\{\vec{r}_i\})]$. The diffusion coefficients $\boldsymbol{D}^0_{ij}$ are functions of the system's configuration and satisfy a generalized Einstein relation with the drag coefficients $\boldsymbol{\zeta}_{ij}$ reading $\boldsymbol{D}^0_{ij} = k_B T(\boldsymbol{\zeta})^{-1}_{ij}$, where $\boldsymbol{D}^0_{ij}$ and $\boldsymbol{\zeta}_{ij}$ are 3×3 matrices for each (i, j) pair.

When divided into self-diffusion and coupled-diffusion parts, the FP equation $\partial\Psi/\partial t = \hat{L}^0_{\rm FP}\Psi$ becomes

$$\begin{aligned}\frac{\partial}{\partial t}\Psi(\{\vec{r}_i\};t) &= \sum_i \nabla_i \cdot \boldsymbol{D}^0_{ii} \cdot (\nabla_i\Psi + \beta\Psi\nabla_i U) \\ &+ \sum_i \sum_{j\neq i} \nabla_i \cdot \boldsymbol{D}^0_{ij} \cdot (\nabla_j\Psi + \beta\Psi\nabla_j U). \end{aligned} \tag{6.2}$$

Note that the double gradient operation acts explicitly as

$$\begin{aligned}\nabla_i \cdot \boldsymbol{D}^0_{ij} \cdot \nabla_j\Psi &= (\nabla_i \cdot \boldsymbol{D}^0_{ij}) \cdot \nabla_j\Psi + \boldsymbol{D}^0_{ij} : \nabla_i\nabla_j\Psi, \\ \nabla_i \cdot \boldsymbol{D}^0_{ij} \cdot (\beta\Psi\nabla_j U) &= (\nabla_i \cdot \boldsymbol{D}^0_{ij}) \cdot (\beta\Psi\nabla_j U) + \boldsymbol{D}^0_{ij} : (\beta\nabla_i\Psi\nabla_j U + \beta\Psi\nabla_i\nabla_j U). \end{aligned} \tag{6.3}$$

Master equation for motor-driven processes: anti-correlated kicks

To mimic the motor-driven filament sliding in actomyosin networks, we describe the motors as generating anti-correlated kicks on pairs of crosslinks that pull in slack locally (Fig. 6.1 middle). Since the linear size of the myosin minifilaments is small compared to the mean separation between the crosslinks, the anti-correlated moves can be treated as being along the lines of centers. In view of the segmented structure of the actin filaments, which consist of periodically arranged subunits of linear size l (Fig. 6.1 bottom), we therefore assume a fixed kick step size l. l indicates the amplitude of relative node displacements due to a typical contraction event. Thus an anti-correlated kick pair acting on nodes i and j can be represented by a pair of displacements along the line of centers $(\vec{l}_{ij}, \vec{l}_{ji}) = l(\hat{r}_{ij}, -\hat{r}_{ij})$, where $\hat{r}_{ij}$ is a unit vector pointing from node i to node j. These anti-correlated kick pairs with equal size automatically satisfy momentum conservation on the macroscopic scale. Yet if we include explicitly the aqueous environment in which the cytoskeletal network is immersed, hydrodynamic interactions [19] between the nodes via the solvent should be taken into account. These interactions might modify the current simplified picture, and counteract any motor-induced force imbalance on individual nodes, thus validating momentum conservation on the microscopic scale as well.

The dynamical evolution of the many-particle configuration $\{\vec{r}_i\}$ due to these motor-driven events can be described by a master equation $\partial\Psi/\partial t = \hat{L}_{\rm NE}\Psi$ with

$$\hat{L}_{\rm NE}\Psi(\{\vec{r}_i\};t) = \int \Pi_i d\vec{r'}_i \left[K(\{\vec{r'}_i\} \to \{\vec{r}_i\})\Psi(\{\vec{r'}_i\};t) - K(\{\vec{r}_i\} \to \{\vec{r'}_i\})\Psi(\{\vec{r}_i\};t)\right], \tag{6.4}$$

where the integral kernel $K(\{\vec{r'}_i\} \to \{\vec{r}_i\})$ encodes the probability of transitions between different node configurations. Our earlier description [11, 12] of the motor kicking rate, k, still applies to current case for correlated kicks, i.e.,

$$k = \kappa[\Theta(\Delta U)\exp(-s_u\beta\Delta U) + \Theta(-\Delta U)\exp(-s_d\beta\Delta U)], \tag{6.5}$$

where κ is the basal kicking rate and $s_u(s_d)$ denotes motor susceptibility to energetically uphill (downhill) moves, except that now the free energy change ΔU is due to *pairs* of displacements. Explicitly we write

$$\begin{aligned}
&\hat{L}_{\rm NE}\Psi(\{\vec{r}_i\};t) = \frac{1}{2}\kappa\sum_i\sum_j C_{ij}\int d\vec{r'}_i\int d\vec{r'}_j \\
&\times\Big\{\delta(\vec{r}_i - \vec{r'}_i - \vec{l}_{ij})\delta(\vec{r}_j - \vec{r'}_j + \vec{l}_{ij}) \\
&\times w\left[U(\cdots,\vec{r'}_i,\cdots,\vec{r'}_j,\cdots) - U(\cdots,\vec{r}_i,\cdots,\vec{r}_j,\cdots)\right]\Psi(\{\vec{r'}_i\};t) \\
&-\delta(\vec{r}_i - \vec{r'}_i + \vec{l}_{ij})\delta(\vec{r}_j - \vec{r'}_j - \vec{l}_{ij}) \\
&\times w\left[U(\cdots,\vec{r}_i,\cdots,\vec{r}_j,\cdots) - U(\cdots,\vec{r'}_i,\cdots,\vec{r'}_j,\cdots)\right]\Psi(\{\vec{r}_i\};t)\Big\}.
\end{aligned}$$

The factor 1/2 avoids double counting in the summation over all pairs. The quantity C_{ij}, much like an element of a contact map in description of protein structures, defines whether the node pair (i,j) is connected by an active bond and thus subject to anti-correlated displacements $(\vec{l}_{ij}, -\vec{l}_{ij})$: $C_{ij} = C_{ji} = 1$ for motor-bonded pairs while $C_{ij} = C_{ji} = 0$ for non-bonded pairs. Our description of the rates gives $w[U_i - U_f] = \Theta(U_f - U_i)\exp[-s_u\beta(U_f - U_i)] + \Theta(U_i - U_f)\exp[-s_d\beta(U_f - U_i)]$.

Assuming symmetric motor susceptibility, i.e. $s_u = s_d = s$, one finds more

simply

$$\hat{L}_{\text{NE}}\Psi(\{\vec{r}_i\};t) = \frac{1}{2}\kappa\sum_i\sum_j C_{ij}$$
$$\times\Big\{e^{-s\beta\left[U(\vec{r}_i,\vec{r}_j)-U(\vec{r}_i-\vec{l}_{ij},\vec{r}_j+\vec{l}_{ij})\right]}\Psi(\{\cdots,\vec{r'}_i=\vec{r}_i-\vec{l}_{ij},\cdots,\vec{r'}_j=\vec{r}_j+\vec{l}_{ij},\cdots\};t)$$
$$-e^{-s\beta\left[U(\vec{r}_i+\vec{l}_{ij},\vec{r}_j-\vec{l}_{ij})-U(\vec{r}_i,\vec{r}_j)\right]}\Psi(\{\cdots,\vec{r}_i,\cdots,\vec{r}_j,\cdots\};t)\Big\}. \tag{6.6}$$

We assume that kicks on different pairs of nodes at any given time are uncorrelated. The rates of possible kicking events depend on the *instantaneous* node configuration reflecting an assumed Markovian character of the motor dynamics. There is no angular average due to the definiteness of kicking directions for a given configuration. Note that the motor power strokes and thus the kick steps are discrete occurring in a stochastic fashion. The correlated motions pull in slack locally while simultaneously pulling taut neighboring filaments until a global balance is reached or a macroscopic collapse occurs, depending on whether the motors are downhill prone (with a large positive s) or load-resisting (with a small or negative s), respectively.

Quadratic expansion of Eq. 6.6 in kick step size l leads to

$$\hat{L}_{\text{NE}}\Psi(\{\vec{r}_i\};t) = \frac{1}{2}\kappa l^2\sum_i\sum_j C_{ij}$$
$$\times\Big[\frac{1}{2}\hat{r}_{ij}\hat{r}_{ij}:\nabla_i\nabla_i\Psi+\frac{1}{2}\hat{r}_{ij}\hat{r}_{ij}:\nabla_j\nabla_j\Psi-\hat{r}_{ij}\hat{r}_{ij}:\nabla_i\nabla_j\Psi$$
$$+s\hat{r}_{ij}\hat{r}_{ij}:\nabla_i\Psi\nabla_i\beta U+s\hat{r}_{ij}\hat{r}_{ij}:\nabla_j\Psi\nabla_j\beta U$$
$$-s\hat{r}_{ij}\hat{r}_{ij}:\nabla_i\Psi\nabla_j\beta U-s\hat{r}_{ij}\hat{r}_{ij}:\nabla_j\Psi\nabla_i\beta U$$
$$+s\left(\hat{r}_{ij}\hat{r}_{ij}:\nabla_i\nabla_i\beta U+\hat{r}_{ij}\hat{r}_{ij}:\nabla_j\nabla_j\beta U-2\hat{r}_{ij}\hat{r}_{ij}:\nabla_i\nabla_j\beta U\right)\Psi\Big].$$

Notice that $\sum_i\sum_j C_{ij}\hat{r}_{ij}\hat{r}_{ij}:\nabla_i\nabla_i=\sum_i\sum_j C_{ij}\hat{r}_{ij}\hat{r}_{ij}:\nabla_j\nabla_j$, the above expression

can be rewritten as

$$\begin{aligned}\hat{L}_{\rm NE}\Psi(\{\vec{r}_i\};t) &= \sum_i \Big[\frac{1}{2}\kappa l^2 \sum_{j\neq i} C_{ij}\hat{r}_{ij}\hat{r}_{ij} : \nabla_i\nabla_i\Psi \\ &+ \beta s\kappa l^2 \sum_{j\neq i} C_{ij}\hat{r}_{ij}\hat{r}_{ij} : (\nabla_i\Psi\nabla_i U + \Psi\nabla_i\nabla_i U)\Big] \\ &- \sum_i\sum_{j\neq i}\Big[\frac{1}{2}\kappa l^2 C_{ij}\hat{r}_{ij}\hat{r}_{ij} : \nabla_i\nabla_j\Psi \\ &+ \beta s\kappa l^2 C_{ij}\hat{r}_{ij}\hat{r}_{ij} : (\nabla_i\Psi\nabla_j U + \Psi\nabla_i\nabla_j U)\Big]. \qquad (6.7)\end{aligned}$$

The definitions in Eq. 6.3 allow us to express $\hat{L}_{\rm NE}\Psi$ in the form of the divergence of a flux plus some extra terms which modify the bare interactions as shown below.

Generalized FP equation for motorized systems: effective temperature and modified potential

By combining the pure Brownian dynamics (Eq. 6.2) with the nonequilibrium dynamics due to correlated motor-driven processes up to $O(l^2)$ (Eq. 6.7), we obtain an effective FP equation with effective tensor parameters ($\boldsymbol{D}^{\rm eff}$ and $\boldsymbol{\beta}_{\rm eff}$) and sitewise modified potentials ($U_{\rm mod}$)

$$\begin{aligned}(\hat{L}^0_{\rm FP} + \hat{L}_{\rm NE})\Psi(\{\vec{r}_i\};t) &= \sum_i \Big[\nabla_i\cdot\boldsymbol{D}^{\rm eff}_{ii}\cdot\nabla_i\Psi + \nabla_i\cdot\big(\boldsymbol{D}^{\rm eff}_{ii}\cdot\boldsymbol{\beta}^i_{\rm eff}\big)\cdot\big(\Psi\nabla_i U^i_{mod}\big)\Big] \\ &+ \sum_i\sum_{j\neq i}\Big[\nabla_i\cdot\boldsymbol{D}^{\rm eff}_{ij}\cdot\nabla_j\Psi \\ &+ \nabla_i\cdot\big(\boldsymbol{D}^{\rm eff}_{ij}\cdot\boldsymbol{\beta}^{ij}_{\rm eff}\big)\cdot\big(\Psi\nabla_j U^j_{mod}\big)\Big]. \qquad (6.8)\end{aligned}$$

The effective diffusion constants read

$$\boldsymbol{D}^{\rm eff}_{ii} = \boldsymbol{D}^0_{ii} + \frac{1}{2}\kappa l^2\sum_{j\neq i} C_{ij}\hat{r}_{ij}\hat{r}_{ij},\ \boldsymbol{D}^{\rm eff}_{ij} = \boldsymbol{D}^0_{ij} - \frac{1}{2}\kappa l^2 C_{ij}\hat{r}_{ij}\hat{r}_{ij}. \qquad (6.9)$$

The effective temperatures are given by

$$\begin{aligned}\boldsymbol{\beta}^i_{\rm eff} &= \beta\Big(\boldsymbol{D}^0_{ii} + s\kappa l^2\sum_{j\neq i} C_{ij}\hat{r}_{ij}\hat{r}_{ij}\Big)\cdot\Big(\boldsymbol{D}^0_{ii} + \frac{1}{2}\kappa l^2\sum_{j\neq i} C_{ij}\hat{r}_{ij}\hat{r}_{ij}\Big)^{-1}, \\ \boldsymbol{\beta}^{ij}_{\rm eff} &= \beta\Big(\boldsymbol{D}^0_{ij} - s\kappa l^2 C_{ij}\hat{r}_{ij}\hat{r}_{ij}\Big)\cdot\Big(\boldsymbol{D}^0_{ij} - \frac{1}{2}\kappa l^2 C_{ij}\hat{r}_{ij}\hat{r}_{ij}\Big)^{-1}. \qquad (6.10)\end{aligned}$$

The modified potentials $U^{i(j)}_{\rm mod} = U + \Lambda^{i(j)}$ involve the (additive) modifications Λ that satisfy

$$-\nabla_i \Lambda^i = -\Big[\nabla_i \cdot \big(\frac{1}{2}\kappa l^2 \sum_{j\neq i} C_{ij}\hat{r}_{ij}\hat{r}_{ij}\big)\Big] \cdot \Big[\big(\boldsymbol{D}^0_{ii} + s\kappa l^2 \sum_{j\neq i} C_{ij}\hat{r}_{ij}\hat{r}_{ij}\big)\beta\Big]^{-1},$$
$$-\nabla_j \Lambda^j = \Big[\nabla_i \cdot \big(\frac{1}{2}\kappa l^2 C_{ij}\hat{r}_{ij}\hat{r}_{ij}\big)\Big] \cdot \Big[\big(\boldsymbol{D}^0_{ij} - s\kappa l^2 C_{ij}\hat{r}_{ij}\hat{r}_{ij}\big)\beta\Big]^{-1}. \qquad (6.11)$$

We assume that the active connectivity described by $\{C_{ij}\}$ is quenched once initially assigned and use the identity that $\nabla_j \cdot (\hat{r}_{ij}\hat{r}_{ij}) = -\nabla_i \cdot (\hat{r}_{ij}\hat{r}_{ij}) = \hat{r}_{ij}(d-1)/r_{ij}$, where d is the spatial dimension and $r_{ij} = |\vec{r}_i - \vec{r}_j|$, to obtain explicit expressions.

Several nontrivial features can be read off from the above expressions (Eqs. 6.8–6.11):

(1) There is a key difference from the simple situation for uncorrelated isotropic kicks [11, 12]. In that case an average over kicking directions yields *uniform scalars* $T_{\rm eff}$ and $D_{\rm eff}$ which are fully determined by the motor properties (motor susceptibility s and activity defined as $\Delta \equiv \kappa l^2/D_0$) regardless of the specific structure of the system. Under correlated kicks along the lines of centers, however, both $\boldsymbol{T}_{\rm eff}$ and $\boldsymbol{D}_{\rm eff}$ become *local tensors*. These tensors depend on local network structure (relative position of bonded neighbors $\vec{r}_{ij}$) and motor distribution (quenched active connectivity defined by C_{ij}) about the central node i. The tensorial nature of the effective diffusion coefficients ($\boldsymbol{D}_{\rm eff}$) and mobility ($\boldsymbol{\mu}_{\rm eff} \equiv \boldsymbol{D}_{\rm eff} \cdot \boldsymbol{\beta}_{\rm eff}$) leads to the diffusive flux not aligning with the density gradient or the drift flux. Motor-induced modifications to the forces ($-\nabla_i U_{\rm mod}$) and to the transport coefficients ($\boldsymbol{D}_{\rm eff}$ and $\boldsymbol{\mu}_{\rm eff}$) only have longitudinal components since $\hat{r}_{ij}\hat{r}_{ij}$ essentially serves as a longitudinal projection operator.

(2) Anti-correlation of the myosin-generated kicks at the two ends of the actin filaments provides a microscopic basis for the anisotropy of actin diffusivity: The anti-correlated kicks enhance self-diffusion of individual molecules, whereas they slow the relative coupled diffusion of motor-bonded molecules (Eq. 6.9). Recent experiments [20] indeed have reported that motor activity can give rise to cytoplasmic motion that has the appearance of diffusion but is significantly enhanced in its magnitude. Such "active" cytoplasmic diffusion could enable rapid

intracellular transport of matter and information.

(3) To quadratic order in kick step size l, it is easy to show:

(a) Both $\nabla_i (\Lambda^i/k_BT)$ and $\nabla_j (\Lambda^j/k_BT)$ are proportional to $\kappa l^2/D_0$. This indicates that the motor-induced forces depend linearly on the strength of the kicking noise relative to the thermal noise in small kick limit.

(b) The inverse effective temperature tensor becomes

$$\begin{aligned}\boldsymbol{\beta}^i_{\text{eff}} &= \beta\left(D_0\mathbf{1} + s\kappa l^2\sum_{j\neq i} C_{ij}\hat{r}_{ij}\hat{r}_{ij}\right)\cdot\left(\frac{1}{D_0}\right)\left(\mathbf{1} - \frac{1}{2}\frac{\kappa l^2}{D_0}\sum_{j\neq i} C_{ij}\hat{r}_{ij}\hat{r}_{ij} + O(l^4)\right)\\ &= \beta\left[\mathbf{1} + (s-\frac{1}{2})\frac{\kappa l^2}{D_0}\sum_{j\neq i} C_{ij}\hat{r}_{ij}\hat{r}_{ij}\right] + O(l^4)\end{aligned}$$

Anti-correlated kick pairs give rise to effective temperature tensors that depend on local active connectivity, implying that the speed of heat flow in motor-kicking directions ($C_{ij} \neq 0$ thus $T_{\text{eff}} \neq T$) is different from energy flux along motor-free directions ($C_{ij} = 0$ thus $T_{\text{eff}} = T$). Along individual active bonds, as for the uncorrelated kick case, we have $T_{\text{eff}} < T$ if $s > 1/2$ whereas $T_{\text{eff}} > T$ if $s < 1/2$, as well as the same detailed balance condition that if $s = 1/2$ then $T_{\text{eff}} = T$.

Therefore the nonequilibrium system driven by small-step anti-correlated motor kicks may be described by an effective FP (Smoluchowski) equation at local effective temperature and with modified interaction potential.

6.2.2 Pair-level steady-state solution

We may ask whether it is still possible to obtain an explicit (but perhaps approximate) steady-state solution to an effective Fokker-Planck equation with tensor transport coefficients and modified interaction potential. Existence of such a solution makes possible the mapping of the system to an equilibrium system even for this nonequilibrium situation with spatially correlated motorized events. This mapping thus allows the study of rheological properties within a quasi-equilibrium framework. The main difficulty in making this mapping arises from the tensorial nature of the effective temperature which depends on local structures.

To approximate the N-body solution, we employ a decoupling scheme that reduces the problem to finding the steady states for the diffusion of "functional

units". We will first study the simplest case for a single pair of motor-bonded nodes without hydrodynamic interactions, i.e., neglecting the $\boldsymbol{D}_{ij}$-related terms. A straightforward calculation leads to an explicit steady-state solution to this two-body problem.

Consider a pair of nodes located at $\vec{r}_1$ and $\vec{r}_2$. For purely Brownian motion, the 2-body configurational probability density $\Psi(\vec{r}_1, \vec{r}_2; t)$ evolves according to the bare Fokker-Planck equation $\partial\Psi/\partial t = \hat{L}^0_{\text{FP}}\Psi$ with

$$\hat{L}^0_{\text{FP}}\Psi = \sum_{i=1,2} \left[\nabla_i \cdot \boldsymbol{D}^0_{ii} \cdot \nabla_i \Psi + \nabla_i \cdot \boldsymbol{\mu}^0_{ii} \cdot \nabla_i U \Psi\right]. \tag{6.12}$$

Here the mobility tensor is related to the diffusion tensor simply by a multiplication of the inverse scalar temperature as $\boldsymbol{\mu}^0_{ii} = \beta \boldsymbol{D}^0_{ii}$. The steady-state solution thus obeys the usual Boltzmann law $\Psi^0_{ss} \propto \exp[-\beta U(r_{12})]$ where the interaction potential U only depends on the node separation $r_{12} = |\vec{r}_1 - \vec{r}_2|$ in the absence of external fields.

The dynamic evolution of a pair due to anti-correlated motor kicks is described by a master equation $\partial\Psi/\partial t = \hat{L}_{\text{NE}}\Psi$ with

$$\begin{aligned} \hat{L}_{\text{NE}}\Psi(\vec{r}_1, \vec{r}_2; t) = \kappa C_{12} \quad \Big\{ & \quad e^{-s\beta\left[U(\vec{r}_1,\vec{r}_2) - U(\vec{r}_1 - \vec{l}_{12}, \vec{r}_2 + \vec{l}_{12})\right]} \\ & \times \quad \Psi(\vec{r}\,'_1 = \vec{r}_1 - \vec{l}_{12}, \vec{r}\,'_2 = \vec{r}_2 + \vec{l}_{12}; t) \\ & - \quad e^{-s\beta\left[U(\vec{r}_1 + \vec{l}_{12}, \vec{r}_2 - \vec{l}_{12}) - U(\vec{r}_1, \vec{r}_2)\right]} \Psi(\vec{r}_1, \vec{r}_2; t) \Big\} \end{aligned} \tag{6.13}$$

By combining the pure Brownian dynamics (Eq. 6.12) and the motor-driven dynamics (Eq. 6.13) we obtain in the small kick limit an effective Fokker-Planck equation characterized by effective diffusion constants, tensor effective temperature as well as a modified potential

$$(\hat{L}^0_{\text{FP}} + \hat{L}_{\text{NE}})\Psi(\vec{r}_1, \vec{r}_2; t) = \sum_{i=1,2} \left[\nabla_i \cdot \boldsymbol{D}^{\text{eff}}_{ii} \cdot \nabla_i \Psi + \nabla_i \cdot (\boldsymbol{D}^{\text{eff}}_{ii} \cdot \boldsymbol{\beta}^i_{\text{eff}}) \cdot (\Psi \nabla_i U^i_{\text{mod}})\right]. \tag{6.14}$$

In this two-body case, the effective diffusion tensors, up to $O(l^2)$, are given by

$$\boldsymbol{D}^{\text{eff}}_{11} = D_0 \mathbf{1} + C_{12}\frac{1}{2}\kappa l^2 \hat{r}_{12}\hat{r}_{12} = D_0 \mathbf{1} + C_{21}\frac{1}{2}\kappa l^2 \hat{r}_{21}\hat{r}_{21} = \boldsymbol{D}^{\text{eff}}_{22}. \tag{6.15}$$

The effective mobility tensors, up to $O(l^2)$, are given by

$$\boldsymbol{\mu}^{\text{eff}}_{11} = \beta\left(D_0 \mathbf{1} + C_{12} s\kappa l^2 \hat{r}_{12}\hat{r}_{12}\right) = \beta\left(D_0 \mathbf{1} + C_{21} s\kappa l^2 \hat{r}_{21}\hat{r}_{21}\right) = \boldsymbol{\mu}^{\text{eff}}_{22}. \tag{6.16}$$

The tensor effective temperatures thus read

$$\boldsymbol{\beta}_1^{\text{eff}} = \boldsymbol{\beta}_2^{\text{eff}} = \beta \left[\mathbf{1} + C_{12} \left(s - \frac{1}{2} \right) \frac{\kappa l^2}{D_0} \hat{r}_{12} \hat{r}_{12} \right] + O(l^4).$$

The modifications to the bare forces are central forces that decay in space as $1/r$:

$$-\nabla_1 \Lambda = C_{12} \frac{\kappa l^2}{\beta D_0} \frac{1}{r_{12}} \hat{r}_{12}\,, \quad -\nabla_2 \Lambda = C_{21} \frac{\kappa l^2}{\beta D_0} \frac{1}{r_{21}} \hat{r}_{21} = -\left[-\nabla_1 \Lambda \right],$$

suggesting the following form of the modified potential

$$U_{\text{mod}}(r_{12}) = U(r_{12}) + C_{12} \frac{\kappa l^2}{D_0} k_B T \ln(r_{12}) + \text{const.} \tag{6.17}$$

For $s = 1/2$, the effective temperature becomes uniform scalar again $\boldsymbol{\beta}^{\text{eff}} = \beta \mathbf{1}$. The steady-state pair solution thus has precisely the form

$$\Psi_{ss}(r_{12}) \propto \exp[-\beta U_{\text{mod}}(r_{12})]$$

where U_{mod} is given by Eq. 6.17.

For $s \neq 1/2$, we have

$$\begin{aligned} \boldsymbol{\beta}^{\text{eff}} \cdot [-\nabla_1 U_{\text{mod}}] &= \beta \left[\mathbf{1} + C_{12} \left(s - \frac{1}{2} \right) \frac{\kappa l^2}{D_0} \hat{r}_{12} \hat{r}_{12} \right] \cdot \left(-\nabla_1 U + C_{12} \frac{\kappa l^2}{\beta D_0} \frac{1}{r_{12}} \hat{r}_{12} \right) \\ &= \beta \left[1 + C_{12} \left(s - \frac{1}{2} \right) \frac{\kappa l^2}{D_0} \right] [-\nabla_1 U] + C_{12} \frac{\kappa l^2}{D_0} \frac{1}{r_{12}} \hat{r}_{12} + O(l^4) \end{aligned} \tag{6.18}$$

and

$$\boldsymbol{\beta}^{\text{eff}} \cdot [-\nabla_2 U_{\text{mod}}] = -\boldsymbol{\beta}^{\text{eff}} \cdot [-\nabla_1 U_{\text{mod}}]\,. \tag{6.19}$$

Here we have used the identity $\hat{r}_{12}(\hat{r}_{12} \cdot \nabla_1 U) = \nabla_1 U$, since $\nabla_1 U$ is parallel to $\hat{r}_{12}$ in the two-body situation. We see therefore that we still arrive at a steady-state solution given by

$$\Psi_{ss} \propto \exp \left\{ -\beta \left[1 + C_{12} \left(s - \frac{1}{2} \right) \frac{\kappa l^2}{D_0} \right] U - C_{12} \frac{\kappa l^2}{D_0} \ln(r_{12}) \right\} \equiv \exp \left[-\bar{\beta}_{\text{eff}} U_{\text{eff}} \right], \tag{6.20}$$

where the scalar inverse effective temperature ($\bar{\beta}_{\text{eff}}$) and the effective interaction potential (U_{eff}) are given by

$$\bar{\beta}_{\text{eff}} = \beta \left[1 + C_{12} \left(s - \frac{1}{2} \right) \frac{\kappa l^2}{D_0} \right] \tag{6.21}$$

and

$$U_{\text{eff}} = U + \frac{C_{12}\,(\kappa l^2/D_0)}{1 + C_{12}(s-1/2)\,(\kappa l^2/D_0)}\,k_B T \ln(r_{12}). \tag{6.22}$$

Since on the pair level the *total* force is automatically along the line of centers, $\bar{T}_{\text{eff}}$ becomes effectively a scalar. Thus at the pair level the steady states take a form consistent with our earlier result for uncorrelated isotropic kicks [11] (note that here is no $1/d$ factor that arises from the angular average). The modification to the bare interaction now, however, yields an additional central force which decays in space as $1/r$. In the limit of high motor activity, i.e., $\Delta \equiv \kappa l^2/D_0 \gg 1$, Eq. 6.22 reduces to $U_{\text{eff}} - U \simeq k_B T \ln(r_{12})/(s-1/2)$. We see the motor-induced forces can be attractive or repulsive depending on whether the motor susceptibility s is larger or smaller than 1/2, respectively.

The scaled effective pair potential given by $\bar{\beta}_{\text{eff}} U_{\text{eff}} = \beta U\,[1 + C_{12}(s-1/2)\Delta] + C_{12}\Delta \ln(r_{12})$ consists of two terms. The first term indicates that the motor action may enhance or weaken the long-range attraction, arising from the ordinary bond stretching in the model cytoskeleton. The sign of this effect depends on the sign of $(s-1/2)$. The second effect of the anti-correlated motors is an effective confinement potential that promotes further contraction even in the buckling regime. This term is independent of motor susceptibility. Therefore by varying s we may distinguish the influences of either term.

Fig. 6.3 displays the profile of the effective pair interaction U_{eff} (Eq. 6.22) scaled by the effective temperature $\bar{\beta}_{\text{eff}}^{-1}$ (Eq. 6.21). As shown in panels (a) and (c), when the motor susceptibility s is varied the long-range interaction becomes modified but the effective attraction at small separations is not affected. In contrast, increasing the motor activity Δ not only influences interactions at large distances but also enhances the short-range attraction, as seen in panels (b) and (d). Notably, at sufficiently high activity, load-resisting motor kicks ($s < 0$) may yield a long-range repulsion, i.e. the slope of the $\bar{\beta}_{\text{eff}} U_{\text{eff}}$ curve becomes negative at large r (see two lowest curves in panels c and d). As a consequence, an energy barrier (indicated by the red arrow) appears at intermediate distances, indicating the tendency for node separation and thus bond stretching that ultimately leads to aster formation observed in simulations.

6.2.3 Self-consistent phonon (SCP) calculation: possibility of phase separation

The pair-level steady-state solution derived above allows us to obtain the effective pair potential and self consistently determine the Debye-Waller factor of the localized nodes using the self-consistent phonon (SCP) method [21]. It is straightforward to derive the effective potential associated with a "cat's cradle" with excluded volume [10], i.e., a system where the nonlinear bonds (with an effective stiffness $\beta\gamma$) stretch elastically when their contour length exceeds the relaxed length L_e but that buckle upon shortening too much. We assume a negligibly small hard core size (σ) for comparison with simulations. We assign two mean-field parameters to characterize the network architecture: (1) network connectivity, P_c, which denotes the fraction of nearest-neighbor pairs that are bonded by filaments; (2) motor concentration, P_a, which indicates the fraction of active bonds that are attached by motors and thus induce anti-correlated kicks on the connected node pairs.

By using the independent oscillator approximation which yields sitewise decoupling of the particles, the free energy (due to configurational degrees of freedom) is expressed as a sum of the effective potentials between the interacting density clouds

$$\beta V_{\text{eff}}(|\vec{r}_i - \vec{r}_j^{\,f}|;\alpha_j) = -\ln \int d\vec{r}_j \rho_j(\vec{r}_j) e^{-\frac{1}{2}\beta U(\vec{r}_i - \vec{r}_j)}, \tag{6.23}$$

which essentially averages the Mayer f-bond, $\exp\left[-(1/2)\beta U(\vec{r}_i - \vec{r}_j)\right]$, over the location of the $\vec{r}_j$ particle with an assumed Gaussian density distribution about the fiducial position $\vec{r}_j^{\,f}$

$$\rho(\vec{r}_j, \vec{r}_j^{\,f}) = \left(\frac{\alpha_j}{\pi}\right)^{d/2} e^{-\alpha_j(\vec{r}_j - \vec{r}_j^{\,f})^2}, \tag{6.24}$$

where d is the spatial dimension of the system.

Self consistency requires that the effective potential mimics the harmonic comparison potential. Thus the curvature of the effective potential must coincide with the phonon frequency or spring constant of the Einstein harmonic oscillators.

This gives a coupled set of self-consistent equations for $\{\alpha_i\}$

$$\alpha_i = \frac{1}{2d}\sum_j Tr[\nabla\nabla V_{\rm eff}(|\vec{r}_i^{\,f} - \vec{r}_j^{\,f}|;\alpha_j)]. \tag{6.25}$$

In the present work the force constants $\{\alpha_i\}$ will be taken to be equal. This is an effective medium approximation.

For a cat's cradle with excluded volume and subject to correlated motor kicks described by the pair-level interaction (Eqs. 6.21–6.22), the effective potential $\widetilde{\beta}_{\rm eff}\widetilde{V}_{\rm eff}$ can be expressed as

$$e^{-\widetilde{\beta}_{\rm eff}\widetilde{V}_{\rm eff}(R,\,\alpha)} = \sqrt{\frac{\alpha}{\pi}}\frac{1}{R}\int_0^\infty dw w\left[e^{-\alpha(w-R)^2} - e^{-\alpha(w+R)^2}\right] \times f(w), \tag{6.26}$$

where the function $f(w)$ encodes the pair interaction depending on whether the nodes are bonded and whether the bond is motor-attached. $f(w)$ can be written in terms of the Heaviside step function $\Theta(x)$ as follows

$$\begin{aligned} f(w) \;=\; & (1-P_c)\Theta(w-\sigma) \\ & +P_c(1-P_a)\left[\Theta(w-\sigma)\Theta(L_e-w) + \Theta(w-L_e)\times e^{-\frac{1}{4}\beta\gamma(w-L_e)^2}\right] \\ & +P_cP_a\Big[\Theta(w-\sigma)\Theta(L_e-w)\times w^{-\Delta/2} \\ & +\Theta(w-L_e)\times w^{-\Delta/2}e^{-\frac{1}{4}\beta\gamma[1+(s-1/2)\Delta](w-L_e)^2}\Big]. \end{aligned} \tag{6.27}$$

Here the first line denotes the interaction between non-bonded pairs where only hard-core repulsion enters (σ stands for the hard-core diameter); the second line is due to the interaction between passively-bonded pairs where elastic bond stretching takes place beyond L_e; the third line accounts for the interaction between actively-bonded pairs where anti-correlated motor kicks induce an effective attraction even in the buckling regime ($\sigma < w < L_e$) and yield an effective bond stiffness that depends on motor activity and susceptibility.

Fig. 6.4 shows the profile of the effective potential $\widetilde{\beta}_{\rm eff}\widetilde{V}_{\rm eff}(R,\,\alpha)$ given by Eq. 6.26 at various values of motor activity (Δ) and susceptibility (s). Panel (a) illustrates the logarithmically growing potential at small separations due to motor-induced effective attraction, and the quadratically increasing potential at large distances due to ordinary bond stretching. Under susceptible motor kicks

($s = 1$), both the short-range and long-range attractions become enhanced as the motor activity increases. The dashed line marks the location where the elasticity of individual filaments sets in (i.e. $R = L_e$). A zoom-in view of the small-R region in panel (a) close to the elasticity onset (shaded region) is presented in panel (b). This figure clearly shows that the effective average potential increases monotonically with increasing separation; there is no inflection point or kink in the potential profile which would kinetically slow binding. Thus no difficulty is expected for initial aggregation, as evidenced by simulations. For load-resisting motors (panel c), however, as the motor activity increases, long-range attraction apparently becomes weakened due to a higher T_{eff}, while the susceptibility-independent short-range attraction still gets stronger. No finite α solution can be stabilized when the motor activity gets too high ($\Delta > 1$), signaling the development of spatial heterogeneity. Inhomogeneous/Site-dependent α solutions should recover the energy barrier at high motor activity, as seen for the pair-level solution (Fig.3c and d). We demonstrate in panel (d) how the effective potential changes with motor susceptibility. As expected, varying s has little effect on the effective attraction at short distances (more clearly seen in the inset), yet increasingly susceptible motors greatly strengthen the long-range attraction.

In our model, given the asymmetric load response of the nonlinear elastic bonds, the effective attraction between motor-bonded nodes may well drive phase separation of a force-percolating network into dense clumps against voids, i.e. local condensates of contracted bonds (analogous to the droplets of the condensed phase) connected by stretched bonds (associated with surface tension of the droplets), as sketched in Fig. 6.2. Spontaneous formation of disordered aggregates has indeed been observed in reconstituted actomyosin systems [4, 18]. Computer simulations of the model network when subjected to correlated motor kicks also show that substantial spatial heterogeneity develops when we started from a uniform distribution of motors over an isotropic network (see Fig. 6.5e for an example).

One thermodynamic indicator of phase separation is a non-monotonic dependence of the pressure upon the density of the constituents. We thus examine how the pressure varies with the node density using the self-consistently determined

phonon frequency. To avoid structural complexity we perform the calculations on regular lattices, yet we expect the same qualitative behavior for random lattices where an isotropic radial distribution function for the fiducial configurations can be obtained from simulations. The pressure p for a simple cubic lattice with a lattice constant R and a total number of N nodes at the ambient temperature T can be evaluated by numerically differentiating the free energy F as given by

$$p = -\frac{1}{3R^2}\left(\frac{\partial}{\partial R}F\right)_{T,N} k_B T, \tag{6.28}$$

where $F = z\widetilde{\beta}_{\text{eff}}\widetilde{V}_{\text{eff}}(R,\, \alpha; \Delta, s)$ with coordination number $z = 6$ for a simple cubic lattice. The dependence of pressure upon motor properties arises from the effective interaction encoded through $f(w)$ (Eq. 6.27) and from the self-consistent α solution.

[Note that since we have ignored the influence of motor-induced effective interaction on the fiducial structures, the SCP calculation may overestimate the instability threshold of the homogeneous state in terms of motor susceptibility s. Nevertheless, given the perturbative nature of the pair solution, any quantitative deviation should be modest.]

6.3 Simulations

To test the validity of the idea of using local effective temperature along with a modified potential for the motorized system, we have performed three types of simulations and compared the resulting steady-state structures. These simulation models are:

(1) Brownian dynamics simulations using a *tensor*-parameter Langevin equation consistent with the effective Fokker-Planck equation (Eq. 6.8)

(2) Brownian dynamics simulations at $\bar{T}_{\text{eff}}$ (Eq. 6.21) and with a modified potential U_{eff} (Eq. 6.22) using a *scalar*-parameter Langevin equation based on the pair-level steady-state solution

(3) Stochastic simulations incorporating anti-correlated kicks along individual active bonds as chemical reaction channels, at bath temperature T and with the bare interaction potential $U(\{\vec{r}_i\})$. This is of course the most realistic model.

6.3.1 Simulation setup

We investigate a model cytoskeleton that consists of nonlinear elastic filaments subjected to anti-correlated kicks on the motor-bonded node pairs. The *bare* interaction $U(r)$ between bonded nearest-neighbor pairs is taken to be of the cat's cradle type defined earlier, i.e. $\beta U(r) = \Theta(r - L_e)\beta\gamma(r - L_e)^2/2$. The assumed weakness of the excluded volume effect allows large-scale structural rearrangements to occur rather readily.

We build the model network on a simple cubic lattice to avoid structural complexity, and connect the nearest-neighbor nodes with nonlinear elastic bonds at a given probability P_c. Note that despite the regular lattice structure, disorder is still inherent in the randomness of bond connectivity for a partially connected network ($P_c < 1$). In most of the cases that we will study, we assume $P_a = 1$, i.e., all the bonds are motor-attached. The bond connectivity and motor distribution are quenched once initially assigned; there are no bond or motor rupture events. We choose the filament relaxed length L_e to be larger than the lattice spacing (set as the length unit in simulations), so that the initial homogeneous network is completely floppy with no tense bonds at all. The system size is $N = 6^3$ and periodic boundary conditions are applied.

Since we are interested in the steady-state behavior at an effective equilibrium, we have chosen a kick step size that is sufficiently small such that higher order contributions to the l-expansion are not significant. On the other hand, the kick size is large enough such that the motor-induced effective interaction outcompetes the thermal randomization. What affects the dynamics and structural development is the dimensionless motor activity or Péclet number $\Delta \equiv \kappa l^2/D_0$ which describes the relative strength of the motor kicking noise with respect to the thermal noise. Since in Brownian dynamics formalisms the motor kicking rate κ and the kick step size l always appear in combination as κl^2, an appropriate kicking rate has been chosen such that $\Delta > 1$ yet no instability occurs. [In stochastic simulations, however, a higher basal kicking rate κ yields a faster approach to the steady state without influencing the steady-state features, since the basal kicking rate does not affect the *relative* probability of different kicking events.]

Brownian dynamics (BD) simulations [22] have been implemented via the position Langevin equation $\Delta\vec{r}_i(t) = \boldsymbol{\mu}^i_{\rm eff}\cdot(-\nabla_i U_{\rm mod})\Delta t + \vec{R}^{\rm eff}_i(\Delta t)$, where $\vec{R}^{\rm eff}_i(\Delta t)$ represents the random motion due to thermal noise. The tensor formalism is equivalent to the effective Fokker-Planck equation (Eq. 6.8) yet without hydrodynamic interactions. The total mobility of node i is given by $\boldsymbol{\mu}^i_{\rm eff} = \beta(D_0\mathbf{1} + s\kappa l^2\sum_j C_{ij}\hat{r}_{ij}\hat{r}_{ij})$, and the modified interaction force $(-\nabla_i U_{\rm mod})$ comprises the total mechanical force $(-\nabla_i U)$ acting on node i and the effective interaction $(-\nabla_i\Lambda)$ given by Eq. 6.11. The movement due to motor-induced effective attraction thus follows $\boldsymbol{\mu}^i_{\rm eff}\cdot(-\nabla_i\Lambda) = \kappa l^2\sum_j C_{ij}\hat{r}_{ij}/r_{ij}$ to quadratic order in l. The scalar formalism, based on the pair-level steady-state solution (Eq. 6.20), sums up the contribution from individual bonded neighbors j, i.e., $\boldsymbol{\mu}^i_{\rm eff}\cdot(-\nabla_i U_{\rm mod}) \to \sum_j \boldsymbol{\mu}^{ij}_{\rm eff}\cdot\vec{F}^{ij}_{\rm mod} = \sum_j \beta(D_0 + C_{ij}s\kappa l^2)\vec{F}^{ij}(r_{ij}) + \kappa l^2\sum_j C_{ij}\hat{r}_{ij}/r_{ij}$, where $\vec{F}^{ij}(r_{ij})$ is the bare interaction force between node i and its bonded neighbor j. The stochastic dynamics governed by the full master equation (Eq. 6.6) has been realized by implementing dynamic Monte Carlo simulations [23] that obey the model kinetic rate (Eq. 6.5).

For making comparisons between the various simulation schemes, we ensure that all runs utilize the same lattice structure, bond connectivity and motor properties. Converging steady-state behavior would then validate the picture of an effective equilibrium at the effective temperature and with the modified interaction as predicted by the expansion.

6.3.2 Illustrations

Validity of an effective equilibrium and arrested phase separation

An explicit way to test the validity of picturing the non-equilibrium system driven by small-step motors as being at an effective equilibrium is to compare the steady-state characteristics resulting from the three types of simulations that we described above.

At a modest kick step size ($l = 0.03$), all three simulation schemes lead to quite similar steady-state behavior despite disparate dynamics toward the steady state. The structural characteristics include (1) the mean squared node displacement (MSD) with respect to the initial regular configuration and (2) the amplitude

of the innermost peak of the pair distribution function (PDF) which reflects the strength of aggregation. The PDF is defined as $\mathrm{PDF}(r) = C\delta n(r, r+\delta r)/r^2\delta r$ where $\delta n(r, r+\delta r)$ counts the number of particles within an interval δr at a distance r from the central particle, and the numeric factor C takes care of normalization. Both of these measures are almost identical for all the three schemes; they saturate to the same steady-state plateau value (see Fig. 6.5c, d). The PDF profile in the main panel of Fig. 6.5d is obtained by averaging over a wide steady-state time window. Note that the compact aggregation, reflected in the steep rise of the PDF in the vicinity of the central node (i.e. the dominant peak at the minimum separation), results from the motor-induced short-range attraction in addition to the absence of excluded volume. The inset shows the time evolution of the aggregation strength. The slight disparity in the potential energy (Fig. 6.5a) and the fraction of taut bonds (Fig. 6.5b) seen in each simulation might arise from the perturbative nature of the expansion as well as from the difference in dynamics. As the kick step size increases we would expect larger deviations. The close resemblance of the steady-state node configurations and bond structures between different schemes (Fig. 6.5e) lends explicit support to the equivalence of the three schemes in the small kick limit, thus validating the picture of an effective equilibrium with modified interactions.

To demonstrate the arrested phase separation, as anticipated from our theory, the network connectivity has been chosen to be sufficient for tension percolation yet moderate enough to allow considerable local force asymmetry ($P_c = 0.4$, i.e. $z = 2$–3). The initial network is completely floppy (in green) with no tense bonds (in red) at all and the nodes sit on a simple cubic lattice (Fig. 6.5e left panel). As shown in the right panels of Fig. 6.5e, under anti-correlated susceptible motor kicks, the active nodes (those with motor-attached bonds; shown as red spheres) begin to aggregate and tend to separate from the passive nodes (those with no motor-attached bonds; shown as blue spheres). The corresponding network structure exhibits clumps of floppy bonds (concentrated short green lines) connected by tense bonds (long red lines). The overall rigidity of the structure is protected by susceptible motors which tune the balance between local bond contraction and

neighboring bond stretching such that energetically unfavorable tense states are avoided.

The arrested phase separation builds up as follows: Susceptible motors enhance the potential gradient via an (s-dependent) effective temperature, since $T_{\text{eff}} < T$ along the kicking direction if $s > 1/2$. This leads to an enhanced long-range attraction and thus strengthens the initial trend of aggregation among the motor-bonded nodes. The motor-induced short-range attraction then efficiently makes the aggregates become compact, yielding a phase separation of an initially homogeneous structure into node-rich and node-poor regions. In analogy to the nucleation of liquid drops within an initially homogeneous gas, where large surface tension serves as the driving force to form a bulk condensed phase, in our picture, local aggregates correspond to the droplets of the condensed phase whereas the stretched bonds connecting the aggregates contribute to the surface tension. Therefore, an ensuing coarsening process serves to reduce the surface area via coalescence of local aggregates into larger condensates. Once a *balance* between local bond contraction and neighboring bond stretching (given a force-percolating network structure) is achieved, the coarsening process stops and the structure does not evolve any further (as reflected in the plateau of the aggregation strength shown in Fig. 6.5d inset). The system ends up with an arrested heterogeneous structure with compact aggregates/dense clumps coexisting with voids/dilute regions (Fig. 6.5e right panels); only moderate fluctuations about the arrested structures have been observed. Therefore, local force asymmetry is necessary for the initiation of phase separation while force percolation is essential for achieving global balance and thus the eventual arrest.

In Fig. 6.6 we demonstrate how the concentration P_a (and thus the cooperativity) of susceptible motors ($s = 1$) affects the tenseness and structural organization of the network. Parameters are chosen such that the system is in the regime of arrested phase separation at sufficiently high P_a. Shown in panel (a), the overall trend of a decrease in the fraction of taut bonds as P_a is raised is apparent. This results from increasing cooperativity in local force generation. Particularly noteworthy, however, is the presence of a kink near $P_a = 0.7$, which separates two

descending branches (I: $P_a = 0.5$–0.7 and II: $P_a = 0.8$–1 as marked in the figure). In stark contrast, the aggregation strength (i.e. the amplitude of the first peak of the radial distribution function) exhibits a highly *non-monotonic* dependence on P_a, which is sharply peaked at $P_a = 0.6$ (see panel b). The total energy (not shown) shows a similar trend as P_a varies. To understand these trends, we visualize the steady-state bond structures and corresponding node configurations in panel (c). These simulated configurations reveal two distinct regimes characterized by different "strategies" to reduce the number of taut bonds: At intermediate motor concentrations (corresponding to branch I), as P_a rises, an increasing number of floppy bonds are formed at the aggregation centers, at the cost of fewer but even more strongly stretched inter-clump filaments due to more compact node aggregation, as most clearly seen for $P_a = 0.6$ in panel (c), where the corresponding aggregation strength of nodes reaches its peak value (indicated by arrow). At sufficiently high motor concentrations (branch II), however, cooperative motor processes tend to minimize the overall tenseness by buckling as many bonds as possible at the same time avoiding too strong stretching. The resulting structure is thus rich in *moderately buckled* bonds and consists of large floppy clumps connected by sparse tense bonds (see $P_a = 1$ case in panel c). The aggregation strength decreases with increasing P_a in this highly cooperative regime. Such an interesting dependence of structural development on motor concentration vividly demonstrates the intricate interplay of local force generation and collective motor action.

Effective attraction

To demonstrate the effect of motor-induced short-range attraction, we choose a network connectivity that is below the percolation threshold ($P_c = 0.2$). In the absence of global force percolation, when driven by spatially anti-correlated motors kicks, the initially homogeneous and entirely floppy network (Fig. 6.7c upper left panel) develops into isolated floppy clumps (Fig. 6.7c lower panels), regardless of motor susceptibility. Under susceptible motor kicks ($s = 1$), it becomes evident that further contractions of the already buckled bonds (with typical spots marked by circles in Fig. 6.7c lower left panels) arise solely from the effective

short-range attraction due to motor processes. On the other hand when driven by load-resisting motors ($s = -0.5$), the anti-correlation in movements causes collapse of the transiently stretched bonds (Fig. 6.7c lower right panels). Adamant motor kicks ($s = 0$) lead to a similar transient structure (with fewer tense bonds though) and the eventual collapse (Fig. 6.7c lower middle panels). Therefore in a non-percolating network driven by anti-correlated kicks, despite the very different dynamics due to differing motor susceptibility, similar steady state structures are reached. The complete collapse of all the individual clumps is characterized by a vanishing total potential energy after the initial transients (Fig. 6.7a) and a significant aggregation strength that saturates to a steady-state plateau (Fig. 6.7b) once isolated condensates form.

In contrast, the control run with pure thermal motion presents a considerable fraction of taut bonds (Fig. 6.7c upper right panel) and thus maintains a finite potential energy (grey curve in Fig. 6.7a). The bond structure and node configuration remain largely homogeneous, exhibiting modest density fluctuations and a vanishingly small aggregation strength (grey curve in Fig. 6.7b).

Note that the illustrations for effective attraction shown here are obtained using fully stochastic simulations. The effective Brownian dynamics schemes give similar steady state structures composed of isolated floppy clumps only for susceptible motor kicking. For load-resisting motors that give rise to an effective long-range repulsion, however, a distinct behavior is seen (detailed below), highlighting the significance of correlation in motion for structural development.

Effective repulsion

Another interesting case arises when the motor susceptibility becomes negative. In this case a negative effective temperature yields an effective repulsion at sufficiently high motor activity (refer to Eqs. 6.21–6.22). As shown in Fig. 6.8(a), starting with an entirely floppy network (upper row), enhanced bond stretching coming from thermally induced fluctuations in bond length giving local force asymmetries, eventually gives rise to highly tense and ordered aster patterns (lower row) at steady state. Aster formation occurs when the effective repulsion that promotes

node separation and thus bond stretching dominates over the effective attraction that drives the opposite; removal of the short-range effective attraction does not affect aster formation, but indeed does disrupt efficient aggregation (see Fig. 6.11e). Consistent with our earlier results for *uncorrelated* kicks [12], the effective Brownian dynamics simulations also give sustained aster patterns. These patterns cannot collapse due to the absence of pairwise anti-correlation in motion; since at each move in Brownian dynamics, an individual node sees only an effective potential due to *all* its neighbors, the pairwise correlation is virtually lost. Such pairwise anti-correlation is crucial for active contractility as we showed elsewhere [24]. This anti-correlation, however, is captured by complete Monte Carlo simulations where anti-correlated move pairs are treated as reaction channels and executed at each MC step.

Fig. 6.8 also highlights the architectural and dynamical ingredients required for the formation of connected tight asters that consist of tense bundles radiating from the common center. Panel (a) illustrates the necessity of a sufficient network connectivity for force transmission and bundle compaction; at low connectivity (Fig. 6.8a left) only individually separate tense bundles are formed. Panel (b) depicts that a high motor kicking rate is needed to defeat thermal spreading and thus to facilitate filament or bundle alignment.

Aster formation finds a natural explanation in our model when we use the notion of the effective long-range repulsion that we have derived. In Fig. 6.9 we show the mean-field indications, obtained by SCP calculations (described in section II.C), of how the concentration (P_a) of load-resisting ($s = -0.5$) motors affects the long-range interactions. As clearly seen in panel (b), as P_a increases the long-range attraction due to bond stretching considerably weakens. Accordingly, the localization strength α of individual nodes (panel a) and the tension ($-p$) within the network (panel c) are both strongly suppressed. At $P_a = 0.8$, the profile of the effective potential becomes almost flat at large distances (red arrow in panel b), indicating a vanishing restoring force. Consistently, α becomes vanishingly small at large R (panel a) and the overall tension decays to zero (red arrow in panel c), because the bond constraints are hardly felt when load-resisting motors

counteract the tendency to contract. Yet higher motor concentration still enhances the effective short-range attraction (small-R region in panel c) as expected.

Effect of motor activity and susceptibility in phase separation: mean-field indications

By performing the self-consistent phonon calculation, we find mean-field indications for the phase separation observed in the simulations and experiments. In particular, such calculation allows us to examine how the changes in motor activity affect the tendency to phase separate which can be tested against simulations. We choose the length unit to be 100σ (such that the excluded volume effect plays a negligible role in phase separation) and vary the mean separation R between the nearest neighbors, i.e. the lattice spacing of the simple cubic lattice.

At sufficiently high motor susceptibility ($s > 0$ for $\Delta = 1$; Fig. 6.10b lower panel), we observe a non-monotonic dependence of the tension ($-p$), i.e. negative pressure, on the mean separation R, clearly indicating the necessity of some kind of phase separation into node-rich and node-poor regions.

For susceptible motors with $s = 1$ (Fig. 6.10a), varying the motor activity Δ affects *both* the short-range (small R) and the long-range (large R) attractions: increasing motor activity (as indicated by dashed arrows) leads to stronger localization of individual nodes (upper panel) and a larger tension in favor of stronger aggregation (lower panel). In particular at small R where the bonds are buckled, effective attraction arising from motor-driven contractions ($\sim \Delta \log r$) dominates, yielding further aggregation of the loosely connected nodes. This behavior is most clearly manifested for a sparsely connected network where lack in bond constraints allows the formation of isolated aggregates, as shown earlier in Fig. 6.7c.

Using Brownian dynamics simulations, we study the dependence of aggregation strength upon motor activity for force-percolating networks ($P_c = 0.4$). The statistical measures and steady-state structures (labeled by T_{eff}/T) are displayed in Fig. 6.11. Increasing motor kicking rate κ (note $\Delta \propto \kappa$) apparently enhances the trend toward phase separation (panel d) and promotes stronger aggregation (panel c and d), supporting the mean-field prediction. Both the fraction of taut

bonds (panel a) and the total energy (panel b) decrease with increasing kicking rate due to a lower T_{eff}.

As we pointed out earlier in deriving the effective pair potential, varying motor susceptibility s affects *only* the long-range interaction (via $\boldsymbol{T}_{\text{eff}}$), as shown in Fig. 6.10b. For a given lattice spacing, increasingly susceptible motors (indicated by dashed arrows) drive stronger attraction (lower panel) and enhance localization of individual nodes (upper panel), as well as yield a stronger tendency for phase separation, as reflected in the increasingly non-monotonic dependence of the tension on density change as s increases (lower panel).

Self-consistent phonon calculations also allow us to determine a quasi-thermodynamic stability diagram. In Fig. 6.12 we present the stability diagram in the P_c-P_a parameter plane for susceptible ($s = 1$), adamant ($s = 0$) and load-resisting ($s = -0.5$) motors. Below the stability boundaries (colored lines), the pressure depends non-monotonically on the mean particle separation. This indicates the tendency toward phase separation. Above the boundaries, there are no stable α solutions , or that the tension (or negative pressure) decreases monotonically with increasing particle separation. As the motor susceptibility increases, the instability region (shaded area) expands toward lower P_c and higher P_a, suggesting that susceptible motors promote phase separation. Since motor susceptibility affects only the long-range interaction via T_{eff} at high P_c, where bond stretching stabilizes finite α solutions, small or negative s may lead to an effective repulsion that counteracts the trend of attraction thus eliminating the non-monotonicity in pressure, or else destabilizes α solutions by offsetting the restoring force. Consequently, the stability boundary at large P_c shifts toward lower P_a as s decreases.

To determine whether the non-monotonicity in pressure indeed corresponds to phase separation, we need to examine heterogeneous/site-dependent α solutions; a bimodal distribution of stable α values would then indicate that localized dense regions phase separate from mobile dilute regions. We hope to investigate this aspect in an upcoming work and thus provide more quantitative arguments for the surface tension associated with stretched bonds connecting floppy clumps. Such an analysis should allow us to determine the "droplet" size for the condensed phase

when bond-constraint-induced arrest occurs.

To summarize our results in Fig. 6.13 we outline the diverse patterns formed at various network connectivity (P_c) for susceptible ($s > 0$) and load-resisting ($s < 0$) motors. This figure delineates where there are contrasting results from complete MC simulations to those obtained from BD simulations using the effective pair interaction. As we mentioned before, the Monte Carlo schemes explicitly incorporate pairwise anti-correlation by treating move pairs as reaction channels, while in the effective Brownian dynamics schemes the total effective potential acting on individual nodes from all the neighbors smears out the pair correlation. This disparity between the predictions of the two schemes does not affect the active patterning by susceptible motors (Fig. 6.13a). In that case the effective attraction provides the dominant mechanism for aggregation and phase separation. MC and BD simulations give converging results: Below the percolation threshold (marked by the vertical line) isolated floppy clumps form, whereas at intermediate P_c above the threshold arrested phase separation occurs. For load-resisting motors (Fig. 6.13b), however, correlation in motion plays a key role in structural development, because in this case an effective long-range repulsion dominates over the short-range attraction and governs the pattern formation. Anti-correlation in movements gives rise to collapse of the tense intermediates which is essential for active contractility/macroscopic contraction [24]. If there is no anti-correlation collapse does not occur. As a result, the tense bundles (for non-percolating case) and connected asters (for percolating case) are maintained as long-time steady state structures. At sufficiently high connectivity, the bond constraints are too strong to allow significant local force asymmetry, thus a balanced tug-of-war between motor-attached filaments prevents the formation of heterogeneous cluster structures, and instead leads to a largely homogeneous structure with moderate fluctuations (rightmost regime in both panels a and b), regardless of the motor susceptibility or correlation in motion.

Also we note that the Brownian dynamics simulations for load-resisting motors exhibit similar behavior to that coming from uncorrelated isotropic kicks as we studied earlier [12]: Both simulations generate sustained aster patterns that

do not collapse, exemplifying a negative effective temperature. For susceptible motors, however, the dependence of T_{eff} and the effective attraction on the instantaneous local network structure hinders the system from achieving global concerted movement. There is thus no spontaneous flow or oscillating behavior that presents for the uncorrelated kick case [12]. A similar absence of a flow transition has also been found for a contractile nematic model recently studied analytically [25] and numerically [26].

6.4 Conclusion and discussion

We are now in a position to recapitulate how the intricate interplay between local force generation, network connectivity and collective action of motors gives rise to regular and heterogeneous patterns, arrested coarsening and macroscopic contraction: A sufficient connectivity is required for forces to percolate so that local motor-induced stresses and resulting deformations can propagate significant distances through the network. Given a force-percolating structure, downhill-prone motors yield heterogeneous/disordered cluster structures, exemplified as an arrested phase separation in the absence of bond or motor rupture events; whereas load-resisting motors may drive large-scale contraction by surmounting a high energy barrier constituted by tense intermediates. Anti-correlation in movements is essential for collapse of the intermediate tense states in approach to the eventual large-scale contraction; in the absence of correlation in movements, as is the case for Brownian dynamics simulations and for our earlier studies on uncorrelated kicks [12], the stretched bundles cannot collapse and no contractile structures result, thus the aster pattern is maintained as the steady-state structure.

The notion of effective interaction provides a natural explanation for the aggregation and coalescence of actomyosin condensates: enhanced long-range attraction facilitates initial density fluctuations; effective attraction at short distances especially in the buckling regime, arising purely from motor-driven contractions, then promotes efficient aggregation by drawing nearby nodes or condensates even closer. Whereas an effective repulsion can originate from a negative motor suscep-

tibility, and in turn a negative effective temperature allows the formation of aster patterns in the absence of correlation in node movements.

Our finding may suggest a new mechanism for aggregation of active gels: local force asymmetry and disorder (structurally inherent or thermally generated) trigger local aggregation which is further enhanced by an effective attraction due to correlated motor kicks; force percolation combined with the tendency to reduce surface tension associated with the stretched bonds leads to coarsening of local aggregates; when the balance between local bond collapse and neighboring bond stretching is reached, the system forms an arrested structure composed of floppy clumps connected by tense bonds. The pertinent dynamic process involves phase separation into node-rich and node-poor regions followed by arrest due to bond constraints.

We also generalize the concept of effective temperature to non-equilibrium many-body systems driven by *correlated* small-step motor kicking events. Explicit simulation tests lend support to the validity of picturing such systems as being at an effective equilibrium with modified interactions.

Chapter 6, in full, is a reprint of the material as it appears in the Journal of Chemical Physics **136** 145102 (2012), S. Wang and P. G. Wolynes. The dissertation/thesis author was the primary investigator and author of this paper.

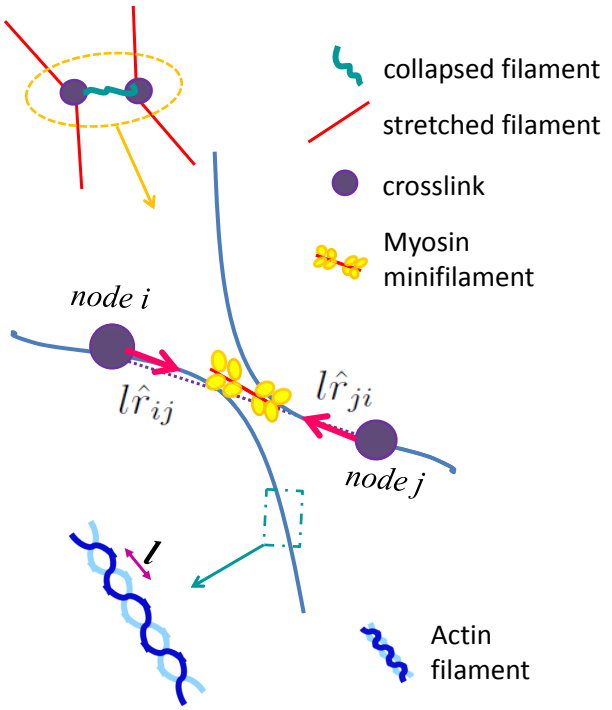

Figure 6.1: Schematic illustration of the spatially anti-correlated kicks acting on motor-bonded node pairs. (Central image) A bipolar myosin minifilament pulls in slack locally, generating a pair of equal size (l) but oppositely directed displacements (red arrows) at the motor-bonded nodes (purple spheres) along their line of centers, where $\hat{r}_{ij}$ is a unit vector pointing from node i to node j. Upon zoom-out, this represents a typical functional unit (marked by a dashed circle in the top image) that generates incremental contractions within a crosslinked filamentous network. An enlarged view of the actin filament (bottom image) reveals its segmented structure. The size l of the subunits determines the magnitude of the relative node displacements due to contraction events of myosin sliding. l is thus taken to be the step size of anti-correlated kicks in our model.

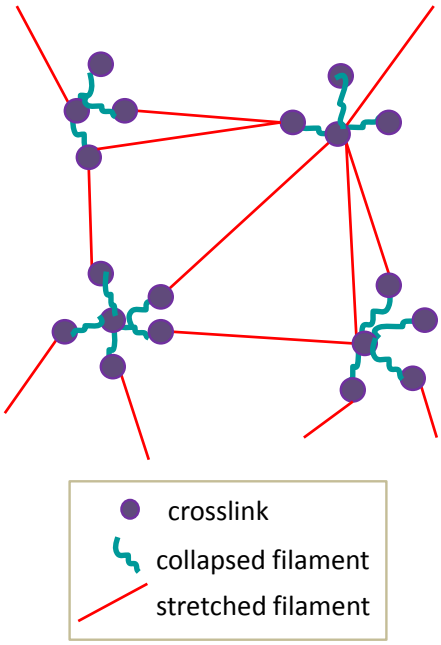

Figure 6.2: Cartoon of the tensegrity structure composed of collapsed and stretched elements. In a crosslinked network of filaments, active filament sliding is stabilized by passive crosslinking. A tensegrity structure is formed once a global balance between local contraction and neighboring bond stretching is achieved. An initially homogeneous network then develops into dense floppy clumps (concentrated green wiggly lines) connected by highly stretched filaments (long red straight lines).

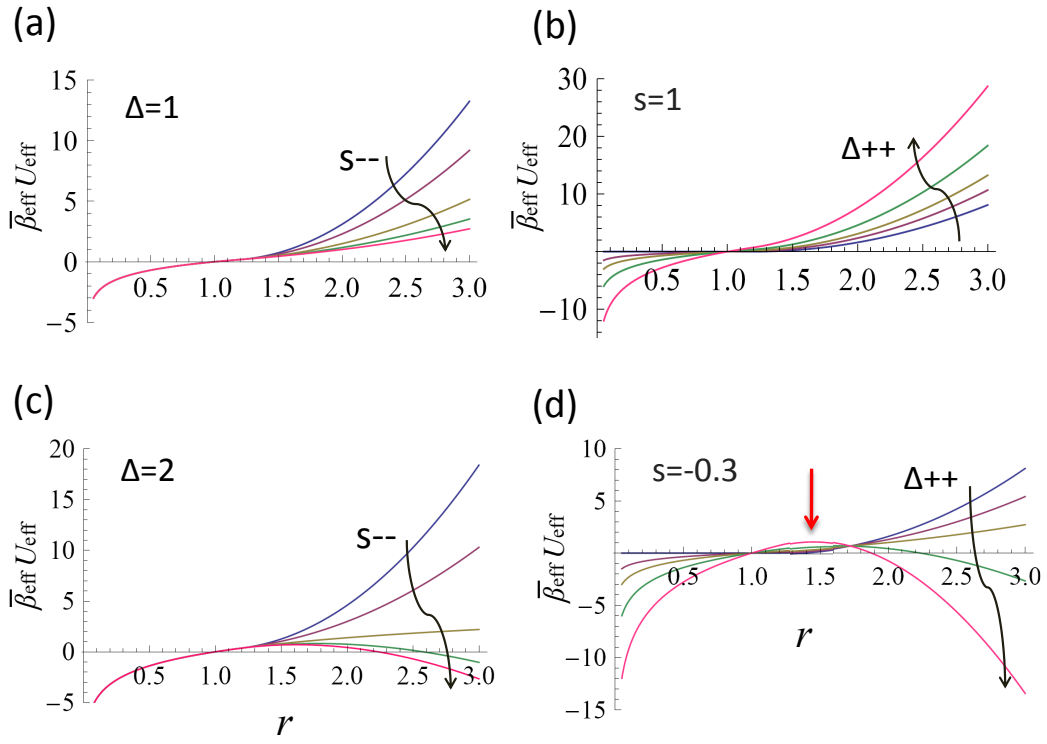

Figure 6.3: Profile of the modified interaction given by the pair-level steady-state solution. We plot the effective interaction $U_{\rm eff}$ (Eq. 6.21) scaled by effective temperature $\bar{\beta}_{\rm eff}^{-1}$ (Eq. 6.22) for various motor activity (Δ) and susceptibility (s). At sufficiently high activity, load-resisting ($s = -0.3$) motors may yield a long-range effective repulsion, an energy barrier (indicated by a red arrow in panel d) thus appears at intermediate distances, suggesting the tendency for node separation and thus the bond stretching that occurs in aster formation. (a) and (c): $s = 1, 0.5, 0, -0.2$ and -0.3. (b) and (d): $\Delta = 0, 0.5, 1, 2$ and 4. Common parameters are $L_e = 1.2, \beta\gamma = 5, P_c = 0.4$, and $P_a = 1$.

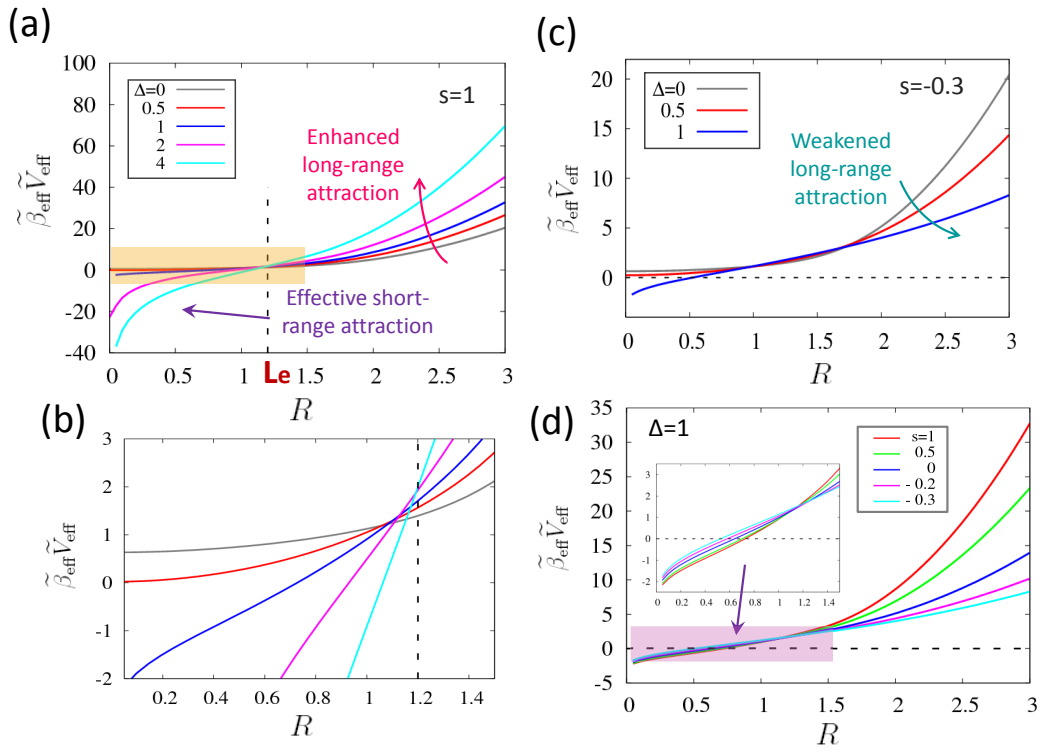

Figure 6.4: Profile of the effective pair interaction (Eq. 6.26) obtained by the self-consistent phonon calculation. (a) Susceptible motors ($s = 1$) with increasing activity Δ enhance the long-range attraction and strengthen the short-range effective attraction. (b) A zoom-in view of the small-R region close to the elasticity onset (dashed line) in panel (a) showing the absence of kink or inflection point in the potential profile. (c) Adamant motors ($s = -0.3$) weaken the long-range attraction. No stable α solution is found if the motor activity gets too high ($\Delta > 1$). (d) Varying motor susceptibility does not affect the short-range effective attraction (inset), but increasingly susceptible motors (bottom to top) lead to a stronger long-range attraction. Common parameters are $L_e = 1.2, \beta\gamma = 5, P_c = 0.4, P_a = 1$.

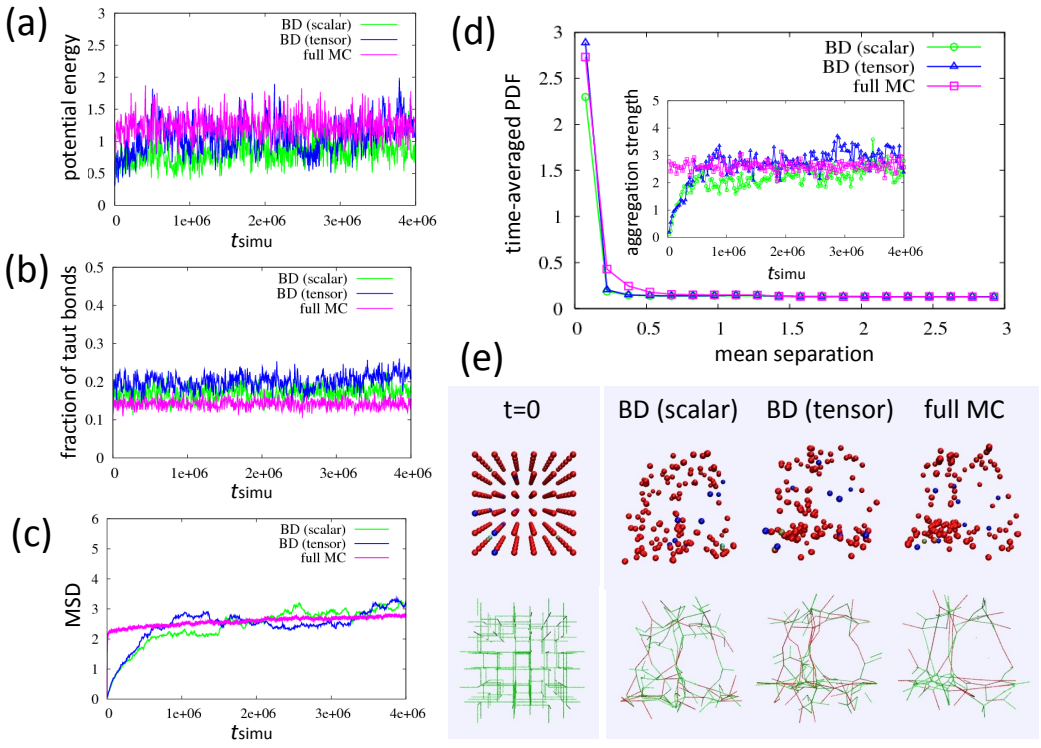

Figure 6.5: Testing the validity of the effective equilibrium approximation: a comparison of three simulation schemes. Statistical characteristics and steady-state structures for a partially and randomly connected ($P_c = 0.4$) network built on a simple cubic lattice driven by small-step ($l = 0.03$) susceptible ($s = 1$) motors are shown. (a) The potential energy; (b) the fraction of taut bonds; (c) the mean square node displacement; (d) main: the pair distribution function (PDF) averaged over a wide steady-state time window; inset: the aggregation strength, which is the height of the innermost peak of the PDF, versus simulation time; (e) initial (left) and steady-state (right) node configurations (upper row) and corresponding bond structures (lower row). The parameters chosen for illustration are $L_e = 1.2, \beta\gamma = 5, P_a = 1$, and $\kappa = 1$.

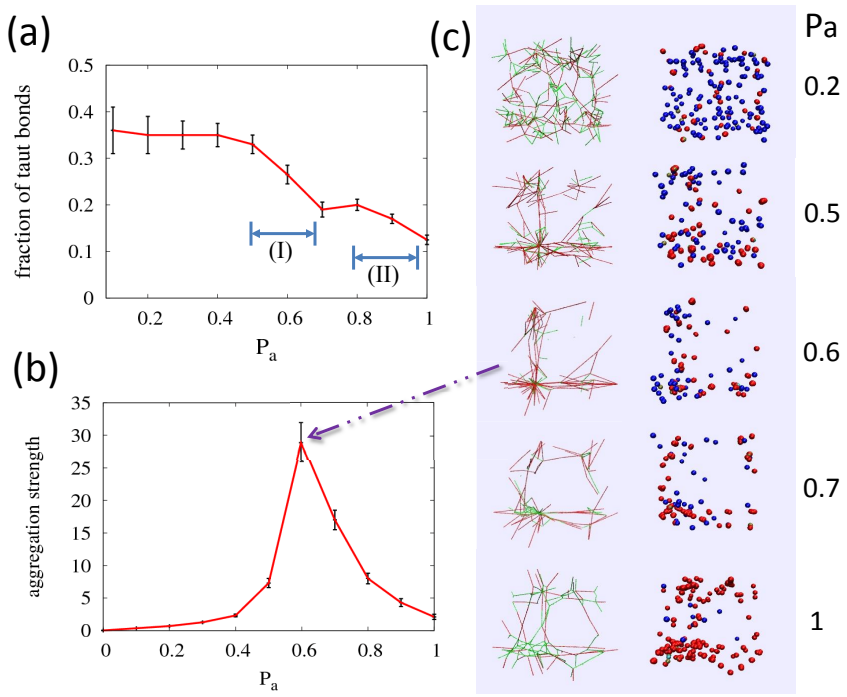

Figure 6.6: The dependence of network tenseness and structure on motor concentration (P_a) obtained by Monte Carlo simulations. The parameters were chosen such that the system is in the regime of arrested phase separation. (a) The fraction of taut bonds decreases as P_a increases. A kink located around $P_a = 0.7$ separates two descending branches: (I) $P_a = 0.5$–0.7 and (II) $P_a = 0.8$–1. (b) The aggregation strength exhibits a sharp peak at $P_a = 0.7$. The error bars in (a) and (b) depict standard deviations from averages over a steady-state time window of 4×10^6 Monte Carlo steps. (c) Bond structures and corresponding node configurations at various P_a values are shown, from top to bottom $P_a = 0.2, 0.5, 0.6, 0.7$ and 1. The arrow indicates the bond structure with the strongest aggregation. The remaining simulation parameters are $L_e = 1.2, \beta\gamma = 5, P_c = 0.4, l = 0.05, s = 1$, and $\kappa = 0.1$.

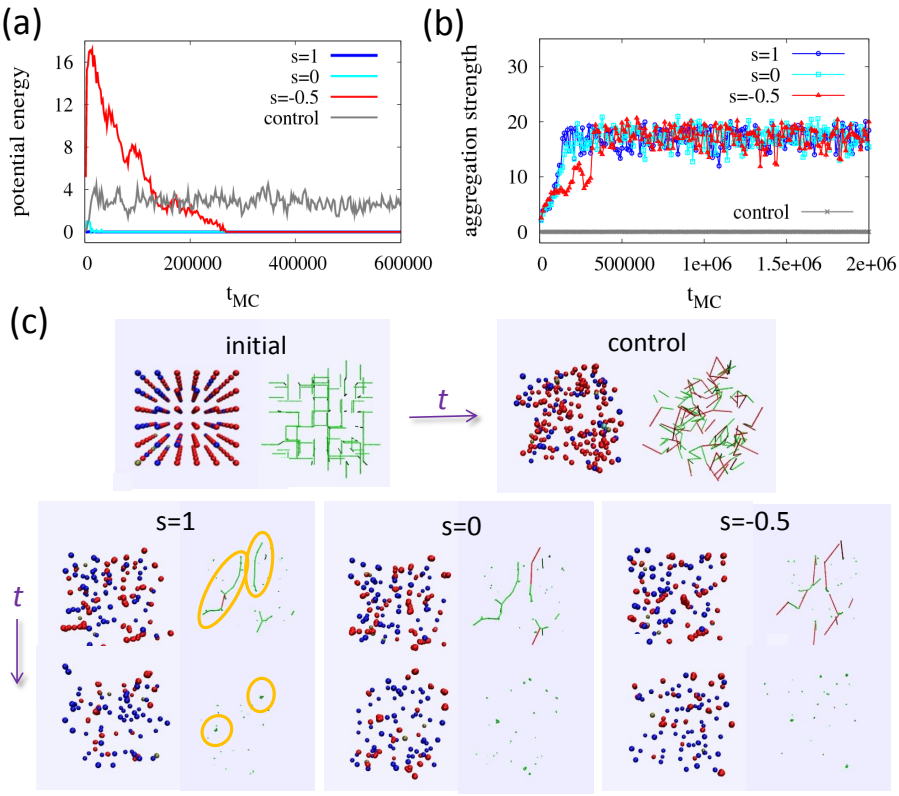

Figure 6.7: An illustration of the motor-induced effective attraction for a non-percolating network ($P_c = 0.2$) at various motor susceptibilities. (a) The potential energy; (b) the aggregation strength; (c) initial (upper left) and later node configurations and bond structures for a control run with pure thermal motion (upper right), and for motorized systems with $s = 1$ (lower left), $s = 0$ (lower middle) and $s = -0.5$ (lower right). Despite having different dynamics, similar steady-state structures with isolated floppy clumps are reached in each case, regardless of the motor susceptibility. The remaining simulation parameters are $L_e = 1.2, \beta\gamma = 5, P_a = 1, l = 0.03$, and $\kappa = 0.1$.

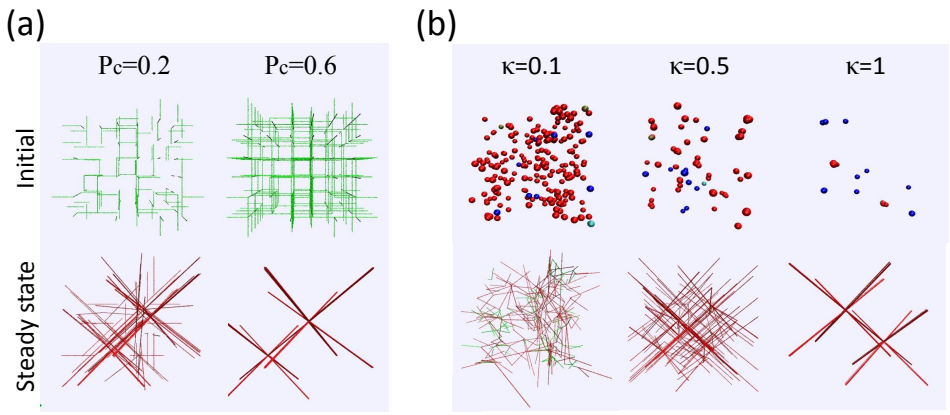

Figure 6.8: An illustration of the motor-induced effective repulsion caused by load-resisting ($s = -0.5$) motors for various network connectivities and motor kicking rates. (a) Initial (upper) and steady-state (lower) bond structures are shown at low (left: $P_c = 0.2$) and at high (right: $P_c = 0.6$) connectivity with $\kappa = 1$. (b) Node configurations (upper) and corresponding bond structures (lower) at various motor kicking rates (left to right: $\kappa = 0.1, 0.5$, and 1) with $P_c = 0.4$. The common set of simulation parameters are given by $L_e = 1.2, \beta\gamma = 5, P_a = 1$, and $l = 0.05$.

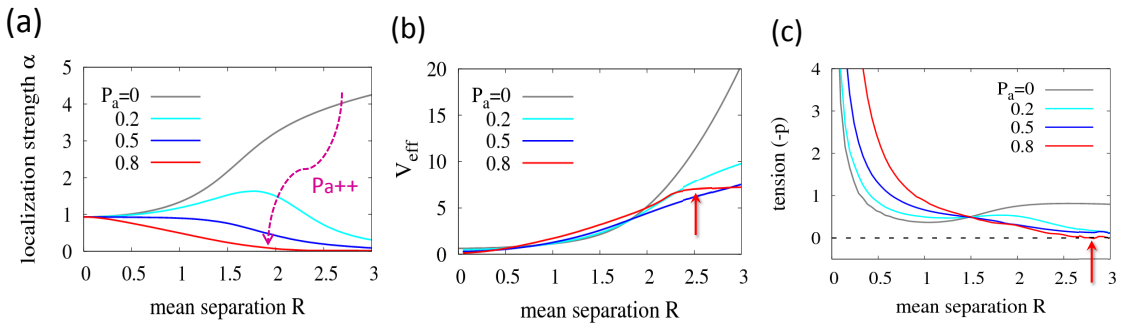

Figure 6.9: Mean-field predictions of the effect of the concentration (P_a) of load-resisting ($s = -0.5$) motors on long-range interactions. (a) The localization strength α of individual nodes. The localization at large separation R is considerably suppressed as P_a increases. (b) The effective potential. Increasing P_a weakens the long-range attraction; the potential profile actually flattens out (red arrow) at $P_a = 0.8$ indicating a vanishing restoring force. (c) The overall tension ($-p$) vanishes at large R (red arrow) for high P_a. This suggests the tendency for contraction is counterbalanced by a motor-induced long-range repulsion. The simulation parameters are $L_e = 1.2, \beta\gamma = 5, P_c = 0.4$ and $\Delta = 1$.

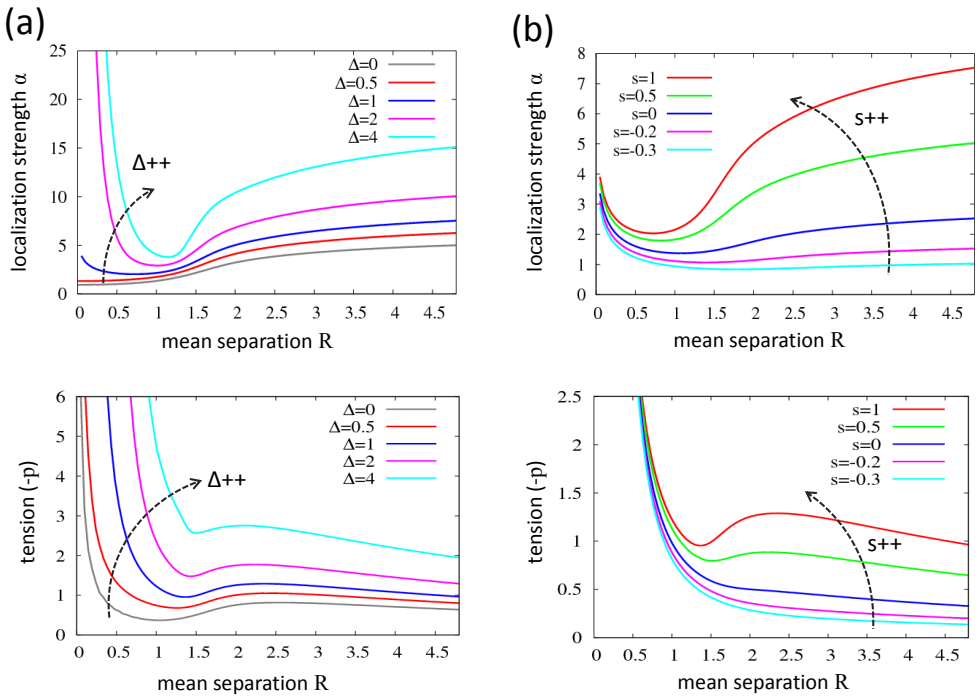

Figure 6.10: The effect of motor activity (Δ) and susceptibility (s) on phase separation. Shown are the calculated localization strength α (upper row) and the tension ($-p$) (bottom row) as a function of the mean separation R for (a) $s = 1$ with various motor activities, $\Delta = 0, 0.5, 1, 2$, and 4 (bottom to top), and (b) $\Delta = 1$ with various motor susceptibilities, $s = -0.3, -0.2, 0, 0.5$, and 1 (bottom to top). The remaining simulation parameters are $L_e = 1.2, \beta\gamma = 5, P_c = 0.4$, and $P_a = 1$.

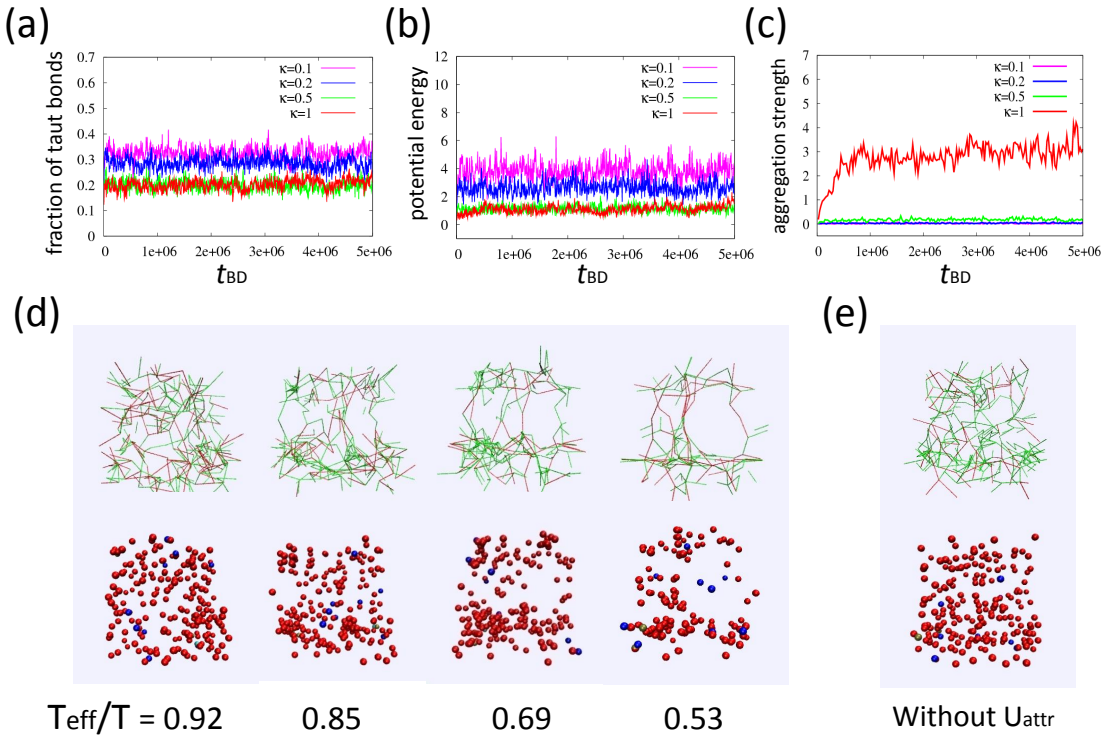

Figure 6.11: The role of motor kicking rate and effective attraction in aggregation. (a)–(c) Statistical measures for the dynamic and structural development at various motor kicking rates. Steady-state bond structures (upper) and node configurations (lower) are shown at increasing motor kicking rates (d): from left to right $\kappa = 0.1, 0.2, 0.5$ and 1 (converted into T_{eff}/T), and for corresponding models without motor-induced short-range attraction at $\kappa = 1$ (e). The remaining simulation parameters are $L_e = 1.2, \beta\gamma = 5, P_c = 0.4, P_a = 1, s = 1$, and $l = 0.03$.

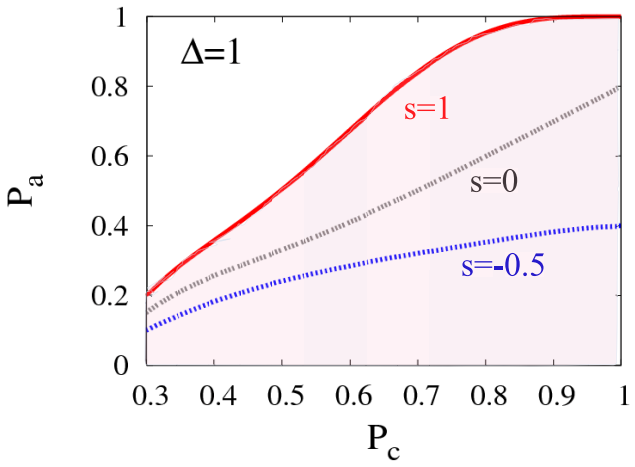

Figure 6.12: The stability diagram at various motor susceptibilities. The colored lines represent the stability boundaries, solid red for $s = 1$, dashed grey for $s = 0$ and dotted blue for $s = -0.5$. Below the stability boundaries the pressure exhibits a non-monotonic dependence on particle separation indicating the tendency toward phase separation. The instability region (shaded area) extends to lower P_c and higher P_a as s increases, suggesting that susceptible motors promote phase separation. The remaining simulation parameters are $L_e = 1.2, \beta\gamma = 5$, and $\Delta = 1$.

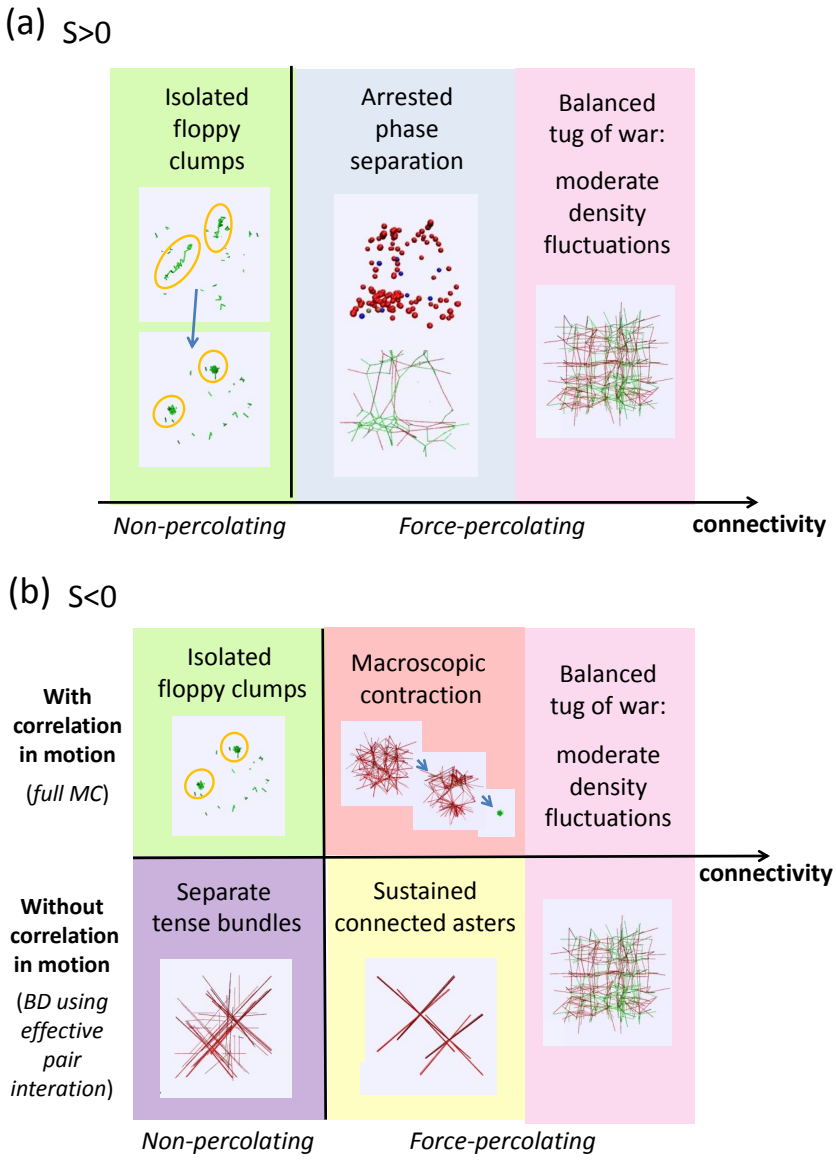

Figure 6.13: Patterns of behavior for susceptible ($s > 0$) and load-resisting ($s < 0$) motors at a high motor concentration. Typical structures generated by simulations are shown for each situation. The horizontal axis indicates increasing network connectivity from left to right. The vertical line locates the percolation threshold. (a) For susceptible motors, effective Brownian dynamics simulations and Monte Carlo simulations give similar results. At intermediate connectivity above the percolation threshold, arrested phase separation occurs. (b) For load-resisting motors, (anti-)correlation plays a key role in the active patterning. Macroscopic contraction occurs only in the presence of anti-correlation in motion, otherwise connected asters form that cannot collapse.

Bibliography

[1] Howard, J. *Mechanics of Motor Proteins and the Cytoskeleton*, (Sinauer Assoc., Sunderland, MA, 2001).

[2] Martin, A. C., Kaschube, M. & Wieschaus E. F. Pulsed contractions of an actin-myosin network drive apical constriction. *Nature* **457,** 495–499 (2009).

[3] Mason, F. M. & Martin, A. C. Tuning cell shape change with contractile ratchets. *Curr. Opin. Genet. Dev.* **21,** 671–679 (2011).

[4] Silva, M. S., Depken, M., Stuhrmann, B., Korsten, M., MacKintosh, F. C. & Koenderink, G. H. Active multistage coarsening of actin networks driven by myosin motors. *Proc. Natl. Acad. Sci. USA* **108,** 9408–9413 (2011).

[5] Surrey, T., Nédélec, F., Leibler, S. & Karsenti, E. Physical properties determining self-organization of motors and microtubules. *Science* **292,** 1167–1171 (2001).

[6] Backouche, F., Haviv, L., Groswasser, D. & Bernheim-Groswasser, A. Active gels: Dynamics of patterning and self-organization. *Phys. Biol.* **3,** 264–273 (2006).

[7] Munro, E., Nance, J. & Priess, J. R. Cortical flows powered by asymmetrical contraction transport PAR proteins to establish and maintain anterior-posterior polarity in the early *C. elegans* embryo. *Dev. Cell* **7,** 413–424 (2004).

[8] Köhler, S., Schaller, V. & Bausch, A. R. Structure formation in active networks. *Nat. Mater.* **10,** 462–468 (2011).

[9] Shen, T. & Wolynes, P. G. Statistical mechanics of a cat's cradle. *New J. Phys.* **8,** 273 (2006).

[10] Wang, S., Shen, T. & Wolynes, P. G. The interplay of nonlinearity and architecture in equilibrium cytoskeletal mechanics. *J. Chem. Phys.* **134,** 014510 (2011).

[11] Wang, S. & Wolynes, P. G. Effective temperature and glassy dynamics of active matter. *J. Chem. Phys.* **135,** 051101 (2011).

[12] Wang, S. & Wolynes, P. G. On the spontaneous collective motion of active matter. *Proc. Natl. Acad. Sci. USA* **108,** 15184–15189 (2011).

[13] Janmey, P. A., McCormick, M. E., Rammensee, S., Leight, J. L., Georges, P. C. & MacKintosh, F. C. Negative normal stress in semiflexible biopolymer gels. *Nat. Mater.* **6,** 48–51 (2007).

[14] MacKintosh, F. C. & Levine, A. J. Nonequilibrium mechanics and dynamics of motor-activated gels. *Phys. Rev. Lett.* **100,** 018104 (2008).

[15] Levine A. J. & MacKintosh, F. C. The mechanics and fluctuation spectrum of active gels. *J. Phys. Chem. B* **113,** 3820–3830 (2009).

[16] Zaccarelli, E. Colloidal gels: equilibrium and non-equilibrium routes. *J. Phys.: Condens. Matter* **19,** 323101 (2007).

[17] Foffi, G., De Michele, C., Sciortino, F. & Tartaglia, P. Arrested phase separation in a short-ranged attractive colloidal system: A numerical study. *J. Chem. Phys.* **122,** 224903 (2005).

[18] Bendix, P. M., Koenderink, G. H., Cuvelier, D., Dogic, Z., Koeleman, B. N., Briehera, W. M., Fielda, C. M., Mahadevan, L. & Weitz, D. A. A quantitative analysis of contractility in active cytoskeletal protein networks. *Biophys. J.* **94,** 3126–3136 (2008).

[19] Wolynes P. G. & Deutch, J. M. Dynamical orientation correlations in solution. *J. Chem. Phys.* **67,** 733 (1977).

[20] Brangwynne, C. P., Koenderink, G. H., MacKintosh, F. C. & Weitz, D. A. Cytoplasmic diffusion: molecular motors mix it up. *J. Cell Biol.* **183,** 583–587 (2008).

[21] Fixman, M. Highly anharmonic crystal. *J. Chem. Phys.* **51,** 3270 (1969).

[22] Ermak D. L. & McCammon, J. A. Brownian dynamics with hydrodynamic interactions. *J. Chem. Phys.* **69,** 1352–1360 (1978).

[23] Gillespie, D. T. A general method for numerically simulating the stochastic time evolution of coupled chemical reactions. *J. Comp. Phys.* **22,** 403–434 (1976).

[24] Wang, S. & Wolynes, P. G. Active contractility in actomyosin networks. *Proc. Nat. Acad. Sci. USA* **109,** 6446–6451 (2012).

[25] Liverpool, T. B. & Marchetti, M. C. A general method for numerically simulating the stochastic time evolution of coupled chemical reactions. *Phys. Rev. Lett.* **97,** 268101 (2006).

[26] Cates, M. E., Fielding, S. M., Marenduzzo, D., Orlandini, E. & Yeomans, J. M. Shearing active gels close to the isotropic-nematic transtion. *Phys. Rev. Lett.* **101,** 068102 (2008).

Chapter 7

Conclusion and outlook

The cytoskeleton is a remarkably rich system. This heterogeneous yet structured motor-filament assembly bathed in water allows eukaryotic cells to replicate, repair themselves, move, respond to stimuli, and communicate with their neighbors in a multicellular organism. We are attempting to discover the concepts needed to think about the dynamics and structure of this versatile "muscle" of the living cell. To this end, we have constructed minimal physical models and asked rather general questions rather than try to model the cytoskeleton with all its biological complexity. As shown in the preceding chapters, our microscopic models that incorporate the essential aspects of biological relevance indeed capture, at least qualitatively, a rich variety of experimental observations in vitro and in vivo. These observations range from the formation of diverse functional patterns (such as sustained asters and heterogeneous condensates) to active contractility and spontaneous flow. Moreover, we have demonstrated the validity of using the concepts of effective temperature and effective motor-induced interactions in describing steady state and responses of weakly motorized systems in a quasi-equilibrium framework. Somewhat beyond the range of validity of this description, mean field theories combined with variational stability analysis revealed how active mechanisms allow for collective directed motion to occur as an emergent phenomenon reflecting broken symmetries. The rigidity of the macroscopically moving state, rather than being provided by quantum statistics as for superfluidity and superconductivity, arises from a cooperative action of load-sensitive active elements supported by a sustained

energy input in a well-connected structure. Despite these conceptual successes, our theory is not yet a complete theory for everything "cytoskeletal". The intricate biochemistry of real cytoskeleton necessitates a more quantitative account for the relative roles of physical interactions and biochemically regulated signaling which act in an intertwined manner. Trying to do this poses new challenges and yet calls forth new opportunities for theory. In the following I will discuss some possible extensions of our model and sketch how these immediate next-steps likely have intriguing consequences and should trigger novel mechanistic thoughts about the living cell.

In vitro structures studied experimentally are assembled irreversibly because these reconstitutions lack many of the in vivo protein factors that allow fast pattern renewals. In line with this fact our current model has assumed quenched network connectivity and motor distribution over the bonds. Yet the transient action of crosslinking proteins and the unbinding kinetics of motor proteins from the filaments, which must interplay with the intrinsic motor activity, may allow more efficient remodeling of living cells and lead to rich dynamical behavior described by several characteristic time scales. By introducing load-dependent bond rupture rate and motor detachment rate, we may study frequency-dependent rheological properties of the cytoskeletal network. Such rheological issues include how the motor kinetics affects the nonlinear elastic responses as well as the low-frequency stress fluctuations, or whether the balance between active sliding, passive crosslinking and forced unbinding can result in a nonequilibrium steady state exhibiting quasi-steady patterns.

The matching of times scales for a weak internal or external driving force with that for the intrinsic structural relaxation also brings the possibility of stochastic resonance [1], in which increased sensitivity of the system to small perturbations is achieved when an appropriate dose of noise is added. The enhanced response arises for the synchronization of noise-induced hopping among neighboring states in a multistable potential with the temporal profile of the weak perturbation. This information-transmitting phenomenon that exploits the noise in a self-optimizing manner may play a promising role in functioning of complex systems. By exam-

ining our systematic expansion scheme for the many-body master equation, we may look for the signatures of stochastic resonance, mainly delta spikes on the power spectral density and exponentially decaying peaks (with their orders) in the residence-time distribution, reflecting the synchronization aspect. The same principle may also be responsible for a thermal ratchet (i.e. a periodic structure with spatial asymmetry subjected to thermal noise) to rectify symmetric, unbiased nonequilibrium fluctuations into a directed current.

It is noted that filament treadmiling [2] also leads to center of mass motion of the filaments and thus generates discrete "kicks" on the nodes, though in this case the motor kicking rate would be proportional to the polymerization rate. The intriguing possibility that our findings may be relevant to treadmiling actomyosin systems and thus have implications for lamellipodium dynamics can be explored by extending our current model. The fluctuating cell membrane to which nonequilibrium polymerization is coupled might be modeled as a moving mechanical obstacle that the "polymerization motors" would sense and respond to.

Particles immersed in a fluid excite long-ranged flows as they move, and similarly move in response to fluid motion. By generating and reacting to a fluid's local velocity, particles experience hydrodynamic interactions with each other and with the walls of their container. It has been shown within a continuum framework that for active particles in a fluid, such as bacteria or collections of living cells, many of the large-scale nonequilibrium phenomena described in the literature can directly arise from the long-range nature of the hydrodynamic interactions among the active particles [3]. This medium-mediated coupling is not yet included in our model, but it can easily be done by incorporating an appropriately cross-correlated diffusion tensor to our Fokker-Planck equation description for Brownian dynamics. When combined with the correlated motor kicking events, we expect the hydrodynamic coupling would induce long-range velocity correlations and facilitate propagation of nearby motor kicks, thus leading to directed motion with pulsed contractions.

The excluded volume interactions among rod-shaped particles lead to orientational, liquid crystal ordering at high particle concentrations. We may extend

the self-consistent phonon theory to account for the spatial anisotropy in the pair interaction due to the particle shape. Specifically, in addition to the localization strength for the center of mass of the rods, we will need also to characterize separately the mechanical feedback strength for motions parallel and perpendicular to the long axis of the rods. The resulting self-consistent solutions should correspond to minima of the Onsager free energy for interacting rods [4].

For "living liquid crystals" composed of self-propelled particles modeled as orientated force dipoles, self-propulsion has been shown to enhance (by contractile "pullers", e.g. algae) or reduce (by extensile "pushers", e.g. most bacteria) the effective viscosity of the active particle suspension at zero shear rate [5]. These same rheological phenomena might be directly related to the sign of motor susceptibility in our models: susceptible motors with $s > 0$ lead to $T_{\text{eff}} < T$ or equivalently an enhanced viscosity; meanwhile a positive susceptibility corresponds to an effective attraction due to contractile subunits. The opposite applies to the $s < 0$ case. We note that the sign of s can be inferred at the single molecule level from the lifetime-force curve obtained by pulling experiments on single motor proteins such as kinesin. Increase (Decrease) in lifetime with increasing applied force would indicate a positive (negative) susceptibility, corresponding to catch (slip) bond behavior [6, 7].

In our earlier studies of a model actomyosin network as a motorized cat's cradle driven by anti-correlated kicks (Chapter 6), we have observed arrested phase separation in computer simulations where the motor-induced coarsening process stops once the local bond collapse balances the neighboring bond stretching. We have argued that force percolation combined with the trend to reduce surface tension associated with the stretched bonds leads to coarsening of local aggregates. We may further inquire as to how to analytically treat the bond constraints. Can they be characterized by a "stopping" term in the free energy functional that counteracts the tendency for a complete phase separation? One possibility is that surface tension that depends on the network connectivity flips sign as the "droplets" consisting of collapsed bonds grow up to a critical size. This mean-field level formulation can then be tested by comparing the estimated droplet size with the

simulation outcome.

In analogy to the force dipoles mimicking the myosin-driven relative sliding of neighboring actin filaments, there also exist torque dipoles [8] imitating the counter-rotation of two sides of the cell, originated from chiral asymmetry of individual actin filaments. We may thus introduce into our model anti-correlated rotations of motorized node pairs around their lines of centers. A similar master equation description for the active processes then should allow us to investigate the consequence of collective action of "chiral" motors, such as modifications to the rotational diffusion of the nodes as well as the possibility of spontaneous organized motion.

Recent experimental studies of F-actin driven chromosome transport [9] have suggested a novel intracellular "transport machine". In this model, force is generated by isotropic contractile activity distributed rather homogeneously throughout the F-actin meshwork. Although the intrinsic meshwork contraction lacks any specific directionality, anchoring of the meshwork to the cell cortex confers directionality to its large-scale motion. Finally, the contractile force is conveyed to cargo at least in part by steric entrapment of particles larger than the effective mesh-size of the network. Notably, in contrast to chromosome transport by microtubules, where re-establishment of severed microtubule-chromosome connections requires significant time and may result in chromosome loss, transport by a space-filling F-actin meshwork may be considerably more robust because of the physical entrapment within an extended meshwork. However, the experimental attempts to test the involvement of myosin motors in this process have remained inconclusive to date. We have performed stochastic simulations on a correlatedly motorized cat's cradle with free boundaries and observed isotropic contraction of the network. We may further fix a group of boundary nodes to mimic the mechanical anchoring and see whether an asymmetric contraction which is essential for the directional transport would indeed occur. Quantitative tests of our model would be provided by the experimentally measured contraction speed as a function of the initial distance from the anchoring position, which can readily be measured in our simulations. Interestingly, it has been seen that the *constant* poleward speed

of each chromosome depends *linearly* on its initial distance from the pole. This quantitative aspect would considerably constrain our model. If it turns out to be true, this finding will support an intriguing possibility that contractile units similar in structure and composition to those that form quasi-2D networks under the cell membrane to mediate cytokinesis or cell migration may alternatively organize into 3D F-actin networks to drive intracellular transport.

Despite being developed in the context of the cytoskeleton, our model and approach may be readily generalized and provide generic insight for a broad class of systems over a wide span of length scales. Our findings have suggested a robust mechanism for collective directed motion. The proposed mechanism based on broken continuous symmetry and dynamic instability of the quiescent state may not only explain cortical flow on sub-cellular scale, but may also be relevant for collective cell migration in epithelial layers on multicellular tissue level. Three crucial aspects in cell migration during wound healing could be encoded in such as model: (1) how cells sense the stress gradient (captured by a high motor susceptibility); (2) mechanical communication between neighboring cells (via nonlinear elastic bonds mimicking adhesive molecules and hard/soft-core repulsion accounting for excluded volume effect); (3) directed motion (based on mechanochemical coupling in a connected structure). We have shown by stochastic simulations that excluded volume interaction quantitatively modifies the flow speed, but does not affect the flow transition. The mechanism for active contractility that we have demonstrated for a model actomyosin network is likely to work also for blood clots, where platelets play a similar role to myosin motors and apply internal stresses. Similar principles apply yet on larger scales.

In summary, through a combination of reconstituted model systems, theoretical modeling, and precision measurement techniques applied more and more also to living cells, we have learned much about fascinating active states of matter, such as those exhibited by the cytoskeleton. Although the controlled design of biomechanical functions and biomimetic materials on a micro-assembly line may remain a distant goal for the foreseeable future, the concrete steps towards its realization in the laboratory and their theoretical modeling are being addressed

now. In vitro tests and in silico simulations will enable quantitative studies of functional modules of reduced and well-defined complexity. Yet our understanding of the physical principles underlying the complex and delocalized biological functions will always rely on identifying the governing physical mechanisms, with the aid of coarse-grained analytical models. A closer synergy of theoretical and experimental physics, detailed numerical modeling, cell biology and biochemistry suggests itself as a natural avenue for future progress.

Bibliography

[1] Gammaitoni, L., Hänggi, P., Jung, P. & Marchesoni, F. Stochastic resonance. *Rev. Mod. Phys.* **70,** 223–287 (1998).

[2] Howard, J. *Mechanics of Motor Proteins and the Cytoskeleton*, (Sinauer Assoc., Sunderland, MA, 2001).

[3] Baskarana, A. & Marchetti, M. C. Statistical mechanics and hydrodynamics of bacterial suspensions. *Proc. Natl. Acad. Sci. USA* **106,** 15567–15572 (2009).

[4] Onsager, L. The effects of shape on the interaction of colloidal particles. *Ann. New York Acad. Sci.* **51,** 627–659 (1949).

[5] Hatwalne, Y., Ramaswamy, S., Rao, M. & Simha, R. A. Rheology of active-particle suspensions. *Phys. Rev. Lett.* **92,** 118101 (2004).

[6] Alon, R., Hammer, D. A. & Springer, T. A. Lifetime of the P-selectin-carbohydrate bond and its response to tensile force in hydrodynamic flow. *Nature* **374,** 539–542 (1995).

[7] Dudko, O. K., Hummer, G. & Szabo, A. Intrinsic rates and activation free energies from single-molecule pulling experiments. *Phys. Rev. Lett.* **96,** 108101 (2006).

[8] Lenz, P., Joanny, J.-F., Jülicher, F. & Prost, J. Membranes with rotating motors. *Phys. Rev. Lett.* **91,** 108104 (2003).

[9] Mori, M., Monnier, N., Daigle, N., Bathe, M., Ellenberg, J. & Lénárt, P. Intracellular transport by an anchored homogeneously contracting F-Actin meshwork. *Curr. Biol.* **21,** 606–611 (2011).